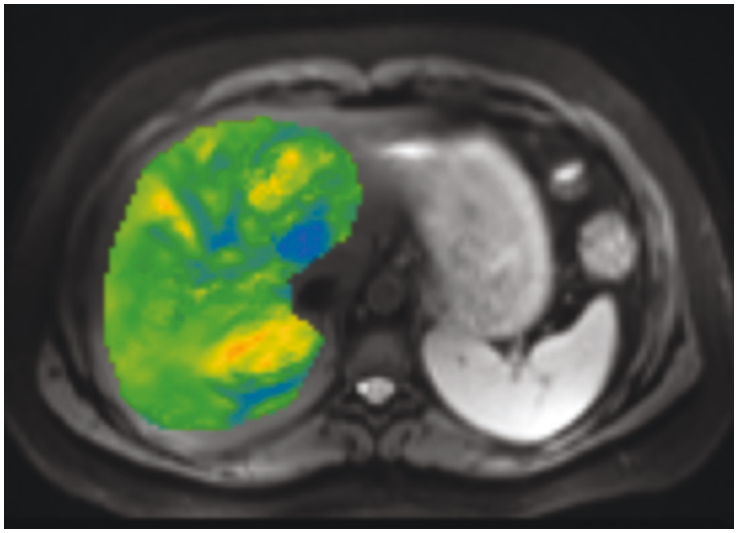

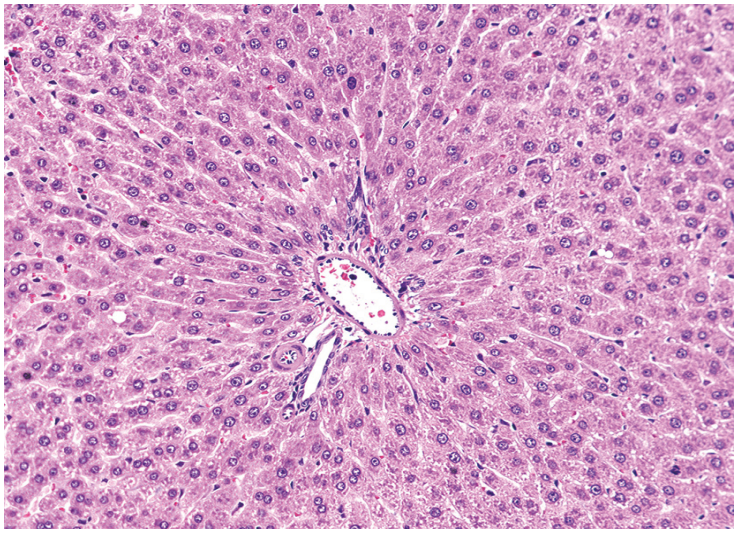

Aus dem Institut für Tierpathologie des Fachbereichs Veterinärmedizin
der Freien Universität Berlin

In Kooperation mit der
Klinik für Radiologie
Charité- Universitätsmedizin Berlin

Studies of microstructural changes of liver tissue by magnetic resonance elastography and diffusion-sensitive magnetic resonance imaging.

Inaugural-Dissertation
zur Erlangung des Grades einer
Doktorin der Veterinärmedizin
an der
Freien Universität Berlin
vorgelegt von

Karolina Maria Krehl
(geboren Garczyńska)
Tierärztin
aus Szczecin (Stettin) in Polen

Berlin 2022
Journal-Nr.: 4371

Aus dem Institut für Tierpathologie des Fachbereichs Veterinärmedizin

der Freien Universität Berlin

In Kooperation mit der

Klinik für Radiologie

Charité- Universitätsmedizin Berlin

Studies of microstructural changes of liver tissue by magnetic resonance elastography and diffusion-sensitive magnetic resonance imaging.

Inaugural-Dissertation

zur Erlangung des Grades einer

Doktorin der Veterinärmedizin

an der

Freien Universität Berlin

vorgelegt von

Karolina Maria Krehl

(geboren Garczyńska)

Tierärztin

aus Szczecin (Stettin) in Polen

Berlin 2022

Journal-Nr.: 4371

Gedruckt mit Genehmigung

des Fachbereichs Veterinärmedizin

der Freien Universität Berlin

Dekan:	**Univ.-Prof. Dr. Uwe Rösler**
Erster Gutachter:	**Univ.-Prof. Dr. Robert Klopfleisch**
Zweiter Gutachter:	**Univ.-Prof. Dr. Ingolf Sack**
Dritter Gutachter:	**Univ.-Prof. Dr. Jörg Aschenbach**

Deskriptoren (nach CAB-Thesaurus):

liver; imaging; magnetic resonance imaging; hepatomegaly; liver cells; tissues; viscosity; diffusion; perfusion; degradation

Tag der Promotion: 01.12.2022

Nothing in life is to be feared, it is only to be understood. Now is the time to understand more, so that we may fear less.

Maria Skłodowska-Curie

Table of contents

List of abbreviations

ADC	apparent diffusion coefficient
ALB	serum Albumin
ALP	Alkaline Phosphatase
ALT	Alanine-Aminotransferase
APRI	AST to platelet ratio index
AST	Aspartate-Aminotransferase
AUDIT-C	Alcohol Use Disorders Identification Test
B_0	external magnetic field
BC	before the Christian era
BD	bile duct
BMI	Body Mass Index
BW	body weight
CA	contrast agent
CL	caudate lobe
CLZ	centrilobular-zone
CT	computed tomography
CV	central/ centrilobular vein
DCL	dorsal caudate lobe
DLD	diffuse liver disease
DRL	dorsal right lobe
DS	space of Disse
DWI	Diffusion weighted imaging
FLL	focal liver lesions
GGT	γ-glutamyltransferase
H&E	Hematoxylin & Eosin- common histological stain
HA	hepatic artery
HCC	hepatocellular carcinoma
INR	international normalized ratio
LC	lymphatic capillaries
LFTs	Liver Function Tests
LLL	left lateral lobe
LML	left middle lobe
MEG	motion encoding gradient
ML	middle lobe
mpMRI	multiparametric MRI

MRE	magnetic resonance elastography
MRI	magnetic resonance imaging
MZ	mid-zone
NAFLD	nonalcoholic fatty liver disease
NASH	nonalcoholic steatohepatitis
pm	post mortem
PP	periportal-zone
PT	portal tracts
PV	portal vein
RF	radiofrequency
RL	right lobe
RML	right middle lobe
ROI	region of interests
SNR	signal-to noise-ratio
SW	shear waves
SWS	shear waves speed
T	Tesla
T1w	T1-weighted
T2w	T2-weighted
TE	echo time
TR	repetition time
US	ultrasound sonography
VCL	ventral caudate lobe
VRL	ventral right lobe

List of Figures

List of tables

1 Introduction

The liver is the largest gland and one of the most important organs of the body. It is a vital organ with over 500 functions: it detoxifies and filters the blood, metabolizes and stores carbohydrates, is involved in fat digestion, produces proteins, regulates blood clotting, and stores vitamins and minerals. With its functionality, anatomy, and unique blood supply, the liver quickly adapts to changes in the organism. Such physiological adaptations, as well as pathological processes lead to changes in the liver's microstructure. The regenerative capacity of the liver is unique, but it can disguise many pathologies, making early diagnosis challenging. Hence, there is a need for new diagnostic modalities that elucidate the link between the liver's microstructure and biophysical tissue alterations during both, normal physiological adaption and abnormal changes in disease.

One of the oldest examination techniques to assess an organ's size, shape, firmness, and structure is palpation. Manual palpation, however, is limited to superficial organs, cannot be quantified, and depends on the examiner's experience. Elastography is an imaging method that allows us to palpate even deep-lying organs as well as the small lesions. Magnetic resonance elastography (MRE) is an elastography technique based on magnetic resonance imaging (MRI), in which an external source generates vibrations that elicit shear waves in biological tissue, which can be quantified to derive information on the tissue's biomechanical properties. MRE is often coupled with other MRI modalities, such as diffusion-weighted imaging (DWI) – a technique that investigates the movement of water molecules to achieve a comprehensive biophysical characterization of the tissue. While the combined use of MRE and DWI has shown promising results in the clinical diagnosis of hepatic pathologies in earlier studies the relationship between tissue microstructure and biophysical alterations quantified by MRE and DWI is still not clear.

Therefore, the aim of this work was to elucidate the connection between biophysical features in imaging and tissue microstructure using *ex vivo* rat liver. First, the time dependence of autolytic changes that occur in *ex vivo* tissues after death and the reliance of such changes on blood content were investigated. Second, the influence of normal pregnancy on the microstructure and biophysical properties of the liver was investigated. Viscoelastic parameters and water diffusivity were compared with histological findings in the liver to demonstrate the potential of MRE and DWI imaging techniques for assessing microstructural liver changes during physiological processes and thus lay the basis for understanding changes that occur in disease.

2 Literature

2.1 Liver

Because of the majority of its functions, the liver is often referred to as "the central laboratory of the organism" [1-3]. As a versatile organ, the liver produces bile necessary for fat digestion and regulation of blood clotting, detoxifies the blood, and plays the leading role in carbohydrates metabolism and the storage of glycogen, vitamins, and minerals [2-5].

2.1.1 Gross anatomy, rat and human comparison

The weight of the liver is approximately 2-3.5% of the body weight (bw), about 1.5 kg in humans and 12 g in rats (350 g bw) [6, 7]. The organ is located in the upper abdomen, whereas in rats the liver extends over the entire subdiaphragmatic region and is lobed (each lobe is individual), in humans the liver is non-lobulated, and is confined to the upper right abdominal quadrant and entirely covered by the ribcage [6]. In both species, the four lobes are distinguishable in humans (traditional, topographical significance only), shown in Figure 1A: right and left lobes, delimited by the falciform ligament, caudate and quadrate [8]; in rats, shown in Figure 1B: left lateral lobe (LLL), median lobe (ML) - divided by the umbilical fissure into a small left median part (LML) and a large right median part (RML), right lobe (RL) - divided into two overlapping parts: dorsal (DRL) and ventral (VRL), and the caudate (CL) is also divided into a dorsal (DCL) and ventral (VCL) part [9, 10]. More precisely, the human liver is subdivided based on vascular anatomy according to the Couinaud system, in which eight segments are distinguished [8, 11], shown in Figure 1A. The abdominal bands, which are distinctive to humans, are not evident in rats. Rats do not have a gallbladder, whereas in humans, it is located below the right lobe [6]. The absence of a gallbladder in rats is probably the result of a random mutation [12] and bile is transported directly to the duodenum via the common bile duct.

The liver has a unique dual afferent blood supply and receives ca. 25 % of the cardiac output. The hepatic artery brings oxygen-rich blood from the heart (about 25 % of the total blood supply to the liver) and the portal vein (75 %) brings nutrient- and hormone-rich blood from the spleen, gastrointestinal tract, and pancreas [3, 13, 14]. Both systems unite in the sinus bed, where blood flows into the central vein and from there via the hepatic veins into the inferior vena cava and back to the heart [1, 13, 14]. For a summary of the comparison of rat and human liver, see Table 1.

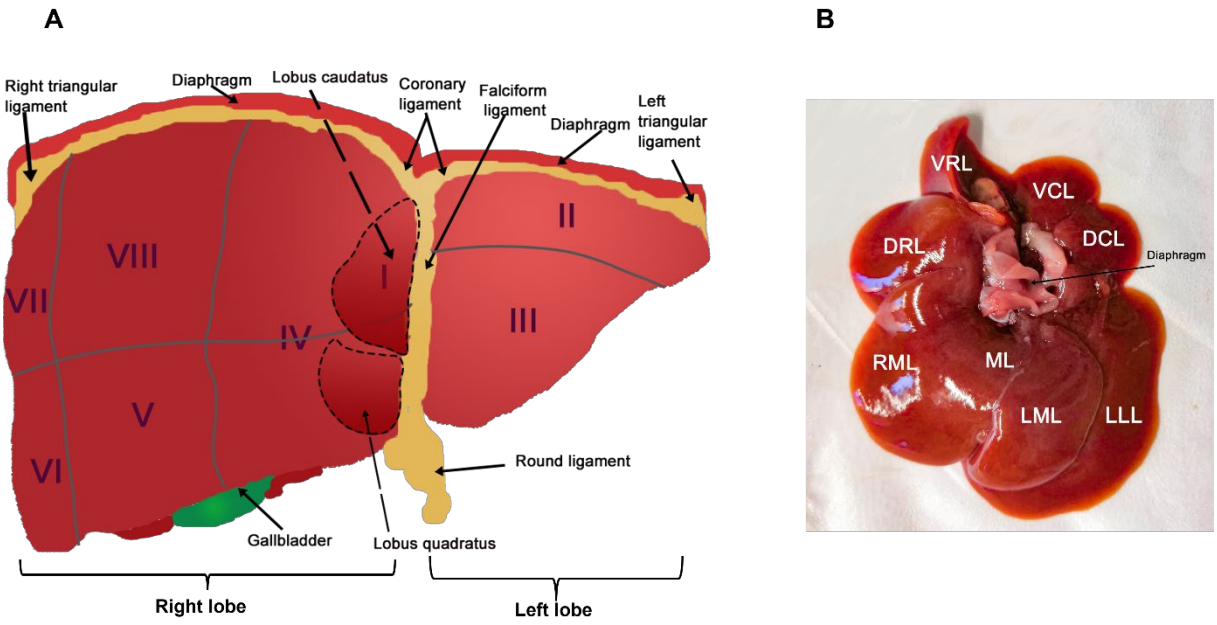

*Figure 1 Gross anatomy of human (**A**) and (**B**) rat liver*

*(**A**) Human liver with the main ligaments and marked Couinaud segments; I- caudate lobe, II-III left lobe, IV-VIII right lobe. (**B**) Rat liver: left lateral lobe (LLL), middle lobe (ML)- divided in small left middle (LML) and a large right middle part (RML), right lobe (RL)- divided in dorsal (DRL) and ventral (VRL), caudate lobe (CL) also split into dorsal (DCL) and ventral (VCL).*

2.1.2 Microstructure of the liver

The liver is a cell-rich organ consisting of parenchymatous cells (hepatocytes) - which form the main mass and structure of the liver - and non-parenchymatous cells - Kupffer cells, sinusoidal endothelial cells, stellate cells and other [15].

There are several concepts for describing the functional unit of the liver [8]. The classical concept is the hexagonal lobule with the terminal hepatic vein (central or centrilobular vein, CV) in the center, divided into a centrilobular- (CLZ), mid- (MZ) and periportal (PP) zone with portal tracts (PT, portal vein (PV), hepatic artery (HA), bile duct (BD) and lymphatic capillaries (LC)) at the edges, described by Kiernan in 1833 [16, 17]. The second most common concept was introduced by Rappaport in 1954 [18] and described the acinus with the portal tracts at the center and zones 1, 2 and 3 with terminal hepatic venules at the periphery. Zones 1, 2 and 3 correspond to PP, MZ and CL respectively [17].

Hepatocytes are polygonal epithelial cells with one or more large nuclei containing nucleoli; about 50% of hepatocytes are polyploid. Two abutting hepatocytes delimit a space known as the bile canaliculus- the first part of the biliary system [4]. Hepatocytes are grouped in columns-interconnected plates/ cords- and appear to be radiating between CV and PT [6, 7]. The plates of hepatocytes anastomose freely, and the spaces between them are irregular sinusoids - the capillaries of the liver, whose walls consist of a discontinuous layer of

fenestrated endothelial cells [4, 6]. Nutrient- and oxygen-rich blood flows from the hepatic artery and portal vein branches in the portal triads through the hepatic sinusoids into the central vein. Kupffer cells located in the sinusoids cleanse the blood of aged erythrocytes and remove bacteria and debris. In a narrow perisinusoidal space (the Disse space, DS) between endothelial cells and hepatocytes, there is a free exchange of macromolecules between blood and hepatocytes. The space of Disse contains plasma and type 3 collagen, which forms a reticulin scaffold and hepatic stellate cells (Ito cells). Ito cells store lipid droplets containing vitamin A and regulate the local immunity [4, 6, 15, 17]. Depending on the blood flow, a different distribution of macromolecules, nutrients and decreasing oxygen gradient is observed across the three zones- centrilobular-/ third-zone is most susceptible to damage due to ischemia or toxic substances [7, 19]. Bile flows in the opposite direction than blood, from the canaliculi, which form a complex pattern of branches and anastomosing channels, through the bile ducts to the Hering's canal, and terminates in the bile duct junction in the portal triad [4, 15, 20].

The microarchitecture of the liver is similar in all animal species, yet there are differences between small and large mammals [12]. The portocentral distance [12] which is comparable in humans and rats- 385 [21] or 300-355 µm, respectively [22, 23]- measures 620 µm in the pig liver [24]. There are differences in vessels between rats and other mammals, including humans [20]. In contrast to humans and other mammals, sinusoids in rats not only drain into the central vein but also into the hepatic venous system at all levels of the hepatic venous tree [20, 25]. Blood enters the sinusoids not only from the terminal portal vein but also directly from larger venous branches, and unlike in humans and pigs, there are no septal venous branches in rats [20, 23]. Because of these vascular attributes, the Rappaport acinar liver concept cannot be applied to rat liver [23]. Another variation between species is the amount of connective tissue in the portal vein ducts and between lobules, which is known to determine tissue stiffness and "fracture toughness" [12, 26, 27]. The least amount of connective tissue in the portal canals is found in rodents, followed by healthy human livers, well developed in ruminant and equine livers, and pronounced in porcine livers with connective tissue septa between PT [6, 7, 12, 20, 28, 29].

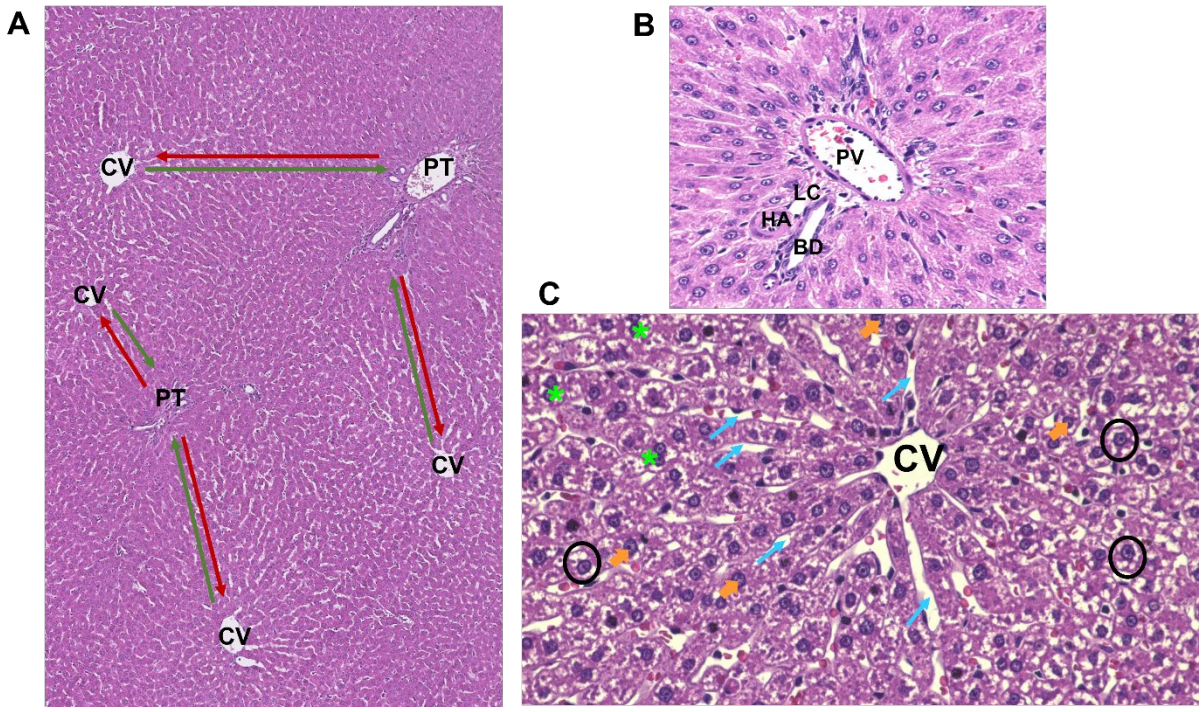

Figure 2 Microanatomy of the rat liver

*H&E overview staining of rat liver: **A** central vein (CV) and portal tracts (PT) with flow direction of blood (red arrow) and bile (green arrow) marked, 10x; **B** portal tract with portal vein (PV), hepatic artery (HA), bile duct (BD) and lymphatic capillary (LC), note the small amount of connective tissue, magnification 20x; **C** hepatocytes cords radiating to central vein (CV), green asterisk: binucleated hepatocytes; black circle: "hepatocyte clearing" because of postprandial glycogen storage, thick orange arrow: nuclei of hepatocytes, thin blue arrow: liver sinusoids, magnification 20x.*

Table 1 Comparison of rat and human liver, adapted from [6, 30]

Feature	Rat	Human
Gross		
Weight	2-3.5% of bw ~ 12 g	2-2,5% of bw ~ 1.5 kg
Location	cranial abdomen, fills entire subdiaphragmatic area	upper right abdominal quadrant
Lobation	yes	no
Liver lobes & corresponding segments according to Couinaud [11]	Caudate lobe Left lobe Middle lobe LML RML Right lobe	Segment I Segment II Segment III Segments IV, V and VIII Segments VI and VII
Ligaments	not apparent	prominent
Gallbladder	not present	underneath right lobe
Macroscopic		
Portocentral distance	300-355 µm	385 µm
Portal triads	Only bigger apparent	All sizes are apparent
Connective tissue (collagen) in and between PT	very spare, may be seen in H&E	spare but more prominent than in rat, distinct in H&E in portal regions
Sinusoids drain	CV + all levels of hepatic venous tree	only to central vein
Nutrients-rich blood inlet	PV + larger venous branches	only terminal PV in PT
Septal vein branches	not apparent	present

2.2 Clinical assessment of the liver

Liver disease accounted for 2.5% of disability-adjusted life years worldwide in 2019, of which liver cirrhosis alone accounted for 1.69%, making it the 13th leading cause of death[31]. These numbers reflect the importance of liver diseases in the clinic. The liver is susceptible to a variety of metabolic (e.g., nonalcoholic fatty liver disease-NAFLD), toxic (e.g., alcoholic liver disease), infectious (e.g., viral hepatitis A, B, or C, bacterial infections), immune-mediated

(e.g., primary sclerosing cholangitis, primary biliary cirrhosis), mechanical (e.g., obstructive cholestasis, vascular disorders), or environmental (e.g., heat stroke) and other injuries [8, 32]. The regenerative capacity and the enormous functional reserve of the liver lead to an asymptomatic course of liver diseases in the early phase [8, 33, 34]. Most often, liver abnormalities are diagnosed accidentally during other examinations or when symptoms appear, which is usually years after the onset of liver damage, when patients already have chronic liver disease [8, 35]. All of these factors combined make the diagnosis of liver disorders so challenging and highlight the importance of detecting disease at the earliest possible stage, so that steps can be taken to prevent the progression of liver fibrosis and the development of end-stage liver disease [8, 35]. The assessment of liver disease has two goals: i) to determine the cause of liver injury and its ii) severity. It includes patient history, biochemical tests, clinical findings, imaging, and often liver histology [8, 32, 35] and must be performed in two common situations: in symptomatic patients with clear signs of liver disease (e.g., upper abdominal pain, jaundice, acholic stools) and in asymptomatic patients with abnormal liver biochemistry [32, 35, 36].

Several factors in the patient's history are important for the correct diagnosis of possible liver disease: risk factors for hepatitis B or C virus (e.g., blood transfusions prior to 1992, tattoos or piercings by amateurs, injection drug use), alcohol history (Alcohol Use Disorders Identification Test- AUDIT-C), medication history (prescribed drugs - even after long-term use - can cause adverse drug reactions - up to 10% of patients with jaundice, who are hospitalized, non-prescribed medications, herbal medicines), family history (increased risk for autoimmune hepatitis, Willson's disease or primary biliary cirrhosis if family history is positive), symptoms (lethargy, pruritus, dry eyes and mouth, right upper quadrant abdominal pain and others) [32, 35].

Laboratory tests are commonly used as noninvasive tests to screen for liver dysfunction and, when abnormal, are often the first indication of liver disease in asymptomatic patients [37-39]. The colloquial term liver function tests (LFTs) encompasses various tests that reflect the different functions of the liver [37].

Tests for synthetic liver function (serum albumin (ALB), prothrombin time and International Normalized Ratio (INR) to measure blood clotting, as blood clotting factors II, V, VII, XI, and X are produced in the liver) and excretory function (total and direct bilirubin) [37, 38]. Tests that evaluate hepatic necroinflammatory activity (aspartate-aminotransferase (AST), alanine-aminotransferase (ALT)) or cholestasis (alkaline phosphatase (ALP), bile acids, γ-glutamyltransferase (GGT)) [36-42]. LFTs have limited sensitivity- normal or minimally abnormal results do not rule out liver disease or even cirrhosis [37, 38], biochemical changes occur during normal pregnancy, for example [43, 44]- and are more suggestive of a general category of liver disease rather than a specific diagnosis [38, 45].

Physical examination should not be neglected in patients with abnormal biochemical liver tests, as inspection by the physician may provide clinical indications of the etiology of the underlying liver injury [46]. Skin changes that yield important clues to liver disease have many manifestations, some of which are: palmar erythema, clubbing, Terry's nails, spider telangiectasias, or xanthelasma [32]. Jaundice is a typical sign of the obstruction of the bile ducts, or parenchymal liver disease, and is most likely to be seen in the eyes- scleral icterus- and in advanced stadium manifested by yellowish pigmentation of the skin [32, 35]. Findings on abdominal examination are now often supported or replaced by imaging of the liver [46] but inspection, auscultation, and palpation remain important in determining abdominal and hepatic tenderness, hepatomegaly, splenomegaly, or ascites and can increase clinical suspicion and help identify patients in whom liver biopsy may be warranted for the diagnosis of cirrhosis [32].

The next step in noninvasive diagnostics is imaging of the liver to evaluate diffuse liver diseases (DLD) such as fibrosis or fatty infiltration and focal liver lesions (FLL)- tumors, bile duct dilatation, and to detect ascites or measure the liver size [47, 48]. The most commonly used techniques are ultrasonography (US), computed tomography (CT) and magnetic resonance imaging (MRI) [48]. Each modality has strengths and weaknesses for diagnosis, and often only the combination of imaging techniques allows a clinical question to be answered [49].

Sonography as a rapid, cost-effective and widely available technique, is often the first method performed for many hepatobiliary disorders and can be used at the bedside [49]. US examinations are safe and can be performed in pregnant patients [47]. It provides real-time dynamic and Doppler imaging, so it can guide diagnostic procedures such as percutaneous biopsy or drainage of abscesses and gives dynamic information about the liver vasculature [37, 49]. Ultrasonography is better at detecting focal lesions than parenchymal disease, and it is the test of choice for detecting biliary dilatation in patients with jaundice [37, 47] and for detecting gallbladder stones [49]. The limitations of the test are its dependence on the examiner and limited reproducibility, limited image quality in obese patients, and the fact that US beams do not readily cross tissue-gas or tissue-bone boundaries, resulting in blind spots in the liver when ribs or gas-filled bowel loops overlie the organ [37, 49].

Computed tomography is more accurate than US in determining liver anatomy and obtaining images of the entire liver [37, 47]. CT can be conducted with several protocols, including nonenhanced (without intravenous contrast agent (CA)) or contrast-enhanced tomography, which are optimized for the evaluation of liver lesions [47, 49, 50]. CT is the standard method for the FLL, contrast-enhanced CT is routinely performed in oncologic examinations, and the nonenhanced CT helps to characterize calcifications or hemorrhage [47]. It may also indicate the presence of cirrhosis, fatty liver, or iron overload, although MRI has a higher sensitivity for these [37, 47]. Computed tomography uses X-rays as the basis for

imaging, which carries a stochastic risk of ionizing radiation that can cause mutations due to chromosomal alterations; however, the risk is relatively low in a person who does not undergo frequent CT scans [49]. Pregnant patients should undergo CT only in emergencies because of the risk of radiation exposure to the fetus, and dose reduction should be used in children [49]. Contrast agents should be avoided in patients with renal injury, but the risk and benefit of contrast-enhanced CT should always be considered for the individual patient [49]. CT is a widely available and robust technique that provides images with fewer motion artifacts than MRI, even in dyspneic or uncooperative patients [47, 49]. CT images are more consistent from study to study than US examinations because they are not directly dependent on the technician's skill [49].

MRI plays an increasingly important role in the evaluation of diffuse and focal liver disease [51]. It has numerous advantages, such as the ability to provide morphologic and physiologic information, the possibility to perform multiparametric MRI (mpMRI), and is becoming the modality of choice for liver imaging due to its better contrast resolution compared to CT [51, 52].

Despite the continuous improvement of biochemical and serologic tests and noninvasive techniques such as imaging and laboratory values, liver biopsy and histologic evaluation remain the gold standard and definitive test in several liver diseases [37, 53, 54]. Since the introduction of rapid percutaneous liver biopsy by Menghini [55] in 1958, the technique has undergone many improvements and changes and fulfills three main roles: i) diagnosis of liver disease that noninvasive methods cannot diagnose; ii) assessment of prognosis and stage of liver fibrosis; and iii) assistance in treatment decisions [39, 54]. Various techniques can be used to obtain liver tissue [54]. Samples are obtained with a needle (by cutting or aspiration) that penetrates percutaneously into the intercostal or subcostal area, nowadays usually under US guidance [56]. Transvenous liver biopsy- usually via jugular vein towards the hepatic veins- is a reasonable option for patients with coagulopathies [56, 57]. A laparoscopic biopsy is also possible, allowing visual inspection of the liver surface and direct palpation, it yields more information and has better sensitivity and lower sampling error than the percutaneous method, and in the event of bleeding after sampling, the surgeon can coagulate the puncture, that makes it feasible in patients with an elevated risk of hemorrhage [54, 56, 57]. Liver biopsy is an invasive diagnostic procedure, and the indications and benefits must be weighed against the small but non-negligible risk of complications [57]. Pain after biopsy occurs in more than two-thirds of patients, serious complications occur in less than 3%, and mortality is reported in less than 0.3% of biopsies [37, 39]. Bleeding is the main problem, but severe hemorrhage occurs only 1 in 2500-10000 cases and usually within 2-4 hours after the procedure [39]. Despite the risks, the main limitations of liver biopsy are sampling errors- the material obtained is not suitable for the evaluation of a heterogeneously distributed lesion,

or the focal lesion was not caught in the tissue sample, or there is too little material for evaluation [39, 56].

Due to the changes in the epidemiology of chronic liver disease that have occurred in recent decades, with the increasing prevalence of NAFLD and the advent of curative treatments for hepatitis C [58-60], there is a growing need of accurate noninvasive tests for the diagnosis, severity assessment (e.g., staging of liver fibrosis), and follow-up of diffuse and focal liver disease [58, 61]. Emerging qualitative and quantitative imaging techniques (e.g., elastography, new Doppler US modes, new CA for MRI or CT) along with modern biomarkers (e.g. FibroTest®, AST to platelet ratio index- APRI), are the most promising approaches of liver diagnostics [58, 61]. They have recently been or are expected to be adopted in clinical practice in the next few years [58, 61].

2.3 MRI- based liver assessment

Magnetic resonance imaging offers many advantages over CT and US, including images in numerous planes and excellent resolution between different proportions of fat and water in tissues, unlike CT, it does not require ionizing radiation and is less operator-dependent than US [37, 50]. MRI is the gold standard for characterizing liver lesions because it definitively classifies a lesion as benign and differentiates it from a malignant lesion [50]. MRI is an excellent method for assessing blood flow and detecting hepatic iron overload [37]. It can also be combined with an intravenous contrast agent containing for example, gadolinium, and similar to CT, extracellular CA is used. Compared with CT, MRI is more sensitive to contrast and can depict vascular alterations that are difficult to see in contrast-enhanced CT [47]. Unlike CT, hepatocyte-specific CA is also available, providing additional information about hepatocyte and biliary system function [50]. Disadvantages of magnetic resonance imaging include higher costs, longer acquisition time and required patient cooperation, which may be challenging in patients with claustrophobia, respiratory problems, or children [47, 50]. The use of magnetic fields precludes imaging in patients with pacemakers or other electronic devices or metal implants [47, 50]. Gadolinium-containing CA are contraindicated in patients with poor renal function because of the risk of nephrogenic systemic fibrosis [50].

2.3.1 Basic MRI principles

MRI scanners use superconducting magnets with a strength between 0.5 to 7.0 Tesla (T) - in clinical settings to generate a static, stable, and spatially homogeneous magnetic field [62, 63]. To enable such enormous currents, electrical resistance must be eliminated. For this purpose, the magnetic coil is encased in liquid helium and cooled to about 4 K (-269°C) [63]. In this work, we used a 0.5 T tabletop MRI scanner capable to measure cost-effectively the viscoelastic properties of small biological soft tissue samples [64], see Section 2.3.3.5 for a

description of this setup. The majority of the clinical MRI scanners are 1.5 or 3.0 T, 7-T scanners are still rare in the clinic but common in animal studies, while 9.4-T machines are only used in preclinical studies, because of the gantry (the space in which the patient lies) is so narrow that it only allows measurements on small animals or phantoms and tissue probes [63]. Open gantry MRI scanners have been designed for patients with claustrophobia, but their use is limited due to the low magnetic field of 0.5 T [63]. The scanners with higher field strength provide better signal-to-noise-ratio (SNR) and a higher resolution, which allows the measurement time to be shortened [63]. In addition to the main magnet, the MRI scanner consists of gradient magnets, radio frequency coils that transmit and/or receive the MRI signals, and processing equipment [65].

More than 80% of the body tissue consists of water and fat, containing many hydrogen atoms. These have intrinsic properties such as mass, charge (positive protons) and spin [52, 63]. Protons spins are scattered in a variety of directions in the body, but when a strong external magnetic field (B_0) is applied, a portion of the protons is aligned parallel (low-energy state) or antiparallel (high-energy state) to the B_0 [52, 62, 63]. The individual nuclei rotate around the B_0 field axis, and the velocity of this rotation is the Larmor frequency, which is proportional to the strength of the magnetic field [52, 62]. To obtain an image, a radiofrequency (RF) signal at exactly the Larmor frequency (resonance frequency) is applied in short pulses perpendicular to B_0 [66]. Two phenomena occur with the RF signal: first, enough protons absorb energy to jump from the low parallel energy state to the high antiparallel energy state, resulting in a net longitudinal magnetization angled (flip angle) away from B_0, and second, the spins are “whipped” so that they precess in phase, resulting in a net transversal magnetization [52, 66, 67]. When the RF pulse is suspended, the protons return to their normal low-energy state and seek the equilibrium state [62, 63]. During this realignment, the nuclei lose energy and emit their own RF signal- the FID (Free Induction Decay Response) signal, which is detected by the coil placed around the subject (patient/ animal/ tissue probe) and provides information to create the MR image [52, 62]. The time required to restore equilibrium is the relaxation time and depends on the type of tissue [63, 66]. There are two different independent types of relaxation processes: longitudinal relaxation, described by the time constant T1, which is the time required for the system to recover to 63% of its equilibrium, and the transversal relaxation, described by T2- the time required for dephasing to allow the signal to decay to 37% of its original value after exposure to the 90° RF pulse [52, 66, 67]. T1 depends on the surrounding structure or lattice and is therefore also referred to as spin-lattice relaxation [52], it can be manipulated by the repetition time (TR)- the time between RF pulses [62]. T2 depends on the spin-spin interactions between protons and their nearest environment and is also called spin-spin relaxation [52, 67]. Its extent is controlled by the echo time (TE)- the time between the first RF excitation and the acquisition of the signal [67]. Both co-occur, and T2 is always shorter

than T1 [52]. By modifying the appropriate parameters (RF pulses, TR, TE, and flip angle), the resulting signal is altered to produce weighted images [52]. For T1- weighted (T1w) images, the shorter TR and shorter TE, the higher the signal, while for T2-weighted (T2w) images, a long TE and TR result in a higher signal [66]. T1w images mean that the difference in tissue contrast is mainly due to the difference in T1 and represents tissue with a higher signal of the shorter T1 value (short longitudinal relaxation time and rapid recovery) [63, 67]. T2w images are proton density-weighted images and represent tissue higher signal of the longer T2 value (long transverse relaxation and slow signal attenuation) [63, 67]. Different settings of other parameters (such as gradient echo or spin echo) allow adjusting the contrast between tissues and visualizing pathological conditions. Fluid, edema, fat and most solid hepatic masses are hyperintense in the T2w images, whereas T1w images show them darkly but can be helpful in detecting hemorrhage within liver tumors or melanoma metastases in the liver [52].

2.3.2 Diffusion Weighted Imaging

Diffusion weighted imaging (DWI) is an MRI technique based on motion encoding by magnetic field gradients [52] and is the result of the work of Stejskal and Tanner [68] in the 1960s. Although the first diffusion images of the brain were made in 1985 and Le Bihan et al. tested diffusion encoding in the liver in 1984 [69, 70], DWI was not adopted in clinical imaging because of the long acquisition time and high sensitivity to motion artifacts. It was not until the early 1990s that several technological advances, such as the availability of echo-planar imaging, high gradient amplitudes, multichannel coils, and parallel imaging, helped expand DWI applications [71, 72].

2.3.2.1 Basic principles of DWI

As the name suggests, DWI provides information about diffusion- the random microscopic motion of (water) molecules driven by their internal thermal energy [73]. The diffusion of water molecules follows the rules of Brownian motion, and we distinguish between “isotropic” and “anisotropic” motion [62]. Isotropic motion is random movement in all directions and is only possible when the water molecules are unconstrained [62]. Due to constraints, anisotropic motion is still random, but not the same in all directions [62]. In biological tissues, water moves in intracellular, extracellular and intravascular spaces and between them [73]. Diffusion in tissues is restricted by their biophysical properties: cell organization (cell membranes, fibers, macromolecules), density, microstructure, and microcirculation [73]. Different tissues have characteristic diffusion properties due to their specific cell architecture and proportions of intracellular and extracellular compartments [71]. Pathological, as well as physiological, processes that affect cell architecture, tissue composition, and distribution between extracellular and intracellular compartments alter water diffusivity [71]. Cellularity and integrity of cell membranes are inversely related to water diffusion [72]. Tumors, abscesses, and fibrosis

have high cellularity, so diffusion is restricted or impeded [73]. Cysts and necrotic tissue (e.g., tumors after treatment) have low cellularity and often disrupted membranes, and diffusion is relatively free or unimpeded [72, 73].

Diffusion weighted imaging uses spin-echo sequences with two symmetric diffusion sensitizing gradients (dephasing and rephasing, respectively) with a 180° refocusing pulse in between [72, 73]. For static molecules, the effect of the dephasing gradient is canceled by the rephasing gradient; overall, the measured signal intensity does not change significantly in tissues with restricted diffusion-the T2 signal is preserved [72, 73]. When not hindered, water molecules move between the dephasing and rephasing gradients and depending on the distance traveled, they are not fully rephased, resulting in a decrease in T2 signal intensity [72, 73]. The extent of water movement is proportional to the signal attenuation [72]. DWI detects very small motions of water molecules at the microscopic level [73]. The sensitivity of the DWI can be adjusted by changing the “b-value”, expressed in s/mm², which is proportional to the gradient amplitude (usually) but also to the duration of the gradient and the time interval between the paired gradients [72, 74]. The higher the b-value the more sensitive the sequence-small b-values (e.g., b = 50-100 s/mm²) are sensitive to large motions, while large b-values (e.g., b = 1000 s/mm²) show slow-moving molecules/short diffusion distance [72, 73]. DWI should be performed with at least two b-values, which must always be specified to allow correct interpretation of the images; in general, the higher the b-value, the greater the degree of signal attenuation [72].

DWI provides qualitative and quantitative information about the tissue. Qualitative DWI assessment is visual and based on the relative tissue signal attenuation: cysts and heterogenous tumors with necrotic areas show greater signal attenuation at high b-values because water is less restricted, while high cellular solid tumors show high signal intensity [72]. Quantitative DWI measurements are reflected in the apparent diffusion coefficient (ADC in mm²/s) [72]. ADC measures tissue water diffusivity and is the mean value of diffusion contributed by intracellular, extracellular, and vascular water molecules and their interactions between their structural and chemical environments within an image voxel at different b-values [73]. More b-values reduce the error in ADC calculation [62, 72]. Highly cellular tissue - with restricted diffusion - shows low ADC values, while tissue with relative free diffusion - low cellularity - shows high ADC values [73].

Like any technique, DWI has its limitations. The signal-to-noise ratio and spatial resolution of DW images are low, and DWI is also prone to some artifacts [73]. Breathing, cardiac, or voluntary movements can cause ghosting images and blurring, so respiratory triggering or breath-hold scans are recommended [73]. T2-shine through appears in tissues with very long T2 relaxation times, and the strong T2 signal may be mistaken for restricted diffusion [74]; to differentiate it, it corresponds to a bright signal on the ADC map [71]. A T2

blackout with a low signal on the ADC map is due to a lack of sufficient water protons rather than restricted diffusion and corresponds to a low signal on T2w fat-saturated images [71]. Nevertheless, diffusion weighted imaging has been established in the fields of stroke imaging (historically its first application), white matter diseases (e.g., multiple sclerosis, Alzheimer's disease) and oncology [71]. It provides information on molecular activity and cellular function as an adjunct to MR imaging, helping to detect and characterize tumors and predicting and evaluating therapy response [74]. DWI should always be combined with conventional MRI because of its high sensitivity to artifacts and poor resolution [71, 73].

2.3.2.2 DWI in the diagnostic of liver diseases

DWI is useful for detecting and characterizing focal liver lesions in the liver and is a desirable tool for patients who cannot receive intravenous contrast [75, 76]. It has a high sensitivity for the detection of liver metastases, especially for small lesions (less than 2 cm) [75], but shows moderate sensitivity for hepatocellular carcinomas (HCC), especially in the cirrhotic liver [75]. The evaluation of qualitative DW images to differentiate between malignant and benign lesions remains controversial. Some differences between them are observed in research with a high degree of accuracy, but there is also considerable overlap between lesions, yet the additional information provided by DWI can help characterize the lesion in some cases [71-73, 75-77]. Although differentiation between solid lesions by ADC is not reliable, separation of liver cysts and hemangiomas from malignant liver lesions is possible [75]. DWI can provide valuable early information for treatment planning, clinical decision-making, and response to treatment in oncology [71, 75]. Changes in ADC value precede lesion size or enhancement changes and correspond with tumor necrosis [75, 76]. Further prospective studies are needed for this new application of DWI, and researchers are confident that DWI has not yet reached its full potential [71, 75]. Another promising application for DWI is assessing diffuse liver disease, such as quantifying the degree of fibrosis [77-79]. Good diagnostic accuracy has already been demonstrated with intravoxel incoherent motion DWI at high field strength (3.0 T) [75, 78].
DWI has the potential as an imaging biomarker for fibrosis, tumor detection/characterization, and tracking/predicting therapy outcomes [80]. Research efforts should focus on improving accuracy and reproducibility and standardizing imaging parameters [80].

2.3.3 Magnetic Resonance Elastography

2.3.3.1 Background

Since the beginning of medicine, palpation has played a significant role in examining and diagnosing diseases [81]. The value of assessing the hardness and consistency of accessible body parts was described in the Edwin Smith Papyrus (3000-2500 BC), and in the texts from China (475-221 BC) were mentioned as an important diagnostic method [82]. Even today,

medical students learn that a palpable hard mass in the thyroid, breast, or prostate gland indicates malignancy, and surgeons discover liver tumors at the time of laparotomy that were not seen in preoperative imaging by CT, MRI, or US [83]. Diagnosis by palpation is very limited, only superficial organs can be reached and usually, only major changes can be detected, it is a subjective examination method that relies on the experience and sensitivity of physicians and does not provide quantitative data that can be used for follow-up examinations or compared by different examiners [84].

The value of a quantitative assessment of the mechanical properties of tissues was recognized and led to the development of elastography.

2.3.3.2 What is elastography?

Elastography is a field of medical imaging that maps and measures soft tissues' mechanical properties [85, 86]. Before going into details of elastography, some commonly used terms need to be identified and explained (see Table 2).

Table 2 Glossary of terms used in elastography.

Term	Definition
a in m/s	Describes the inverse attenuation per frequency- the penetration rate of the waves in the tissue *a* = penetration length x frequency. Penetration is related to the attenuation properties of the tissue: geometric and intrinsic damping. [87] In this work, *a* is inversely correlated with tissue viscosity.
Attenuation	The amplitude loss of waves through viscous tissue [88]
c in m/s	Represents the speed at which a shear wave (SW) propagates through the medium, also known as shear wave speed (SWS). *c* depends on the frequency at which the SW is applied *c* = wavelength x frequency. [87] In this work, *c* represents the stiffness of the tissue.
Elasticity	Describes the ability of a material to return to its original size and shape after the deforming forces have been removed. [88-90]
Elastography	It is a field of noninvasive medical imaging modalities (based on ultrasound- or MRI) that image and measures the mechanical properties of soft tissues. [86, 88]
Inversion algorithm	A mathematic algorithm that allows the calculation of mechanical properties from wave images. [88]
Shear wave (SW)	It is a type of mechanical wave that oscillates perpendicular to its propagation direction. It is also known as S-wave or transversal wave [88, 89].
Stiffness	Traditionally, it was evaluated by palpation and described with qualitative statements. It expresses the resistance to deformation of an object in response to applied force (tension or compression). It is mathematically defined and expressed by different moduli referring to the different types of forces: elastic (tensile forces), shear (shear forces), and bulk modulus (volumetric compressive forces). In elastography, the term stiffness should explicitly indicate the quantity to which it refers. [88-90]
Viscoelasticity	A property of materials that exhibit both viscous and elastic behavior when deformed. All biological soft tissues are viscoelastic. [88, 91]
Viscosity	It measures the resistance of a material to deformation and is related to the absorption of the mechanical energy. [88-90]

Elastography measures the response of tissue to deformation. It can be distinguished by the source (static, quasi-static, or dynamic), duration (transient or continuous) of tissue deformation, and modality used for tracking (ultrasound or MRI) [88]. In static/quasi-static

elastography, also called strain elastography, pressure is applied to the tissue and no vibrations or waves in the tissue are monitored or imaged [82, 91]. Since it was not used in this work, it will not be discussed further. Dynamic- shear wave elastography has become the dominant method [82]. Here, the mechanical properties of tissues are assessed by evaluating the propagation of mechanical waves, which travel through the body as compression and shear waves [88]. In compressions waves (longitudinal waves), the tissue moves back and forth parallel to the direction of wave propagation, while shear waves (SW) produce tissue motion to the wave propagation. The compression waves move almost 1000 times faster than shear waves in soft tissue. Because of the speed and tissue specificity, all current elastography techniques track shear waves (SW) [81, 88]. SW can be generated by external mechanical vibrations applied to the body surface over the tissue of interest or by focusing acoustic radiation force impulses inside the tissue of interest [86]. In this thesis, MRI Elastography (MRE) based on time-harmonic continuous vibrations was applied [88]. Henceforth, this technique will be discussed in more detail.

2.3.3.3 Principles of MR Elastography

A basic MRE examination consists of three steps: i) vibration excitation- generated time harmonic mechanical shear waves deform the tissue; ii) visualization of the propagating waves- image acquisition and displacement encoding using a phase contrast sequence; iii) reconstruction of viscoelastic parameters- processing of the wave images using inverse algorithms, quantitative images are generated [90-92], see Figure 3.

A complete description of the basics of MR Elastography is beyond the scope of this work, for further reading, please refer to the book "Magnetic resonance elastography: physical background and medical applications" [93], which integrates important concepts of MR physics, viscoelastic theory and signal processing and provides access to important background content.

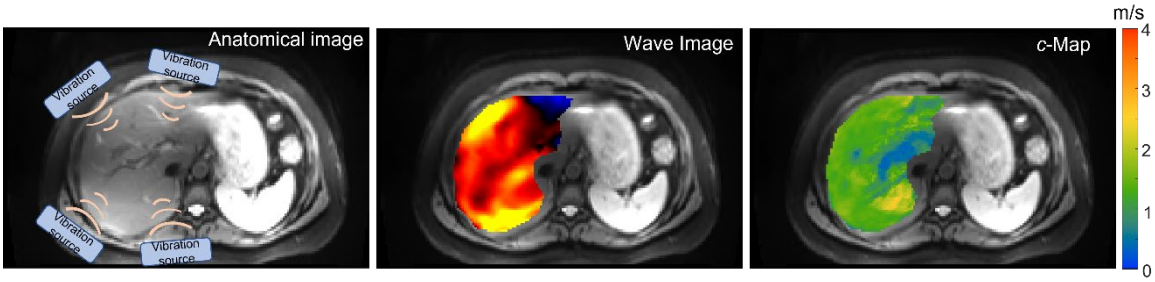

Figure 3 The three basic steps of elastography, on an example of human liver MRE.

i) Vibration excitation: the standard anatomical image shows the position of the vibration source, i.e., the pressure pads, which transmit the vibrations into the body via compressed air and induces shear waves, shown schematically as orange lines. ii) Visualization of the

propagating waves: a snapshot of propagating waves obtained by image acquisition and displacement encoding. iii) Reconstruction of the viscoelastic parameters: shown here on the example of c, inverse algorithms derive the stiffness from the wave properties.

There are different sources of vibration used in elastography, and the choice must be adapted to the organ under the study, and it differs between preclinical and clinical applications [81]. Devices generating SW can be based on pneumatic, electromechanical, piezoelectric and compressed air pulse systems and usually contain an active driver outside the MRI room that generates the vibrations at specific frequencies (typically 20-80 Hz for clinical MRE, and much higher for preclinical (200-1500 Hz) or phantom examinations (up to 3000 Hz) [94]), as well a passive driver that is placed on the body surface over the organ under investigation [81, 90, 92], see Figure 4.

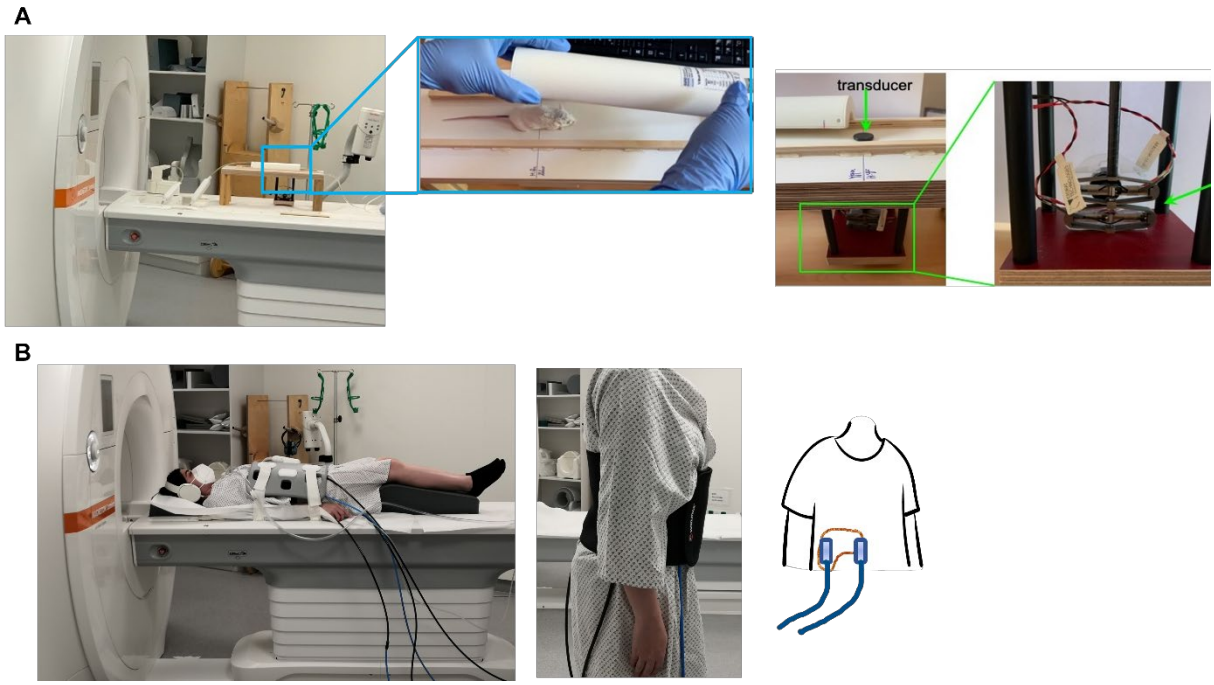

Figure 4 Examples of in vivo preclinical and clinical liver MRE setup.

***A)** Small animal coil coupled to the clinical 3T Siemens scanner for mouse liver in vivo MRE. Position of the mouse on the transducer- green arrow-transmitting vibrations from the two parallel piezo actuators shown in the enlarged photo. **B)** Setup of the 3 T Siemens clinical scanner for human liver MRE based on pressure pads- transmitting the vibrations to the body via compressed air. Pressure pads are positioned on the back and abdomen over the liver (schematically shown on the right side) and secured with a belt.*

There are many variants of pulse sequences that can be used for MRE, but generally, the phase-contrast pulse sequence is synchronized with motion encoding gradients (MEGs) to the frequency of the waves generated by the vibration actuator [85, 86, 90]. This sequence maps

the cyclic motion of the spins caused by the propagating SW. These micron-level movements result in a measurable phase shift in the acquired MR signal, which is used to quantify the displacement of the protons, resulting in a magnitude (anatomical information) and phase (wave motion information) image [83, 85, 86].

After generating magnitude and phase images, inversion algorithms can be used to recover material properties from the acquired MRE data based on various assumptions and approaches [90]. Additional images and maps are automatically generated using pre-installed codes on the MRI scanner or later by analyzing software using specific codes in the research [86]. The stiffness maps depict the stiffness of the tissue on the studied cross section; for further analysis regions of interest (ROIs) can be manually drawn to obtain the shear stiffness of the organs; calculation of other parameters is also possible [92].

2.3.3.4 Output of MRE

MRE is constantly evolving and changing, and because of the variety of techniques, different stiffness-related parameters can be reported. This variety hampers comparisons between methods [88, 90].

Shear wave speed (SWS, c in *m/s*) is often reported as it is directly related to stiffness: waves travel faster in hard (stiff) tissue, while they are slower in soft materials [82, 86, 88]. SWS can be converted to the elastic (Young's) modulus (stiffness in kPa) using this equation: $E = 3\rho c^2$, where E is Young's modulus, ρ is the tissue density (in biological soft tissue is assumed to be equal to water: 1.0 g/cm³ or 1000 kg/m³) and c is the shear wave speed [82, 88]. This equation can be used for isotropic homogenous materials. Heterogeneous and/or anisotropic materials like skeletal muscle and renal medulla should be analyzed with c [82].

Another important parameter, which is becoming increasingly important in addition to stiffness, is viscosity. Soft biological tissues are hydrated, their fluid-like behavior can be described by viscosity, while their solid-like behavior is represented by elasticity [95]. Viscosity provides information about the microstructure of soft tissues, simply put, higher cross-linking leads to higher absorption of the shear waves in the tissue, and viscous materials respond to mechanical stimulation with a time-delay- imagine the movement of water and honey [91]. The viscosity of tissue is inversely proportional to the penetration rate of shear waves into that tissue, described by a in *m/s*, the higher the penetration rate, the less viscous the tissue, for highly viscous tissue the penetration rate is low [87].

Several mathematical modules can be used to define stiffness or viscosity, and the modules define the deformation of the material and are mathematically related [88], but the description of these will go out of the scope of this work because we used for the analysis only c and a.

2.3.3.5 Tabletop MRE

To facilitate the investigations of tissue probes by MRE and to determine the relationship between tissue structure and macroscopic viscoelastic parameters for the analysis of tissue structure by *in vivo* imaging, a tabletop portable MRE device has been introduced. It operates at 0.5 T with a permanent magnet and measures the viscoelastic properties of small biological soft tissue probes at low costs [64]. With this setup, small samples (e.g., biopsy specimens) can be studied even by inexperienced personnel [64], and the low costs and availability allow longitudinal measurement.

A glass tube containing a tissue sample is placed in a sample holder coupled to a piezo-actuator (PAHL60/20 Piezosystem Jena, Jena, Germany) connected to an external gradient amplifier (DC 600, Pure Devices GmbH, Würzburg, Germany) and inserted into the MRI device (Pure Devices GmbH, Würzburg, Germany) with a 0.5 T permanent magnet [96], as shown in Figure 5A.

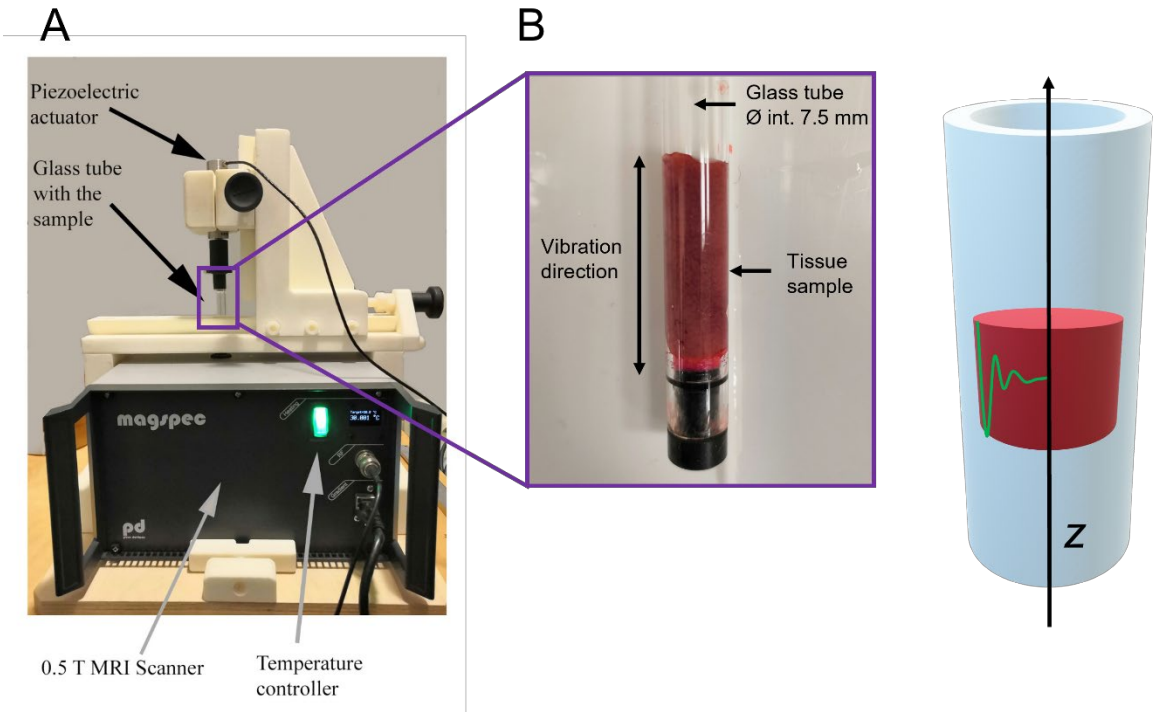

Figure 5 Tabletop MRE

Customized setup for tissue probe or gel phantom examination using MRE. ***A)*** *Portable 0.5 T MRI scanner with a piezoelectric actuator installed on top coupled to a gradient amplifier (not shown), which transmits the vibrations to the sample glass tube;* ***B)*** *Glass tube with a liver tissue sample with marked vertical direction (z-Axis) of the vibrations. On the right simplified model of the glass tube, the green curve indicates a damped shear wave propagating perpendicular from the outer edge of the sample into its center- adapted from Braun, Tzschätzsch et al. 2018 [96]*

As shown in Figure 5B, the vibrations of the piezo-electric actuator are transmitted in the vertical direction of the glass tube with the sample. The friction between the glass tube and the sample causes shear waves, the outermost sample layer moves with the tube and the second sample layer is set in motion. The generated waves propagate cylindrically from the outside to the center of the sample.

Before an experiment with a new type of tissue, a frequency sweep is performed to determine the best frequency for that specific tissue, in this case, liver tissue. In the range between 300-2000 Hz, a frequency of 800 Hz was chosen for the liver tissue in this work according to the phase, wavefield images, and frequency profile as shown in Figure 6.

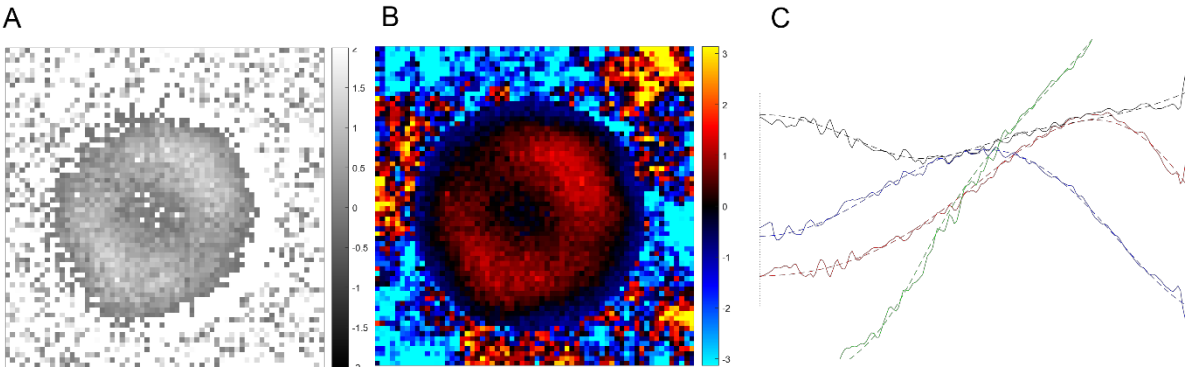

Figure 6 Wave propagation in the liver at 800 Hz

According to the phase (A) and wave field images (B), we can observe a proper concentric wave profile with more than one wave propagation at 800 Hz. This choice can be confirmed by a smooth frequency profile acquired at 800 Hz.

2.3.3.6 MRE in the diagnostics of liver diseases

MRE is becoming increasingly more important clinically [97]. It is the most promising noninvasive technique for detecting, staging, and treatment monitoring of liver fibrosis [92, 97-99]. The presence of fat alone does not affect stiffness; therefore, evaluation of fibrosis in the liver with nonalcoholic fatty liver disease (NAFLD) can be performed using elastography [92, 100]. MRE can distinguish steatosis from nonalcoholic steatohepatitis with fibrosis (NASH) with a sensitivity of 94% [101] and detect advanced fibrosis in NAFLD patients with a sensitivity of 85% and specificity of 93% [100, 102]. Tomoelastography also shows promising results in pediatric patients with NAFLD [103]. Focal liver lesions can be detected by MRE with high accuracy, even in fibrotic livers [104]. Tomoelastography can also differentiate between benign and malignant liver lesions with high stiffness sensitivity and high specificity based on fluidity [105]. More information about the above and other applications of MRE in clinical investigations, such as viral hepatitis or portal hypertension, can be found here [92, 97, 100].

More and more elastographic procedures are being included in clinical guidelines for liver diagnosis. In particular, if one or more of the following factors are present, MRE is recommended: ascites, severely elevated ALT, BMI ≥ 30 kg/m² (Body Mass Index) [106].
The European Association for Study of Liver with the Asociacion Latinoamericana para el Estudio del Higado and the American Gastroenterological Association recommend elastography to evaluate liver fibrosis [107, 108]. American Association for the Study of Liver Diseases suggests MRE for fibrosis detection in patients with NAFLD [109], and the American College of Radiology's adequacy criteria for chronic liver disease describes MRE as the most accurate method for noninvasive diagnosis of liver fibrosis because it assesses the entire liver and can grade liver fibrosis by stages [110].

Liver elastography is an active area of research and needs standardization [97, 111]. It has been proposed for various purposes, such as monitoring stiffness, predicting liver complications, and detecting inflammation [111]. When changes in liver stiffness are observed, it is currently unclear whether they are related to fibrosis, inflammatory changes, venous congestion, or other factors when no other data are available [111]. Therefore, studies with paired biopsies are necessary to validate elastographic changes, but due to the risk of biopsies, they are rare in patients [111], making animal studies that can compare histology with elastography more important.

To understand the relationships between microarchitectural extracellular matrix (ECM) and cellular changes, the corresponding biophysical manifestations at the macroscopic image level, and the histological features reflecting the observed biophysical parameters, we decided to perform two basic *ex vivo* experiments in which liver tissue was altered only by physiological processes to study the structural changes of liver tissue and their biophysical effects without pathological complications.

3 Aims and Objectives of the thesis

The aim of this dissertation was to establish the relationship between the microstructure and biophysical properties of the *ex vivo* rat liver by investigating two hypotheses:

Hypothesis 1: Postmortem processes alter the structure of the liver tissue and its biophysical properties. These changes are time dependent, and the blood content of the tissue determines the rate of change.

Hypothesis 2: Physiological pregnancy leads to changes in the liver microstructure that affect biophysical parameters measured by MRE and DWI.

4 Research Publications in Journals with Peer-Review

4.1 Publication I

Title: Effect of Post-mortem Interval and Perfusion on the Biophysical Properties of *ex vivo* Liver Tissue Investigated Longitudinally by MRE and DWI

Authors: Garczyńska Karolina, Tzschätzsch Heiko, Assili Sanam, Kühl Anja A., Häckel Akvile, Schellenberger Eyk, Berndt Nikolaus, Holzhütter Hermann-Georg, Braun Jürgen, Sack Ingolf, Guo Jing

Journal: Frontiers in Physiology

Impact factor: 4.566

Volume: 12

Year: 2021

Published: 03 August 2021

URL: https://doi.org/10.3389/fphys.2021.696304

DOI: 10.3389/fphys.2021.696304

ISSN: 1664-042X

Citation: Garczyńska, K, Tzschätzsch H, Assili S, Kühl AA, Häckel A, Schellenberger E, Berndt N, Holzhütter H-G, Braun J, Sack I and Guo J (2021) Effect of Post-mortem Interval and Perfusion on the Biophysical Properties of *ex vivo* Liver Tissue Investigated Longitudinally by MRE and DWI. Front. Physiol. 12:696304. doi: 10.3389/fphys.2021.696304

4.1.1 Declaration of own portion of work in the research publication:

Contribution by K. Garczynska: conceptualization, preparation, completion and evaluation of the experiments, histological investigation, data acquisition, formal and statistical analysis, data curation, writing—original draft, editing, and visualization.

Contributions of other authors: HT: software, validation. AK: cooperation by histological investigation. HT, AK, SA, AH, ES, NB, and H-GH: writing—review and editing. JB: funding acquisition, resources, and methodology. IS: conceptualization, funding acquisition, resources, methodology, project administration, supervision, and critical revision of the manuscript. JG: conceptualization, formal analysis, funding acquisition, methodology, visualization, supervision, writing—original draft, writing—review and editing, and critical revision of the manuscript.

frontiers in Physiology

ORIGINAL RESEARCH
published: 03 August 2021
doi: 10.3389/fphys.2021.696304

Effect of Post-mortem Interval and Perfusion on the Biophysical Properties of *ex vivo* Liver Tissue Investigated Longitudinally by MRE and DWI

*Karolina Garczyńska[1,2], Heiko Tzschätzsch[1], Sanam Assili[1,3], Anja A. Kühl[4], Akvile Häckel[1], Eyk Schellenberger[1], Nikolaus Berndt[5,6], Hermann-Georg Holzhütter[6], Jürgen Braun[7], Ingolf Sack[1] and Jing Guo[1]**

[1] Department of Radiology, Berlin Institute of Health, Charité - Universitätsmedizin Berlin, Corporate Member of Freie Universität Berlin, Humboldt-Universität zu Berlin, Berlin, Germany, [2] Department of Veterinary Pathology, College of Veterinary Medicine, Freie Universität Berlin, Berlin, Germany, [3] Department of Biology, SUNY Albany, Albany, NY, United States, [4] iPATH.Berlin - Core Unit of Charité, Universitätsmedizin Berlin, Corporate Member of Freie Universität Berlin, Humboldt-Universität zu Berlin, Berlin, Germany, [5] Institute for Imaging Science and Computational Modelling in Cardiovascular Medicine, Berlin Institute of Health (BIH), Charité - Universitätsmedizin Berlin, Corporate Member of Freie Universität Berlin, Humboldt-Universität zu Berlin, Berlin, Germany, [6] Computational Systems Biochemistry Group, Institute of Biochemistry, Berlin Institute of Health (BIH), Charité - Universitätsmedizin Berlin, Corporate Member of Freie Universität Berlin, Humboldt-Universität zu Berlin, Berlin, Germany, [7] Institute of Medical Informatics, Berlin Institute of Health, Charité - Universitätsmedizin Berlin, Corporate Member of Freie Universität Berlin, Humboldt-Universität zu Berlin, Berlin, Germany

OPEN ACCESS

Edited by:
Wouter van Elmpt,
Maastricht University, Netherlands

Reviewed by:
Meng Yin,
Mayo Clinic, United States
Martina Guidetti,
Rush University Medical Center, United States

***Correspondence:**
Jing Guo
jing.guo@charite.de

Specialty section:
This article was submitted to Medical Physics and Imaging, a section of the journal Frontiers in Physiology

Received: *16 April 2021*
Accepted: *12 July 2021*
Published: *03 August 2021*

Citation:
Garczyńska K, Tzschätzsch H, Assili S, Kühl AA, Häckel A, Schellenberger E, Berndt N, Holzhütter H-G, Braun J, Sack I and Guo J (2021) Effect of Post-mortem Interval and Perfusion on the Biophysical Properties of ex vivo Liver Tissue Investigated Longitudinally by MRE and DWI. Front. Physiol. 12:696304. doi: 10.3389/fphys.2021.696304

Structural changes of soft tissues on the cellular level can be characterized by histopathology, but not longitudinally in the same tissue. Alterations of cellular structures and tissue matrix are associated with changes in biophysical properties which can be monitored longitudinally by quantitative diffusion-weighted imaging (DWI) and magnetic resonance elastography (MRE). In this work, DWI and MRE examinations were performed in a 0.5-Tesla compact scanner to investigate longitudinal changes in water diffusivity, stiffness and viscosity of ex-vivo rat livers for up to 20 h post-mortem (pm). The effect of blood on biophysical parameters was examined in 13 non-perfused livers (containing blood, NPLs) and 14 perfused livers (blood washed out, PLs). Changes in cell shape, cell packing and cell wall integrity were characterized histologically. In all acquisitions, NPLs presented with higher shear-wave speed *(c)*, higher shear-wave penetration rate *(a)* and smaller apparent-diffusion-coefficients (ADCs) than PL. Time-resolved analysis revealed three distinct phases: (i) an initial phase (up to 2 h pm) with markedly increased c and a and reduced ADCs; (ii) an extended phase with relatively stable values; and (iii) a degradation phase characterized by significant increases in *a* (10 h pm in NPLs and PLs) and ADCs (10 h pm in NPLs, 13 h pm in PLs). Histology revealed changes in cell shape and packing along with decreased cell wall integrity, indicating tissue degradation in NPLs and PLs 10 h pm. Taken together, our results demonstrate that the biophysical properties of fresh liver tissue rapidly change within 2 h pm, which seems to be an effect of both cytotoxic edema and vascular blood content.

Several hours later, disruption of cell walls resulted in higher water diffusivity and wave penetration. These results reveal the individual contributions of vascular components and cellular integrity to liver elastography and provide a biophysical, imaging-based fingerprint of liver tissue degradation.

Keywords: liver stiffness, viscosity, perfusion, degradation, magnetic resonance elastography (MRE), diffusion-weighted imaging (DWI), water diffusivity, post-mortem interval

INTRODUCTION

Changes in cellular and extracellular matrix (ECM) architecture associated with pathological or physiological processes affect the biophysical tissue properties that are visualized by medical imaging. However, the exact link between microarchitectural changes and the corresponding biophysical manifestations on the macroscopic imaging level is still elusive. Especially for the liver, where imaging of viscoelastic tissue properties by elastography has become a standard clinical procedure, a deeper understanding of the structure elements that determine the changes in macroscopic imaging properties is urgently needed (Mueller, 2020; Hudert et al., 2021).

Changes of the tissue's microarchitecture can be caused by either pathological factors (such as inflammation, fibrosis, etc.) or physiological factors (such as post-mortem cellular apoptosis, blood perfusion status, etc.). Post-mortem (pm) degeneration of biological tissues is a process that involves alterations of tissue composition and structure on many levels. The degree of *ex vivo* decomposition is determined by many factors, including the tissue type, post-mortem interval, temperature, and humidity (Oka, 1920; Otto et al., 1981; Milroy, 1999; Tomita et al., 2004). Earlier studies investigating the time course of tissue decomposition from biochemical and morphological perspectives have revealed changes in macro- and microstructures (Benda et al., 1957; Masshoff et al., 1964; Riede et al., 1976), glycogen concentration (Popper and Wozasek, 1932; Hertz, 1933; Nunley et al., 1973; Calder and Geddes, 1990), pH level and fat content (Shima, 1922; Sinapius, 1963; Donaldson and Lamont, 2013). In view of the structural and functional changes involved in the post-mortem degeneration process, serial characterization of the biophysical properties of *ex vivo* tissues by imaging with simultaneous histological validation could help us elucidate the link between imaging parameters and microscopic tissue structure.

Magnetic resonance imaging (MRI) has been employed to investigate the morphological and biophysical properties of *ex vivo* tissue specimens (Schneiderman et al., 2005; Tempel-Brami et al., 2015; Nebelung et al., 2016; Wolfram et al., 2020). In the context of tissue degradation, water diffusivity measured by diffusion-weighed imaging (DWI) has been revealed as a potential marker of post-mortem tissue alterations (Arthurs et al., 2015; Keller et al., 2018; Sapienza et al., 2019). Three studies investigating *ex vivo* brain tissue *in situ* have also demonstrated biomechanical properties quantified by magnetic resonance elastography (MRE) to be sensitive to instantaneous cerebral structural and functional changes occurring after death (Vappou et al., 2008; Weickenmeier et al., 2018; Bertalan et al., 2020). Although published studies provide imaging data on *ex vivo* tissue, most publications report results obtained at a single point in time. To our knowledge, data from systematic MRI studies of tissue without fixation over a long post-mortem interval (>10 h) are very limited (Keller et al., 2018; Sapienza et al., 2019). The recently introduced compact MRI device with MRE capability is an excellent tool for performing repeated examinations for the longitudinal investigation of *ex vivo* tissue samples (Braun et al., 2018; de Schellenberger et al., 2019; Sauer et al., 2019; Everwien et al., 2020; Garczyńska et al., 2020). The cylindrical sample tube utilized by this device ensures well-defined boundary conditions, which is beneficial for MRE analysis, and this technique has been shown to provide consistent values of stiffness and viscosity (Ipek-Ugay et al., 2015; Braun et al., 2018; Garczyńska et al., 2020).

In the present study, we used this compact MRI/MRE device to longitudinally investigate changes in the biophysical properties of *ex vivo* liver samples harvested from rats in a post-mortem interval of up to 20 h. In addition to the effect of the duration of the pm interval, we investigated the possible effect of the presence of blood on tissue decomposition by comparing the biophysical features of perfused and non-perfused liver samples. This was done because tissue perfusion is a common sample preparation step for histopathological analysis in science, especially for immunohistology (Scouten et al., 2006). Moreover, our imaging findings were supported by histological findings. Our foremost aim using this setup was to further the understanding of the underlying microscopic structural changes that manifest as macroscopic imaging features. Specifically, we quantified the apparent water diffusion coefficient (ADC) by DWI as well as stiffness-related shear wave speed (c) and viscosity-related shear wave penetration rate (a) by MRE in order to provide a specific fingerprint of the biophysical alterations of perfused and non-perfused liver tissue over time after death.

MATERIALS AND METHODS

All procedures involving animals were approved by the local authority (Landesamt für Gesundheit und Soziales Berlin, Reg. No. T0212/19) and were performed according to animal welfare regulations and institutional guidelines.

Sample Preparation

Livers were harvested from young adult female Wistar rats (Forschungseinrichtungen für Experimentelle Medizin, FEM, Berlin, Germany; Janvier Labs, Le Genest-Saint-Isle, France). All rats were kept in the same animal facility under standard housing

conditions for at least 3 days before imaging. In total, 41 rats were sacrificed and livers were harvested and randomly selected for two groups: (i) non-perfused liver (NPL, n_total = 20 with $n = 13$ for the MRE/DWI investigations and $n = 7$ for histology) and (ii) perfused liver (PL, n_total = 21 with $n = 14$ for the MRE/DWI investigations and $n = 7$ for histology).

To harvest the livers, the rats were first anesthetized with an overdose of isoflurane vapor. For the NPL group,

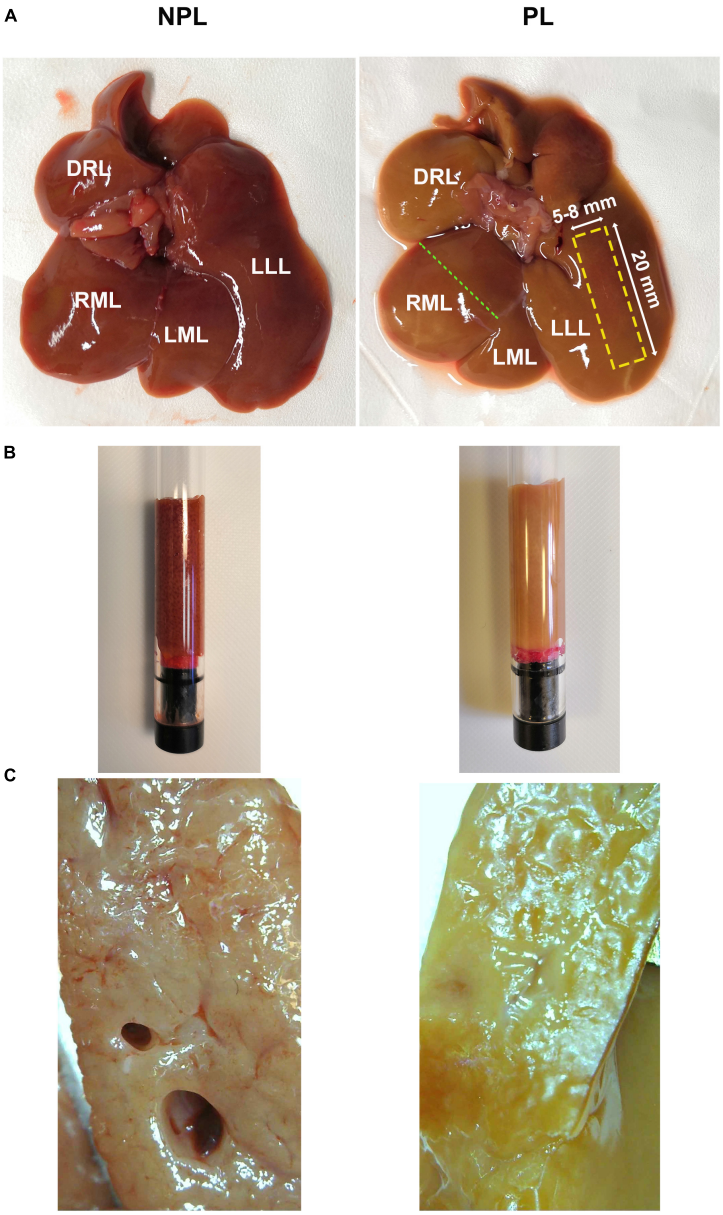

FIGURE 1 | (A) Photograph of fresh non-perfused livers (NPLs, left) and perfused livers (PLs, right); a rectangular area marked by a dashed yellow line indicates the site from which the sample for MRI was taken. The green dashed line indicates the position of the cross-sectional area shown in **(C)**. **(B)** Sample tubes containing liver tissue obtained from NPL and PL for DWI and MRE. **(C)** cross-sectional area of the liver showing more blood in the NPL sample (left) than in the PL sample (right). NPL, non-perfused liver; PL, perfused liver; LLL, left lateral lobe; LML, left middle lobe; RML, right middle lobe; DRL, dorsal right lobe.

the rats were decapitated with a rodent guillotine and the livers were removed without further processing. For the PL group, anesthesia was followed by exsanguinations, and the liver was perfused *in situ*. For liver perfusion, the portal vein (PV) was cannulated (20G Vasofix Safety IV Catheter, B. Braun, Melsungen, Germany) and the inferior vena cava (IVC) was severed and used as outflow. Blood was washed out using a peristaltic pump (MEDOREX TBE/200 62-4-3-3, MDX Biotechnik International, Nörten-Hardenberg, Germany), and circulating cells were removed from the liver by phosphate-buffered saline solution (PBS Tablets, Gibco, Thermo Fisher Scientific, Paisley, United Kingdom). Perfusion was stopped upon the observation of a non-decoloring liver with clear outflow. Average perfusion time was 13 min at a perfusion rate of approx. 40 ml/min and a total perfusate consumption of ˜700 ml.

For MR imaging, a cylindrical sample (8 mm Ø, 20 mm height) was cut out from the left lateral lobe of the liver and directly transferred into a glass tube, which was then inserted into a compact MRI device (Pure Devices GmbH, Würzburg, Germany) for imaging. Sample preparation time was 19 min for NPLs and 32 min for PLs (13 min extra for perfusion). As a result, MRI started 19 min pm for NPLs and 32 min pm for PLs.

Magnetic Resonance Elastography (MRE) and Diffusion-Weighted Imaging (DWI)

All imaging examinations were performed in a 0.5-T compact MRI device as mentioned above. For MRE measurements, an external gradient amplifier (DC 600, Pure Devices GmbH, Würzburg, Germany) and a piezo-actuator (PAHL60/20 Piezosystem Jena, Jena, Germany) coupled to the sample tube were implemented to the MRI device to provide mechanical vibrations. Details of the MRE setup are provided in Braun et al. (2018); de Schellenberger et al. (2019); Sauer et al. (2019); Everwien et al. (2020) and Garczyńska et al. (2020).

Imaging parameters for MRE and DWI were the same as described in Garczyńska et al. (2020). For MRE, one axial 3 mm slice with an in-plane resolution of 150 μm was acquired using a mechanical driving frequency of 800 Hz. The tissue deflection generated by the mechanical vibration was 0.67 μm. Eight time steps were recorded over a wave cycle within an acquisition time of 3 min. For DWI, the same slice with an in-plane resolution of 600 μm was acquired using seven b-values (50, 175, 300, 425, 550, 675, and 800 s/mm2), which took a total of 5 min. Data from MRE and DWI were repeatedly acquired in an interleaved manner up to 15 h pm. MRE was discontinued thereafter due to visible liquid accumulation between the liver tissue and the sample tube wall, which compromised contact and effectively hindered transfer of mechanical vibrations. Conversely, DWI acquisition, which does not require wave propagation, was continued until 20 h after death. To minimize the possible influence of temperature (Bertalan et al., 2019), the sample was kept at a constant temperature of 30°C throughout the imaging process by a built-in temperature control unit of the MRI scanner.

All imaging data were postprocessed using algorithms written in MATLAB (R2019b, The Mathwork Inc., Natick, MA, United States) as described previously in Braun et al. (2018) and de Schellenberger et al. (2019). MRE-based shear wave speed (c in m/s) and shear wave penetration rate (a in m/s) were derived using a Bessel function fit. c is a surrogate marker of tissue stiffness which can be converted to stiffness in kPa, assuming the elastic model, by ρc2 with ρ being the material's density of 1,000 kg/m^3. a is inversely correlated to viscous damping of shear waves. For DWI, maps of apparent diffusion coefficient (ADC), which quantifies water diffusivity, were generated with mono-exponential fitting using all seven b-values.

Histology

For histology, 14 additional rats (7 per group) were used, and liver tissue specimens from the left lateral lobe were investigated at three time points: fresh (immediately after death for NPLs and 13 min pm for PLs), 2 h pm, and 10 h pm. To ensure that the histologic features examined reflected the same intrinsic tissue properties of specimens subjected to MRE, all specimens assigned to histology were exposed to the same imaging protocols, including temperature and mechanical fluctuation. In order to

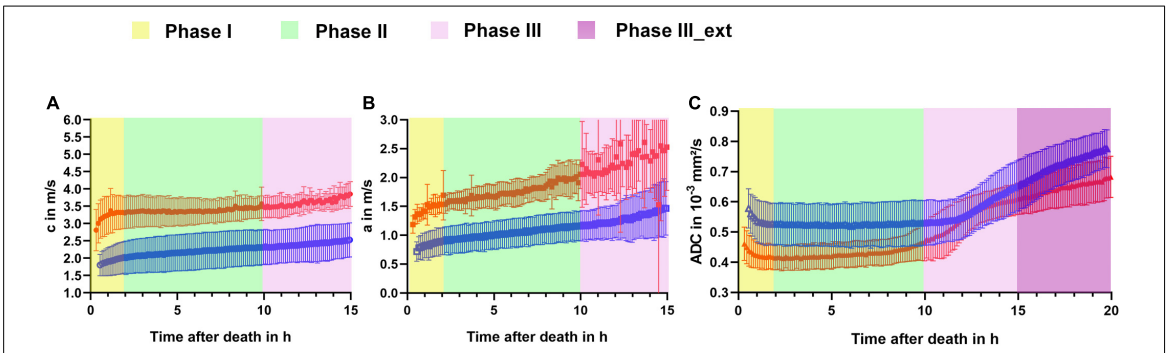

FIGURE 2 | Temporal evolution curves of group averages and standard deviations of **(A)** shear wave speed c, **(B)** penetration rate a, and **(C)** apparent diffusion coefficient ADC of non-perfused (red curve) and perfused (blue curve) liver with different colors indicating phases as defined in the text. NPL, non-perfused liver; PL, perfused liver.

minimize disturbance, each liver sample was divided into two portions separated in the sample tube by a small piece of foam earplug. After 1.5 h of MRI acquisition (2 h pm), the top liver portion was removed and prepared for histology while the bottom liver portion remained in the sample tube for another 8 h of MRI examinations and was finally removed for histology at 10 h pm. As the liver samples for histology were divided into 2 portions and were only imaged up to 10 h, the imaging data were not included in the final data analysis.

Tissue samples from all 3 time points were fixed in 4 % formaldehyde solution (Formalin Solution 4 %, J.T. Baker, Fisher Scientific, Avantor, Gliwice, Poland) at room temperature for 24 h. The fixed samples were processed as described earlier (Garczyńska et al., 2020). Paraffin sections of 2 μm thickness were stained with hematoxylin and eosin (H&E; Mayer's Hemalum Solution, Merck, Darmstadt, Germany; Eosin Y solution, Sigma-Aldrich, Darmstadt, Germany).

Images of stained sections were taken with a BZ-X800 fluorescence microscope (KEYENCE DEUTSCHLAND GmbH, Neu-Isenburg, Germany). For each time point, two high-power fields per sample were analyzed. Hepatocytes were counted per field of view (FoV) at 40x magnification in H&E-stained sections using ImageJ software version 1.52v (Schneider et al., 2012). Histological analysis was performed in a blinded manner.

Statistical Analysis

Mixed analysis of variance (ANOVA) was performed to account for the effects and interactions of two factors present in our data- acquisition time (within-subject factor) and perfusion status (between-subject factor; non-perfused vs. perfused) for all imaging parameters.

Dynamic responses of water diffusivity over time as quantified by ADC were fitted using the exponential model:

$$ADC = ADC_0 + (ADC_p - ADC_0) \times (1 - exp(-k \times t))$$

where ADC_0 and ADC_p are initial and plateau ADC values in mm^2/s, k is the rate constant in $hours^{-1}$, and t is acquisition time in hours.

Normality of the datasets was first assessed using the D'Agostino-Pearson normality test. Differences between groups were assessed using the unpaired *t*-test for data with normal distribution while the Mann-Whitney test was used for data without normal distribution.

P-values below 0.05 were considered statistically significant. Graphical and statistical analysis was performed with GraphPad Prism (GraphPad Prism 8.01. for Windows, GraphPad Software, San Diego, California, United States).[1]

RESULTS

General Characterization

The difference in appearances between NPL and PL samples is shown in **Figure 1**. PLs appeared paler and contained less blood

[1]www.graphpad.com

TABLE 1 | Summary of variation rates of MRI-based parameters (in %/h) in different post-mortem phases for non-perfused (NPL) and perfused (PL) livers and pairwise comparison of phases.

	Phase I		Phase II			Phase III			Phase III_ext			Comparison of phases	
	NPL	PL	NPL	PL	*P*	NPL	PL	*P*	NPL	PL	*P*	NPL	PL
c in %/h	2.88 ± 2.82	4.45 ± 5.13	0.65 ± 0.86	1.58 ± 0.41	≤ 0.01	1.59 ± 1.91	1.59 ± 1.41	0.99	/	/	/	P1 vs. P2: $p \leq 0.05$ P1 vs. P3: $p = 0.21$ P2 vs. P3: $p = 0.12$	P1 vs. P2: $p \leq 0.05$ P1 vs. P3: $p = 0.05$ P2 vs. P3: $p = 0.98$
a in %/h	4.99 ± 5.99	9.78 ± 3.94	≤ 0.05	2.85 ± 1.33	2.86 ± 0.66	0.98	4.09 ± 3.07	3.75 ± 2.40	0.75	/	/	P1 vs. P2: $p = 0.22$ P1 vs. P3: $p = 0.64$ P2 vs. P3: $p = 0.19$	P1 vs. P2: $p \leq 0.001$ P1 vs. P3: $p \leq 0.001$ P2 vs. P3: $p = 0.12$
ADC in %/h	−2.75 ± 1.57	−4.95 ± 2.77	≤ 0.05	1.23 ± 1.17	0.09 ± 0.43	≤ 0.01	4.65 ± 0.94	3.50 ± 1.99	0.07	2.12 ± 0.69	3.26 ± 1.22	≤ 0.01	P1vs. P2: $p \leq 0.001$ P1 vs. P3: $p \leq 0.001$ P2 vs. P3: $p \leq 0.001$ P1 vs. P3_ext: $p \leq 0.001$ P2 vs. P3_ext: $p \leq 0.01$ P3 vs. P3_ext: $p \leq 0.001$	P1 vs. P2: $p \leq 0.001$ P1 vs. P3: $p \leq 0.001$ P2 vs. P3: $p \leq 0.001$ P1 vs. P3_ext: $p \leq 0.001$ P2 vs. P3_ext: $p \leq 0.001$ P3 vs. P3_ext: $p = 0.69$

P1 = Phase I, P2 = Phase II, P3 = Phase III, P3_ext = extended Phase III (DWI).

than NPLs. Note that, as a result of incomplete perfusion, residual blood was still visible in PLs.

Magnetic Resonance Elastography

Time evolution curves of group averages and standard deviations (SDs) of shear wave speed *c* and penetration rate *a* for NPLs and PLs are presented in **Figure 2**. Both *c* (2.81 $\pm$ 0.60 m/s) and *a* (1.19 $\pm$ 0.15 m/s) were initially higher in NPLs than PLs (*c*: 1.80 $\pm$ 0.31 m/s; *a*: 0.72 $\pm$ 0.17 m/s); the difference was 35.94% ($p \leq 0.001$) and 39.50% ($p \leq 0.001$), respectively. Based on the development of parameters over time, we identified three distinct phases: Phase I from the start of the first imaging experiment to 2 h pm; Phase II from 2 to 10 h pm; and Phase III from 10 to 15 h pm. In Phase I, an initial increase in both *c* and *a* was observed in both NPLs and PLs. While the increase in *c* did not differ significantly between the two groups, the increase in *a* was more pronounced in the PL group (*c*: 2.88 $\pm$ 2.82 %/h for NPLs vs. 4.45 $\pm$ 5.13 %/h for PLs, $p = 0.34$; *a*: 4.99 $\pm$ 5.99 %/h for NPLs vs. 9.78 $\pm$ 3.94 %/h for PLs, $p \leq 0.05$). In Phase II, both *c* and *a* were relatively stable over time in both groups. For *c*, a significantly higher increase was observed in PLs (NPLs: 0.65 $\pm$ 0.86 %/h vs. PLs: 1.58 $\pm$ 0.41 %/h, $p \leq 0.01$). The increase in *a* was similar in both groups with 2.85 $\pm$ 1.33 %/h in NPLs and 2.86 $\pm$ 0.66 %/h in PLs ($p = 0.98$). In Phase III, both *c* and *a* increased continuously over time without a significant difference between the two groups (*c*: 1.59 $\pm$ 1.91 %/h for NPLs vs. 1.59 $\pm$ 1.41 %/h for PLs, $p = 0.99$; *a*: 4.09 $\pm$ 3.07 % for NPLs vs. 3.75 $\pm$ 2.40 %/h for PLs, $p = 0.75$). Interestingly, the SD of *a* increased notably in both NPLs and PLs compared to Phases I and II (SD: NPLs: 0.13 $\pm$ 0.07 m/s, PLs: 0.06 $\pm$ 0.03 m/s for Phase I vs. NPLs: 0.17 $\pm$ 0.05 m/s, PLs: 0.08 $\pm$ 0.01 m/s for Phase II vs. NPLs: 0.39 $\pm$ 0.31 m/s, PLs: 0.11 $\pm$ 0.09 m/s for Phase III, all $p \leq 0.001$). The rate of parameters variation was calculated by comparing the two values at the beginning and the end of each phase taking the phase duration into consideration. The SD of each phase was obtained by averaging the SD of each measurement point in the corresponding phase. All MRE results are presented in **Table 1**. The changes in MRE parameters over time are summarized in **Table 2**.

To analyze the influence of time after death and perfusion status on MRE parameters, mixed ANOVA analysis was performed separately for each of the three phases. First, in Phases I and II, the significantly higher values of *c* and *a* in NPLs than in PLs were found to be attributable to the factors time ($p \leq 0.001$) and perfusion status ($p \leq 0.001$) with a significant interaction between them (all $p \leq 0.01$). In Phase III, the two factors (i.e., time and perfusion status) continued to have a significant influence on both *c* and *a*, resulting in higher *c* and *a* values in NPLs than in PLs (all $p \leq 0.01$). Additionally, these two factors had independent effects on *c* and *a* with no significant interactions between them (*c*: $p = 0.90$; *a*: $p = 0.88$). All mixed ANOVA results are summarized in **Table 3**.

Diffusion-Weighted Imaging

As for MRE, we divided the period of DWI acquisition into different phases, based on group averaged apparent diffusion coefficient (ADC) curves over time as shown in **Figure 2C**. In addition to the three phases defined for MRE, an extended phase III, Phase III_ext, from 15 to 20 h pm was introduced due to the longer DWI acquisition interval. Based on initial ADC values, NPL samples demonstrated 26.08% lower water diffusivity than PL samples (NPLs: 0.46×10^{-3} $\pm$ 0.05 mm^2/s vs. PLs: 0.58×10^{-3} $\pm$ 0.07 mm^2/s, $p \leq 0.001$).

Contrary to MRE parameters, ADC values in Phase I decreased in both groups, and the decrease was more pronounced in the PL group (NPLs: -2.75 $\pm$ 1.57%/h vs. PLs: -4.95 $\pm$ 2.77%/h, $p \leq 0.05$). In Phase II, a 1.23 $\pm$ 1.17%/h increase in ADC was observed in NPLs while the ADC was almost unchanged in PLs (0.09 $\pm$ 0.43 %/h, $p \leq 0.01$). A marked increase in ADC was found for both groups in Phase III and III_ext. While the increase was not significantly different between NPLs and PLs in Phase III (NPLs: 4.65 $\pm$ 0.94%/h vs. PLs:

TABLE 2 | Main results of MRE, DWI and histological analysis in both non-perfused liver (NPL) and perfused liver (PL) samples at different phases and time points after death.

Method	Observation/parameter	Phase I		Phase II		Phase III	
		NPL	PL	NPL	PL	NPL	PL
MRE	*c*	↑	↑↑	↑	↑	↑	↑
	a	↑↑	↑↑↑	↑	↑	↑↑	↑↑
	ADC	↓	↓↓	↑	↔	↑↑	↑↑
		Fresh		2h post-mortem		10h post-mortem	
Histology	Hepatocyte organization	Tight	Loose	Loose, a few separated cells	Separated cells	Loose, separated cells	Separated cells
	Hepatocyte shape	Polygonal	Round	Round	Round + polygonal	Elongated	Elongated
	Cell wall visibility	High	High	Moderate	Moderate	Low	Moderate
	Glycogen amount	High	Low	Low	None	None	None

For the imaging parameters, relative changes are qualitatively indicated as increase (↑), decrease (↓), or unchanged (↔). The number of arrows indicates the degree of changes.

TABLE 3 | Summary of mixed model ANOVA results and initial values (means with SDs) in different phases during the acquisition interval in non-perfused liver (NPL) and perfused liver (PL) samples.

	Phase I			Phase II			Phase III			Phase III_ext		
	Initial value		Time Status Interaction	Initial value		Time Status Interaction	Initial value		Time Status Interaction	Initial value		Time Status Interaction
	NPL	PL		NPL	PL		NPL	PL		NPL	PL	
c *in m/s*	2.81 ± 0.60	1.80 ± 0.31	***	3.31 ± 0.45	2.03 ± 0.47	***	3.31 ± 0.45	2.32 ± 0.50	**	/	/	/
a *in m/s*	1.19 ± 0.15	0.72 ± 0.17	***	1.53 ± 0.15	0.90 ± 0.24	***	1.91 ± 0.31	1.16 ± 0.26	***	/	/	/
ADC *in 10^{-3} mm^2/s*	0.46 ± 0.05	0.58 ± 0.07	***	0.42 ± 0.04	0.53 ± 0.07	***	0.47 ± 0.06	0.53 ± 0.07	***	0.61 ± 0.05	0.65 ± 0.08	***

*NPLs (n = 13); PLs (n = 14); ns, non-significant, **$p \leq 0.01$, ***$p \leq 0.001$.*

3.50 ± 1.99%/h, $p = 0.07$), PLs exhibited a significantly higher increase than NPLs in Phase_III_ext (NPLs: 2.12 ± 0.69 %/h vs. PLs: 3.26 ± 1.22 %/h, $p \leq 0.01$). All averaged ADC values are summarized in **Table 1**. Changes in ADC in the three phases are provided in **Table 2**.

Mixed ANOVA was also performed to assess the effects of perfusion status and time after death on ADC. In all four phases, time after death had a significant effect on ADC values between the NPL and PL groups ($p \leq 0.001$) while the effect of perfusion status was only significant in Phases I, II, and III_ext (Phase I: $p \leq 0.001$; Phases II and III_ext: $p \leq 0.01$; Phase III: $p = 0.24$). The two factors considered in mixed ANOVA demonstrated significant interactions in all phases ($p \leq 0.001$) except Phase I ($p = 0.97$). All results of mixed ANOVA are presented in **Table 3**.

The ADC curves revealed a strong dynamic change during Phase III with different onset time between the NPL and PL groups. To better describe this change, exponential fitting as described in the Methods section was performed for each individual sample from Phase II to Phase III_ext.

In **Figure 3A**, the fitted curves for samples with the earliest and the latest onset of ADC increase in both NPLs and PLs are selectively shown. Comparison of the two groups showed the initial value, ADC_0, to be significantly higher in PLs than in NPLs (PLs: 0.53 × 10^{-3} ± 0.07 × 10^{-3} mm^2/s vs. NPLs: 0.43 × 10^{-3} ± 0.04 × 10^{-3} mm^2/s, $p \leq 0.001$, **Figure 3B**). Secondly, the averaged onset time for the ADC increase in the NPL group was significantly earlier than in the PL group (NPLs: 9.88 ± 1.29 h vs. PLs: 12.59 ± 1.78 h, $p \leq 0.001$, **Figure 3C**). Thirdly, rate constant *k*, which denotes the degree of ADC increase over time, was also significantly different between the NPL and PL groups (NPLs: 0.36 ± 0.17 h^{-1} vs. PLs: 0.23 ± 0.13 h^{-1}, $p \leq 0.05$, **Figure 3D**). The time range that covered the dynamic increase in ADC for all samples in the NPL group and the PL group was 3.19 and 6.53 h, respectively. All parameters obtained from model fitting were averaged for NPL and PL groups and are summarized in **Table 4**.

Histological Evaluation

Representative microscopic images of H&E-stained liver sections from PLs and NPLs at three time points are shown in **Figure 4**. The most prominent histological features of these samples can be described as follows: fresh NPL samples commonly displayed structural integrity with polygonal hepatocytes tightly organized in trabeculae. Additionally, a high amount of glycogen was present, seen as white spaces inside the cytoplasm of hepatocytes. Conversely, hepatocytes in fresh PL samples tended to appear roundish rather than polygonal. Although the trabecular arrangement was still visible, some hepatocytes already demonstrated detachment from the rest, resulting in a seemingly loosened packing. Furthermore, there was almost no glycogen visible in the fresh PL sample.

At 2 h pm, the histological appearance of the NPL sample was very similar to that of the fresh PL sample as described above, showing roundish hepatocytes which were loosely packed with no visible presence of glycogen. Comparatively in the PL sample, roundish hepatocytes displayed larger-scale separation and dissociation with almost no visible hepatocyte clusters. At

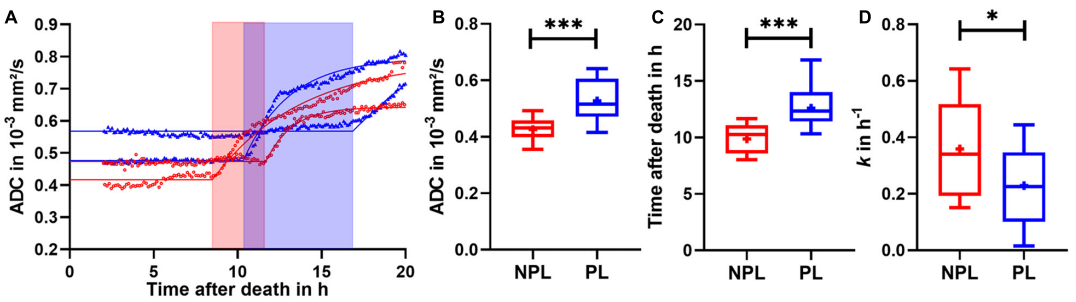

FIGURE 3 | (A) ADC data of two samples with the earliest and latest onset of ADC increase have been selected for illustration, separately for NPLs (red) and PLs (blue). Solid lines represent fitted curves using the exponential model. Colored blocks indicate the time duration of the observed ADC increase. Box plots of **(B)** ADC_0-initial fitted ADC values in mm^2/s **(C)** onset time of the ADC increase in hour and **(D)** *k*-rate constant in h^{-1}. Data are presented as minimum to maximum with interquartile range and median; + indicates means. *$p \leq 0.05$; ***$p \leq 0.001$. NPL, non-perfused liver; PL, perfused liver.

this time point, the nuclei appeared hyperchromatic in both NPL and PL samples, while the nuclei in the NPL sample additionally showed a slight size reduction.

At 10 h pm, the most prominent changes appearing in both the NPL and PL samples affected the shape and size of hepatocytes. In both groups, the formerly round hepatocytes observed at 2 h pm became elongated, taking on an ellipsoidal shape. Overall size of hepatocytes appeared to be smaller compared to 2 h pm. Additionally, cell walls appeared to become less distinct, making it harder to visually separate hepatocytes from one another. Furthermore, nuclei became smaller and exhibited signs of hyperchromasia and pyknosis. There was even evidence of karyorrhexis in the NPL sample. All histological findings are summarized in **Table 2**.

Hepatocytes per FoV at 40x magnification were counted at all three time points for both NPLs and PLs, and counts were further analyzed using the mixed ANOVA method. We found that the difference in cell counts between the NPL and PL groups was solely influenced by the time after death ($p \leq 0.01$) with no significant effect of perfusion status ($p = 0.98$, **Figure 5**). Mean cell counts for the two groups at the different time points were as follows: fresh, NPLs: 183 ± 41 vs. PLs: 189 ± 26; 2 h pm, NPLs: 189 ± 45 vs. PLs: 183 ± 24; 10 h pm, NPLs: 205 ± 56 vs. PLs: 204 ± 26.

DISCUSSION

In this study, we investigated longitudinal variation of two biophysical properties, water diffusion and viscoelasticity, of perfused (PLs) and non-perfused (NPLs) livers over a long post-mortem (pm) interval with a high sampling rate. Comparison of NPLs and PLs consistently revealed higher stiffness, better wave penetration, and lower water diffusivity in NPLs for all measurements. Furthermore, we observed a significant dependency of all imaging parameters in both groups on the time after death. These findings are summarized in **Table 2** and will be briefly discussed in the following paragraphs.

TABLE 4 | Summary of parameters from model fitting of DWI results averaged for non-perfused liver (NPL) and perfused liver (PL) samples.

	ADC_0—initial value in 10^{-3} mm^2/s	T—onset time in h	*K*—rate constant in h^{-1}	ADCp—plateau in 10^{-3} mm^2/s
NPL	0.43 ± 0.04	9.88 ± 1.29	0.36 ± 0.17	0.68 ± 0.08
PL	0.53 ± 0.07	12.59 ± 1.78	0.23 ± 0.13	0.98 ± 0.35

In both NPLs and PLs, the initial phase (Phase I) from immediately after death up to 2 h pm was characterized by the biological pattern of ischemia followed by hypoxia and anoxia, ultimately resulting in cytotoxic edema and hepatocytes swelling (Riede et al., 1976). It appears as if the enlarged hepatocytes created intracellular pressure and mechanical resistance (Bertalan et al., 2020) and formed a tightly packed and compact structure which mechanically manifested as increased stiffness and lower viscosity (i.e., higher wave penetration rate *a*). Furthermore, it is known from the literature that water mobility is restricted by cell walls, leading to diminished water diffusivity when extracellular water is shifted into the intracellular space (Le Bihan and Iima, 2015) e.g., during formation of cytotoxic edema. A similar finding of reduced ADC and increased stiffness was reported after induction of hypoxic-anoxic injury in the mouse brain (Bertalan et al., 2020). Arthurs et al. (2015) also observed a decrease in ADC values in the post-mortem liver. In addition to cytotoxic edema, blood coagulation could also contribute to higher stiffness and restricted water diffusivity (Berg, 1950; Clark et al., 1996; García-Manzano et al., 2001). The effect of coagulation should be more pronounced in NPLs than PLs; however, residual blood in PLs due to incomplete perfusion might also contribute to stiffening in NPLs. It is also worth mentioning that based on literature data, blood remains mostly fluid in the main vessels after sudden death (Mole, 1948; Berg, 1950; Haba et al., 1963; Takeichi et al., 1984, 1985, 1986; Jackowski et al., 2006; El alfy and Elhadidy, 2018), such as decapitation used in our study for the NPLs.

After the prominent changes observed in the initial phase, we identified a stable phase extending up to 10 h pm that was characterized by fairly small changes in stiffness, wave

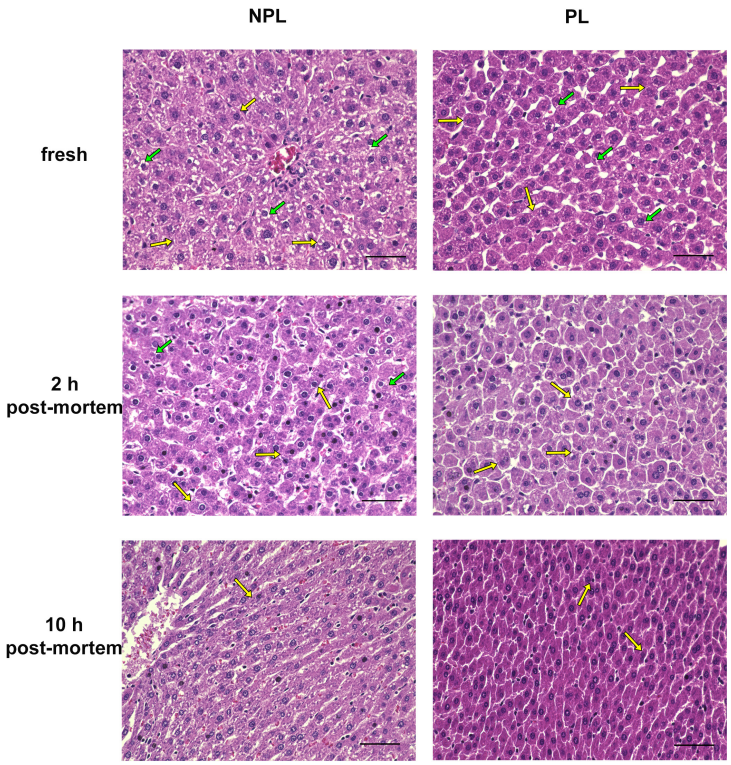

FIGURE 4 | Representative H&E-stained liver sections from NPLs and PLs collected immediately after death (fresh), 2 h post-mortem, and 10 h post-mortem. Scale bars correspond to 50 μm. NPL, non-perfused liver; PL, perfused liver. Arrows indicate examples for: glycogen (green) and cell wall (yellow).

penetration and water diffusivity in both NPLs and PLs. In this phase, there were no biophysical signs of major disruption of tissue integrity or cell breakdown.

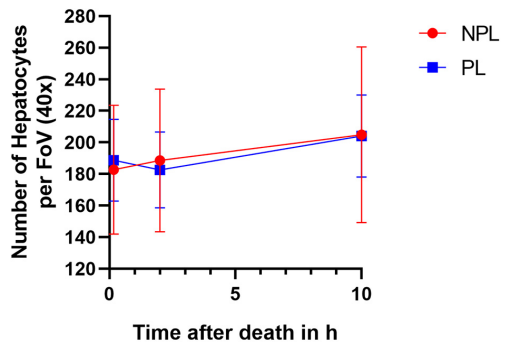

FIGURE 5 | Mean with SD of numbers of hepatocytes per field of view (FoV) counted at 40x optical field at three time points (fresh, 2 h post-mortem, and 10 h post-mortem) for both NPLs (n = 7) and PLs (n = 7). For each animal, two images were analyzed. NPL: non-perfused liver; PL: perfused liver.

After the stable phase, the penetration rate displayed a visible time dependency from 10 h to 15 h pm in both NPL and PL groups. Comparing histological images acquired at 2 h and 10 h pm, we suspected that the increase in penetration rate was a result of changes in cell shape with subsequent alteration in cell packing and reordering of the tissue lattice. In comparison to the fresh state, which was characterized by hepatocytes arranged in a tightly packed pattern, gradual elongation of hepatocytes over time seemed to create a more parallel-oriented packing arrangement. This arrangement of elongated hepatocytes appears to reduce intercellular friction, thus facilitating wave propagation. Similar to wave penetration rate, a significant increase in water diffusivity, indicating diminished restriction of water mobility, was observed from 10 h after death until the end of measurement. Considering that no decrease in stiffness was seen and cell walls were still visible in the histological images at 10 h pm, we hypothesize that the observed increase in water diffusivity is largely due to a gradual increase in cell membrane permeability rather than cell collapse and autolysis. Increased membrane permeability with a loss of membrane integrity is usually a process of tissue degradation which is followed by cell shrinkage and cell death (Majno et al., 1960; Kimura and Abe, 1994; Milroy, 1999; Yoon et al., 2002; Malhi et al., 2006;

Miller and Zachary, 2017; Yahia et al., 2018). Diffusivity started to increase earlier in NPLs, indicating faster tissue degradation in NPLs than PLs. Death induced anaerobic glycogenolysis during ischemia and anoxia produces a high amount of lactate, which leads to an acidic environment that is toxic to cells (Shima, 1922; Popper and Wozasek, 1932; Hertz, 1933; Nunley et al., 1973; Calder and Geddes, 1990; Donaldson and Lamont, 2013). Calder and Geddes (1990) reported the highest glycogen and lactate concentration in *ex vivo* livers of Wistar rats 30 min after death. Accumulation of lactate occurred in both NPLs and PLs in our study; however, due to perfusion, the high lactate-containing blood was replaced by PBS in PL samples, which apparently delayed the process of autolysis and tissue degeneration (Shima, 1922; Mukundan et al., 1986; George et al., 2016). We also found that the time window for observing such an increase in water diffusivity was narrower in NPLs than PLs, suggesting an inhomogeneity of residual blood remaining in PL vessels and leading to more heterogeneous tissue degradation in PLs. Additionally, the increase in cell membrane permeability and successive release of apoptogenic proteins and other small solutes might also function as intercellular lubricant that reduced friction and promoted wave propagation, as mentioned earlier. Since membrane permeability increases during tissue degradation, Phase III and the extended Phase III for DWI are considered to be degradation phases.

Despite the encouraging results, our study has limitations. First, no anticoagulant was used due to ethical restrictions in our study protocol. Therefore, we cannot rule out that some blood remained within the hepatic vessels. Second, the number of samples used for histological analysis was small so that the statistical power for cell counts was limited. Further studies investigating *ex vivo* tissue from other organs while controlling and varying factors such as medium osmolality, degree of cell hydration, and temperature levels are planned in order to gain deeper insights into autolysis and tissue decomposition and their biophysical manifestations.

To summarize, both MRE and DWI provided biophysical imaging parameters sensitive to structural alterations of rat livers during a cascade of biological events occurring after death. Throughout the 15-h pm interval investigated here, NPLs always showed higher stiffness, better penetration rate and lower water diffusivity than PLs. During this interval, three distinct phases were discernible - an initial phase with marked changes in biophysical properties up to 2 h pm, a stable phase up to 10 h pm, and a degradation phase characterized by significant increases in wave penetration and water diffusivity. As supported by histological results, these observed changes in biophysical parameters were closely related to variations in cell shape, cell packing patterns and cell wall integrity. Although obtained ex vivo, our results shed light on the individual contributions of vascular components and cellular integrity to liver biomechanical properties that can be quantified by elastography. In future applications of elastography, our results might support the interpretation of the biophysical signature related to liver tissue degradation.

DATA AVAILABILITY STATEMENT

The raw data supporting the conclusions of this article will be made available by the authors, without undue reservation.

ETHICS STATEMENT

The animal study was reviewed and approved by the Landesamt für Gesundheit und Soziales Berlin.

AUTHOR CONTRIBUTIONS

KG: conceptualization, data acquisition, investigation, formal analysis, data curation, writing—original draft, editing, and visualization. HT: software, validation, and writing—review and editing. AK: histological investigation, and writing, review and editing. SA, AH, ES, NB, and H-GH: writing—review and editing. JB: funding acquisition, resources, and methodology. IS: conceptualization, funding acquisition, resources, methodology, project administration, supervision, and critical revision of the manuscript. JG: conceptualization, data curation, formal analysis, funding acquisition, investigation, methodology, visualization, supervision, writing—original draft, writing—review and editing, and critical revision of the manuscript. All authors fully qualify for authorship and have approved the final version of the manuscript.

FUNDING

This work was supported by the Deutsche Forschungsgemeinschaft: SFB1340 Matrix in Vision (subprojects: A01, B07, B08, and C03) and BIOQIC graduate school. This work was also funded by the German Systems Biology Program "LiSyM," grant no. 31L0057, sponsored by the German Federal Ministry of Education and Research (BMBF).

ACKNOWLEDGMENTS

We acknowledge support from the German Research Foundation (DFG) and the Open Access Publication Fund of Charité—Universitätsmedizin Berlin.

REFERENCES

Arthurs, O. J., Price, G. C., Carmichael, D. W., Jones, R., Norman, W., Taylor, A. M., et al. (2015). Diffusion-weighted perinatal postmortem magnetic resonance imaging as a marker of postmortem interval. *Eur. Radiol.* 25, 1399–1406. doi: 10.1007/s00330-014-3525-y

Benda, L., Rissel, E., and Thaler, H. (1957). Über das histologische Bild der Leberdystrophie und seine Beeinflussung durch agonale und postmortale

Vorgänge. *Virchows Arch. Pathol. Anat. Physiol. Klin. Med.* 330, 594–607. doi: 10.1007/bf00954944

Berg, S. P. (1950). Das postmortale Verhalten des Blutes. *Dtsch. Z. Gesamte Gerichtl. Med.* 40, 1–75. doi: 10.1007/bf00706022

Bertalan, G., Boehm-Sturm, P., Schreyer, S., Morr, A. S., Steiner, B., Tzschätzsch, H., et al. (2019). The influence of body temperature on tissue stiffness, blood perfusion, and water diffusion in the mouse brain. *Acta Biomater.* 96, 412–420. doi: 10.1016/j.actbio.2019.06.034

Bertalan, G., Klein, C., Schreyer, S., Steiner, B., Kreft, B., Tzschatzsch, H., et al. (2020). Biomechanical properties of the hypoxic and dying brain quantified by magnetic resonance elastography. *Acta Biomater.* 101, 395–402. doi: 10.1016/j.actbio.2019.11.011

Braun, J., Tzschatzsch, H., Korting, C., Ariza de Schellenberger, A., Jenderka, M., Driessle, T., et al. (2018). A compact 0.5 T MR elastography device and its application for studying viscoelasticity changes in biological tissues during progressive formalin fixation. *Magn. Reson. Med.* 79, 470–478. doi: 10.1002/mrm.26659

Calder, P. C., and Geddes, R. (1990). Post mortem glycogenolysis is a combination of phosphorolysis and hydrolysis. *Int. J. Biochem.* 22, 847–856. doi: 10.1016/0020-711x(90)90288-e

Clark, M. A., Worrell, M. B., and Pless, J. E. (1996). "Post mortem changes in soft tissues," in *Forensic Taphonomy: the Postmortem Fate of Human Remains*, 1st Edn, eds W. D. Haglund and M. H. Sorg (Boca Raton, FL: CRC Press), 151–164.

de Schellenberger, A. A., Tzschatzsch, H., Polchlopek, B., Bertalan, G., Schrank, F., Garczynska, K., et al. (2019). Sensitivity of multifrequency magnetic resonance elastography and diffusion-weighted imaging to cellular and stromal integrity of liver tissue. *J. Biomech.* 88, 201–208. doi: 10.1016/j.jbiomech.2019.03.037

Donaldson, A. E., and Lamont, I. L. (2013). Biochemistry changes that occur after death: potential markers for determining post-mortem interval. *PloS One* 8:e82011. doi: 10.1371/journal.pone.0082011

El alfy, M., and Elhadidy, M. (2018). Biochemical Identifiers of Postmortem Time Interval on Autopsy of Albino Rats versus Physiological One. Global Journal of Medical Research. 18.

Everwien, H., Ariza de Schellenberger, A., Haep, N., Tzschätzsch, H., Pratschke, J., Sauer, I. M., et al. (2020). Magnetic resonance elastography quantification of the solid-to-fluid transition of liver tissue due to decellularization. *J. Mech. Behav. Biomed. Mater.* 104:103640. doi: 10.1016/j.jmbbm.2020.103640

García-Manzano, A., González-Llaven, J., Lemini, C., and Rubio-Póo, C. (2001). Standardization of rat blood clotting tests with reagents used for humans. *Proc. West Pharmacol. Soc.* 44, 153–155.

Garczyńska, K., Tzschätzsch, H., Kühl, A. A., Morr, A. S., Lilaj, L., Häckel, A., et al. (2020). Changes in liver mechanical properties and water diffusivity during normal pregnancy are driven by cellular hypertrophy. *Front. Physiol.* 11:605205. doi: 10.3389/fphys.2020.605205

George, J., Van Wettere, A. J., Michaels, B. B., Crain, D., and Lewbart, G. A. (2016). Histopathologic evaluation of postmortem autolytic changes in bluegill (*Lepomis macrohirus*) and crappie (*Pomoxis anularis*) at varied time intervals and storage temperatures. *PeerJ* 4:e1943. doi: 10.7717/peerj.1943

Haba, K., Kumano, O., Mohri, M., Takemaru, H., Kawanishi, K., Tobe, S., et al. (1963). Post mortem activation of human blood fibrinolytic enzyme in sudden and natural deaths. *Acta Med. Okayama* 17, 279–288.

Hertz, W. (1933). Der postmortale Glykogenschwund in der Leber von menschlichen Neugeborenen und Feten. *Z. Kinderheilkd.* 55, 410–420. doi: 10.1007/bf02252148

Hudert, C. A., Tzschätzsch, H., Rudolph, B., Loddenkemper, C., Holzhütter, H-G, Kalveram, L., et al. (2021). How histopathologic changes in pediatric nonalcoholic fatty liver disease influence in vivo liver stiffness. *Acta biomaterialia.* 123, 178–186.

Ipek-Ugay, S., Driessle, T., Ledwig, M., Guo, J., Hirsch, S., Sack, I., et al. (2015). Tabletop magnetic resonance elastography for the measurement of viscoelastic parameters of small tissue samples. *J. Magn. Reson.* 251, 13–18. doi: 10.1016/j.jmr.2014.11.009

Jackowski, C., Thali, M., Aghayev, E., Yen, K., Sonnenschein, M., Zwygart, K., et al. (2006). Postmortem imaging of blood and its characteristics using MSCT and MRI. *Int. J. Legal Med.* 120, 233–240. doi: 10.1007/s00414-005-0023-4

Keller, S., Schmidt, T. M., Kim, A. C., Fischer, R., Heinemann, A., Adam, G., et al. (2018). Postmortem MR diffusion-weighted imaging of the liver: time-behavior of the hepatic apparent diffusion coefficient in the early death interval. *Int. J. Legal Med.* 132, 263–268. doi: 10.1007/s00414-017-1685-4

Kimura, M., and Abe, M. (1994). Histology of postmortem changes in rat livers to ascertain hour of death. *Int. J. Tissue React.* 16, 139–150.

Le Bihan, D., and Iima, M. (2015). Diffusion magnetic resonance imaging: what water tells us about biological tissues. *PloS Biol.* 13:e1002203. doi: 10.1371/journal.pbio.1002203

Majno, G., La Gattuta, M., and Thompson, T. E. (1960). Cellular death and necrosis: chemical, physical and morphologic changes in rat liver. *Virchows Arch. Pathol. Anat. Physiol. Klin. Med.* 333, 421–465. doi: 10.1007/bf00955327

Malhi, H., Gores, G. J., and Lemasters, J. J. (2006). Apoptosis and necrosis in the liver: a tale of two deaths? *Hepatology* 43(2 Suppl. 1), S31–S44.

Masshoff, W., Lindlar, F., and Stolpmann, H. J. (1964). Morphologische und lipidchemische Untersuchungen zur Autolyse von Leber und Pankreas. *Virchows Arch. Pathol. Anat. Physiol. Klin. Med.* 337, 340–352. doi: 10.1007/bf00957666

Miller, M. A., and Zachary, J. F. (2017). "Chapter 1–mechanisms and morphology of cellular injury, adaptation, and death11for a glossary of abbreviations and terms used in this chapter see E-Glossary 1-1," in *Pathologic Basis of Veterinary Disease*, 6th Edn, ed. J. F. Zachary (Maryland Heights, MO: Mosby), 2.e–43.e.

Milroy, C. M. (1999). Forensic taphonomy: the postmortem fate of human remains. *BMJ* 319:458.

Mole, R. H. (1948). Fibrinolysin and the fluidity of the blood post mortem. *J. Pathol. Bacteriol.* 60, 413–427. doi: 10.1002/path.1700600308

Mukundan, M. K., Antony, P. D., and Nair, M. R. (1986). A review on autolysis in fish. *Fish. Res.* 4, 259–269. doi: 10.1016/0165-7836(86)90007-x

Mueller, S. (2020). *Liver Elastography Clinical Use and Interpretation* (ChamS: Springer), XIX, 737.

Nebelung, S., Tingart, M., Pufe, T., Kuhl, C., Jahr, H., and Truhn, D. (2016). Ex vivo quantitative multiparametric MRI mapping of human meniscus degeneration. *Skeletal Radiol.* 45, 1649–1660. doi: 10.1007/s00256-016-2480-x

Nunley, W. C., Dickie, M. W., and Schuit, K. E. (1973). Delayed, in vivo hepatic postmortem autolysis. *Virchows Archiv B Cell Pathol.* 14, 285–291.

Oka. (1920). Zur Frage der postmortalen autolyse der zellgranula. *Virchows Arch. Pathol. Anat. Physiol. Klin. Med.* 228, 200–215. doi: 10.1007/bf01993804

Otto, G., Kemmer, C., Wolff, H., and David, H. (1981). Elektronenmikroskopische befunde während hypothermer Lagerungskonservierung der Leber. *Langenbecks Arch. Chir.* 354, 117–123. doi: 10.1007/bf01271159

Popper, H., and Wozasek, O. (1932). Zur Kenntnis des Glykogengehaltes der Leichenleber. III. *Z. Gesamte Exp. Med.* 83, 682–710. doi: 10.1007/bf02598846

Riede, U. N., Lobinger, A., Grünholz, D., Steimer, R., and Sandritter, W. (1976). Einfluß einer einstündigen Autolyse auf die quantitative Zytoarchitektur der Rattenleberzelle (Eine ultrastrukturell-morphometrische Studie). *Beitr. Pathol.* 157, 391–411. doi: 10.1016/s0005-8165(76)80052-2

Sapienza, D., Asmundo, A., Silipigni, S., Barbaro, U., Cinquegrani, A., Granata, F., et al. (2019). Quantitative MRI molecular imaging in the evaluation of early post mortem changes in muscles. A feasibility study on a pig phantom. *arXiv* [Preprint] arXiv:1903.02346,

Sauer, F., Oswald, L., Ariza de Schellenberger, A., Tzschatzsch, H., Schrank, F., Fischer, T., et al. (2019). Collagen networks determine viscoelastic properties of connective tissues yet do not hinder diffusion of the aqueous solvent. *Soft Matter.* 15, 3055–3064. doi: 10.1039/c8sm02264j

Schneider, C. A., Rasband, W. S., and Eliceiri, K. W. (2012). NIH Image to ImageJ: 25 years of image analysis. *Nat. Methods* 9, 671–675. doi: 10.1038/nmeth.2089

Schneiderman, J., Wilensky, R. L., Weiss, A., Samouha, E., Muchnik, L., Chen-Zion, M., et al. (2005). Diagnosis of thin-cap fibroatheromas by a self-contained intravascular magnetic resonance imaging probe in ex vivo human aortas and in situ coronary arteries. *J. Am. Coll. Cardiol.* 45, 1961–1969. doi: 10.1016/j.jacc.2004.09.080

Scouten, C. W., O'Connor, R., and Cunningham, M. (2006). Perfusion fixation of research animals. *Micros. Today.* 14, 26–33. doi: 10.1017/s1551929500057631

Shima, S. (1922). Studies of autolysis. *J. Biochem.* 2, 1–26. doi: 10.1093/oxfordjournals.jbchem.a125828

Sinapius, D. (1963). Die Fette der Leichenleber bei spontaner und künstlicher Autolyse. *Virchows Arch. Pathol. Anat. Physiol. Klin. Med.* 337, 215–230. doi: 10.1007/bf00958160

Takeichi, S., Tokunaga, I., Hayakumo, K., and Maeiwa, M. (1986). Fluidity of cadaveric blood after sudden death: part III. Acid-base balance and fibrinolysis. *Am. J. Forensic Med. Pathol.* 7, 35–38. doi: 10.1097/00000433-198603000-00007

Takeichi, S., Wakasugi, C., and Shikata, I. (1984). Fluidity of cadaveric blood after sudden death: part I. Postmortem fibrinolysis and plasma catecholamine level. *Am. J. Forensic Med. Pathol.* 5, 223–227. doi: 10.1097/00000433-198409000-00006

Takeichi, S., Wakasugi, C., and Shikata, I. (1985). Fluidity of cadaveric blood after sudden death: part II. Mechanism of release of plasminogen activator from blood vessels. *Am. J. Forensic Med. Pathol.* 6, 25–29. doi: 10.1097/00000433-198503000-00006

Tempel-Brami, C., Schiffenbauer, Y. S., Nyska, A., Ezov, N., Spector, I., Abramovitch, R., et al. (2015). Practical applications of in Vivo and ex Vivo MRI in toxicologic pathology using a novel high-performance compact MRI system. *Toxicol. Pathol.* 43, 633–650. doi: 10.1177/0192623314568390

Tomita, Y., Nihira, M., Ohno, Y., and Sato, S. (2004). Ultrastructural changes during in situ early postmortem autolysis in kidney, pancreas, liver, heart and skeletal muscle of rats. *Leg. Med.* 6, 25–31. doi: 10.1016/j.legalmed.2003.09.001

Vappou, J., Breton, E., Choquet, P., Willinger, R., and Constantinesco, A. (2008). Assessment of in vivo and post-mortem mechanical behavior of brain tissue using magnetic resonance elastography. *J. Biomech.* 41, 2954–2959. doi: 10.1016/j.jbiomech.2008.07.034

Weickenmeier, J., Kurt, M., Ozkaya, E., de Rooij, R., Ovaert, T. C., Ehman, R. L., et al. (2018). Brain stiffens post mortem. *J. Mech. Behav. Biomed. Mater.* 84, 88–98. doi: 10.1016/j.jmbbm.2018.04.009

Wolfram, F., Böttcher, J., and Lesser, T. G. (2020). MR imaging of pulmonary lung nodules during one lung flooding: first morphological evaluation using an ex vivo human lung model. *Magma* 33, 537–547. doi: 10.1007/s10334-020-00826-8

Yahia, D., El-Amir, Y. O., and Sadek, A. A. I. (2018). Early postmortem biochemical and histopathological changes in the kidney, liver, and muscles of dogs. *Comp. Clin. Pathol.* 27, 1447–1455. doi: 10.1007/s00580-018-2756-8

Yoon, H.-W., Yoon, C.-G., and Cho, H.-G. (2002). Hepatic cell membrane changes of rats in the early postmortem period. *J. Biomed. Lab. Sci.* 8, 89–93.

Conflict of Interest: The authors declare that the research was conducted in the absence of any commercial or financial relationships that could be construed as a potential conflict of interest.

Publisher's Note: All claims expressed in this article are solely those of the authors and do not necessarily represent those of their affiliated organizations, or those of the publisher, the editors and the reviewers. Any product that may be evaluated in this article, or claim that may be made by its manufacturer, is not guaranteed or endorsed by the publisher.

4.2 Publication II

Title: Changes in Liver Mechanical Properties and Water Diffusivity During Normal Pregnancy Are Driven by Cellular Hypertrophy

Authors: Garczyńska Karolina, Tzschätzsch Heiko, Kühl Anja A., Morr Anna Sophie, Lilaj Ledia, Häckel Akvile, Schellenberger Eyk, Berndt Nikolaus, Holzhütter Hermann-Georg, Braun Jürgen, Sack Ingolf, Guo Jing

Journal: Frontiers in Physiology

Impact factor: 4.566

Volume: 11

Year: 2020

Published: 23 November 2020

URL: https://doi.org/10.3389/fphys.2020.605205

DOI: 10.3389/fphys.2020.605205

ISSN: 1664-042X

Citation: Garczyńska K, Tzschätzsch H, Kühl AA, Morr AS, Lilaj L, Häckel A, Schellenberger E, Berndt N, Holzhütter H-G, Braun J, Sack I and Guo J (2020) Changes in Liver Mechanical Properties and Water Diffusivity During Normal Pregnancy Are Driven by Cellular Hypertrophy. Front. Physiol. 11:605205. doi: 10.3389/fphys.2020.605205

4.2.1 Declaration of own portion of work in the research publication:

Contribution by K. Garczynska: conceptualization, preparation, completion and evaluation of the experiments, histological investigation, data acquisition, formal and statistical analysis, data curation, writing—original draft, editing, and visualization.

Contributions of other authors: HT and LL: software, validation. AK: cooperation in histological investigation. A-SM: help in completion of experiments. HT, LL, AK, A-SM, SA, AH, ES, NB, and H-GH: writing—review and editing. JB: funding acquisition, resources, and methodology. IS: conceptualization, funding acquisition, resources, methodology, project administration, supervision, and critical revision of the manuscript. JG: conceptualization, formal analysis, funding acquisition, methodology, visualization, supervision, writing—original draft, writing—review and editing, and critical revision of the manuscript.

frontiers in Physiology

ORIGINAL RESEARCH
published: 23 November 2020
doi: 10.3389/fphys.2020.605205

Changes in Liver Mechanical Properties and Water Diffusivity During Normal Pregnancy Are Driven by Cellular Hypertrophy

*Karolina Garczyńska[1], Heiko Tzschätzsch[1], Anja A. Kühl[2], Anna Sophie Morr[1], Ledia Lilaj[1], Akvile Häckel[1], Eyk Schellenberger[1], Nikolaus Berndt[3,4], Hermann-Georg Holzhütter[4], Jürgen Braun[5], Ingolf Sack[1] and Jing Guo[1]**

[1] Department of Radiology, Charité – Universitätsmedizin Berlin, Corporate Member of Freie Universität Berlin, Humboldt-Universität zu Berlin, and Berlin Institute of Health, Berlin, Germany, [2] iPATH.Berlin Core Unit, Charitá – Universitätsmedizin Berlin, Corporate Member of Freie Universität Berlin, Humboldt-Universität zu Berlin, and Berlin Institute of Health, Berlin, Germany, [3] Institute for Imaging Science and Computational Modelling in Cardiovascular Medicine, Charité – Universitätsmedizin Berlin, Corporate Member of Freie Universität Berlin, Humboldt-Universität zu Berlin, and Berlin Institute of Health, Berlin, Germany, [4] Computational Systems Biochemistry Group, Institute of Biochemistry, Charité – Universitätsmedizin Berlin, Corporate Member of Freie Universität Berlin, Humboldt-Universität zu Berlin, and Berlin Institute of Health, Berlin, Germany, [5] Institute of Medical Informatics, Charité – Universitätsmedizin Berlin, Corporate Member of Freie Universität Berlin, Humboldt-Universität zu Berlin, and Berlin Institute of Health, Berlin, Germany*

OPEN ACCESS

Edited by:
Simo Saarakkala, University of Oulu, Finland

Reviewed by:
Simon Auguste Lambert, Université Claude Bernard Lyon 1, France
Sebastian Mueller, Heidelberg University, Germany

***Correspondence:**
Jing Guo
jing.guo@charite.de

Specialty section:
This article was submitted to Medical Physics and Imaging, a section of the journal Frontiers in Physiology

Received: *11 September 2020*
Accepted: *29 October 2020*
Published: *23 November 2020*

Citation:
Garczyńska K, Tzschätzsch H, Kühl AA, Morr AS, Lilaj L, Häckel A, Schellenberger E, Berndt N, Holzhütter H-G, Braun J, Sack I and Guo J (2020) Changes in Liver Mechanical Properties and Water Diffusivity During Normal Pregnancy Are Driven by Cellular Hypertrophy. Front. Physiol. 11:605205. doi: 10.3389/fphys.2020.605205

During pregnancy, the body's hyperestrogenic state alters hepatic metabolism and synthesis. While biochemical changes related to liver function during normal pregnancy are well understood, pregnancy-associated alterations in biophysical properties of the liver remain elusive. In this study, we investigated 26 *ex vivo* fresh liver specimens harvested from pregnant and non-pregnant rats by diffusion-weighted imaging (DWI) and magnetic resonance elastography (MRE) in a 0.5-Tesla compact magnetic resonance imaging (MRI) scanner. Water diffusivity and viscoelastic parameters were compared with histological data and blood markers. We found livers from pregnant rats to have (i) significantly enlarged hepatocytes ($26 \pm 15\%$, $p < 0.001$), (ii) increased liver stiffness ($12 \pm 15\%$, $p = 0.012$), (iii) decreased viscosity ($-23 \pm 14\%$, $p < 0.001$), and (iv) increased water diffusivity ($12 \pm 11\%$, $p < 0.001$). In conclusion, increased stiffness and reduced viscosity of the liver during pregnancy are mainly attributable to hepatocyte enlargement. Hypertrophy of liver cells imposes fewer restrictions on intracellular water mobility, resulting in a higher hepatic water diffusion coefficient. Collectively, MRE and DWI have the potential to inform on structural liver changes associated with pregnancy in a clinical context.

Keywords: liver stiffness, viscosity, pregnancy, hypertrophy, magnetic resonance elastography (MRE), diffusion weighted imaging (DWI), water diffusion, hepatomegaly

INTRODUCTION

Pregnancy is a dynamic process involving a series of maternal physiological changes and adaptations that occur to support fetal growth and development. The changes are driven by maternal and placental hormones (estrogen, progesterone, prolactin, and others; Napso et al., 2018) and require considerable morphological and physiological flexibility of the maternal body, both

locally and systemically (Moll, 2001; Baeyens et al., 2016; Soma-Pillay et al., 2016; Napso et al., 2018).

The liver is the largest gland in the human body and plays a central role in metabolism. Hepatocytes participate, inter alia, in glucose, lipid, protein, and peptide metabolism (Pedrycz et al., 2014). As a central metabolic organ, the maternal liver undergoes significant changes induced by higher estrogen levels during normal pregnancy. In early pregnancy, when fetal demands are still relatively low, the maternal body stores energy through increased glucose intake and lipogenesis, as well as glycogen accumulation in hepatocytes to prepare for the higher energy consumption by the developing fetus in late gestation. Therefore, maternal cholesterol, triglyceride, and phospholipid levels are elevated from the second trimester until the end of pregnancy (Bacq, 2000–2013; Lain and Catalano, 2007; Pedrycz et al., 2014; Soma-Pillay et al., 2016; Zhang et al., 2017; Napso et al., 2018). In light of these known physiological changes, adjusted standard reference levels of serum markers have been defined for pregnant women (Abbassi-Ghanavati et al., 2009; Jamjute et al., 2009).

In addition, pregnancy-related adaptation of the maternal liver also involves changes in the organ's biomechanical properties (Ammon et al., 2018; Stenberg Ribeiro et al., 2019). Elastography can quantify biomechanical properties such as stiffness and viscosity of the liver *in vivo*. Studies of pregnant women using ultrasound-based elastography reported that liver stiffness increased during normal pregnancy and returned to baseline values after delivery (Ammon et al., 2018; Stenberg Ribeiro et al., 2019) where intraabdominal pressure was considered an imported contributor. Additionally, it was shown that changes in liver stiffness related to normal pregnancy differed from those caused by pregnancy-related liver disorders such as pre-eclampsia (Frank Wolf et al., 2016; Ammon et al., 2018) and intrahepatic cholestasis of pregnancy (IHC; Cetin et al., 2017). These results indicate that elastography sensitively detects mechanical changes of the liver during pregnancy. However, due to a lack of histological evidence, the underlying biological causes of altered hepatic stiffness during pregnancy are not fully understood, the authors only hypothesized on a possible association of increased stiffness with altered liver perfusion and intra-abdominal pressure during pregnancy.

Magnetic resonance elastography (MRE), an emerging elastography modality based on magnetic resonance imaging (MRI), can quantify the mechanical properties of soft tissues both *in vivo* and *ex vivo*. A compact MRE modality tailored to *ex vivo* tissue investigation of small cylindrical samples has been introduced recently (Ipek-Ugay et al., 2015; Braun et al., 2018; de Schellenberger et al., 2019; Sauer et al., 2019; Everwien et al., 2020). This compact MRE technique enforces well-controlled (cylindrical) boundary conditions permitting analytical solutions of the inverse problem in MRE by utilizing Bessel function. As a result, compact MRE has been shown to provide consistent values of stiffness and attenuation (shear elasticity and shear viscosity) with little degradation by noise. Moreover, MRE examinations can be combined with determination of other quantitative MRI parameters including water diffusion. In order to correlate pregnancy-related biomechanical changes with underlying biology, we used compact MRE (Ipek-Ugay et al., 2015; Braun et al., 2018; de Schellenberger et al., 2019; Sauer et al., 2019; Everwien et al., 2020) to investigate changes in stiffness and viscosity of *ex vivo* liver samples harvested from pregnant rats. With *ex vivo* samples, we examine mainly the dependency of mechanical properties on the underlying microarchitecture of the liver without influence from blood perfusion, which could be a confounding factor. MRE results were paired with diffusion-weighted imaging (DWI) to investigate the effect of pregnancy on hepatic water diffusivity. The water transport and viscoelasticity quantified by MRE and DWI, respectively, provided complementary information that are sensitive to the microstructure of biological tissues.

In addition, we performed extensive histological and biochemical analyses to elucidate possible structural causes of MRE and DWI parameter changes due to pregnancy. Our MRE results might shed light on clinically relevant biophysical changes of the liver detected by ultrasound elastography in pregnant women, however, one must take into consideration the difference between the two imaging modalities in terms of frequency range and data acquisition technique when comparing data obtained from MRE and ultrasound elastography.

MATERIALS AND METHODS

All procedures involving animals were approved by the local authority (Landesamt für Gesundheit und Soziales Berlin, Reg. No. T0280/10, T0212/19) and were performed according to institutional guidelines.

Sample Preparation

Livers were harvested from young adult female Wistar rats (Forschungseinrichtungen für Experimentelle Medizin, FEM, Berlin, Germany; Janvier Labs, Le Genest-Saint-Isle, France) of two groups: (i) pregnant group (P18; sacrificed on 18th day of gestation), $n = 13$; and (ii) non-pregnant group (NP), $n = 13$. The animals were kept in the same animal facility under standard housing conditions for at least 3 days before imaging.

To harvest the liver, rats were anesthetized with an overdose of isoflurane vapor and then decapitated with a rodent guillotine. A slice of liver (approximately 20 mm in height, 5–8 mm in width) was cut from the left lateral lobe of the fresh liver and transferred directly to the sample tube for MR imaging, while the remaining liver tissue was prepared for histological analysis. The width of the liver slice was trimmed to fit the diameter of the sample tube so that the liver slice can be slid into the tube easily without any compression. In 8 rats of each group, the freshly harvested livers were weighed and the blood collected- approx. 0.8 ml per rat in blood collection tubes containing EDTA and lithium heparin (Sarstedt, Germany)- for laboratory analysis.

Histology and Immunostaining

After harvesting, fresh liver tissue samples (from 8 rats per group) were fixed in 4 % formaldehyde solution (ROTI® Histofix 4 %, Roth, Karlsruhe, Germany) at room temperature for 24 h. After fixation, the samples were dehydrated for 24 h and embedded in paraffin (ROTI® Plast, Roth, Karlsruhe, Germany).

The tissue paraffin blocks were sliced into 2 µm thick sections and finally transferred onto Superfrost/Superfrost Plus slides (R. Langenbrinck GmbH, Emmendingen, Germany). As the mechanical properties quantified by MRE directly associate with microarchitecture of the tissue and the arrangement of the structure elements, especially those in the extra cellular matrix (ECM), we have selected the following staining methods for morphological characterization: hematoxylin and eosin (H&E; Mayer's Hemalum Solution, Merck, Darmstadt, Germany; Eosin Y solution, Sigma-Aldrich, Darmstadt, Germany) and Elastica van Gieson (Merck, Darmstadt, Germany). As hyperproliferation of hepatocytes has been reported in Bustamante et al. (2010), Dai et al. (2011) for pregnant rats, the liver tissue sections were also immunostained for Ki-67 protein. The primary antibody (clone SolA15, eBioscience™ from Thermo Fisher Scientific; Thermo Fisher Scientific Cat# 14-5698-80, RRID:AB_10853185) was pre-incubated with FabuLight secondary antibody (biotinylated goat anti-rat; Jackson ImmunoResearch). Biotin was detected by streptavidin coupled with alkaline phosphatase (ALP) and RED as chromogen [both Dako REAL™ Detection System, ALP/RED, Rabbit/Mouse (Agilent Technologies)], nuclei were counterstained with hematoxylin (Merck Millipore).

Images of stained sections were taken with a BZ-X800 fluorescence microscope (KEYENCE DEUTSCHLAND GmbH, Neu-Isenburg, Germany). Five high-power fields per animal were analyzed. Hepatocytes and Ki67-positive hepatocytes were counted per field of view (FoV) at 40x magnification in H&E-stained and immunostained sections, respectively, using ImageJ software version 1.52v (Schneider et al., 2012). Histological analysis was performed in a blinded manner.

Magnetic Resonance Elastography and Diffusion-Weighted Imaging

All tissue samples for MRI (P18, n = 13; NP, n = 13) were taken from the left lateral lobe of the liver which is the largest lobe, facilitating sample preparation (**Figure 1A**). The MRI measurements started 2 h post-mortem. Liver slices (approximately 20 mm in height, 5–8 mm in width) were cut from the liver. The samples were placed in a glass tube (**Figure 1B**), which was then inserted in a 0.5-T compact MRI device (Pure Devices GmbH, Würzburg, Germany) for both MRE and DWI.

The compact MRE setup (tabletop MRE) was described in detail in previous publications (Braun et al., 2018;

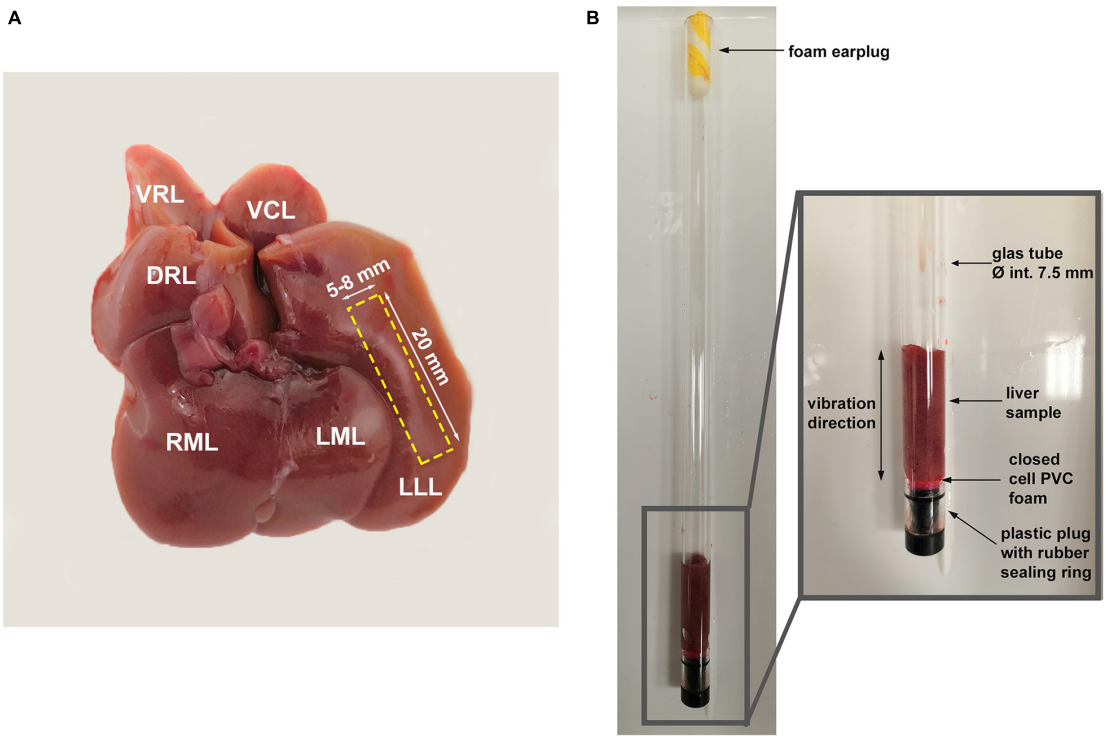

FIGURE 1 | (A) Photo of the fresh liver of a non-pregnant rat; rectangular area marked by dashed yellow line indicates the sample taken for MRI examinations. LLL, left lateral lobe; LML, left middle lobe; RML, right middle lobe; DRL, dorsal right lobe; VRL, ventral right lobe; VCL, ventral caudate lobe; and DCL, dorsal caudate lobe. **(B)** Liver sample in the glass tube used for tabletop MRI.

de Schellenberger et al., 2019; Sauer et al., 2019; Everwien et al., 2020). In short, a gradient amplifier (DC 600, Pure Devices GmbH, Würzburg, Germany) and a piezo-actuator (Piezosystem Jena, Jena, Germany) which was directly coupled to the glass sample tube, were integrated into the tabletop MRI device for generating mechanical vibrations and introducing them into the tissue sample. A spin-echo-based MRE sequence as described in Braun et al. (2018) was used for acquiring wave images.

Imaging parameters for tabletop MRE and DWI were similar to those described in Braun et al. (2018), de Schellenberger et al. (2019), Sauer et al. (2019), Everwien et al. (2020). In brief, mechanical vibrations of 800 Hz were excited for MRE acquisition. Dynamic wave propagation was recorded in eight time steps over a wave cycle in one axial 3-mm thick slice with a field of view of 9.6 × 9.6 mm^2 (64 × 64 matrix size). With a repetition time (TR) of 0.5 s and an echo time (TE) of 20 ms, the total MRE acquisition time was 3 min. DWI was performed with a customized spin-echo sequence (Sauer et al., 2019) using seven *b*-values (50, 175, 300, 425, 550, 675, and 800 s/mm^2). One 3-mm single slice with an in-plane resolution of 600 μm was acquired with a TR of 1 s and TE of 8 ms, and total acquisition time was 5 min. During one imaging session, MRE and DWI were performed in an interleaved manner, and the MRE/DWI block was repeated five times, resulting in a total acquisition time of 40 min. Sample temperature was kept constant at 30°C for all MRI examinations. During the acquisition time, the liver sample which was sealed in the sample tube and kept at a constant temperature was considered well-conditioned.

For MRE data post-processing, shear wave speed (c in m/s) and penetration rate (a in m/s) were derived by taking the analytic solution of the fitting of the single profile of complex-valued wave along the z-direction based on a Bessel function, as described in Braun et al. (2018), de Schellenberger et al. (2019). c represents tissue stiffness while penetration rate a is inversely correlated with tissue viscosity. For comparing to results obtained by ultrasound elastography, c can be converted to Young's modulus (E) with: $E = 3\rho c^2$ where ρ is the density, which we assume to be 1 kg/l for all biological soft tissues. For DWI, maps of apparent diffusion coefficient (ADC), which quantifies water diffusivity, were generated with mono-exponential fitting and linear regression analysis taking images at all seven *b*-values. Images with *b*-value of 50 were also used for fitting considering the absence of perfusion in our *ex vivo* samples. Data were post-processed using algorithms written in MATLAB (R2019b, The Mathwork Inc., Natick, MA, United States).

Statistical Analysis

Mixed analysis of variance (ANOVA) was performed to account for the effects and interactions of two factors present in our data – acquisition time (within-subject factor) and pregnancy (between-subject factor). Normality was tested with both the Shapiro–Wilk test and the Kolmogorov–Smirnov test. Differences between the pregnant and non-pregnant groups were tested using the unpaired *t*-test for normally distributed data and the Mann–Whitney test for datasets that violated the normality assumption. Relationships between data were assessed by Pearson correlation ($n > 10$) and Spearman correlation ($n < 10$). *P*-values below 0.05 were considered statistically significant.

Graphical and statistical analysis was performed with GraphPad Prism (GraphPad Prism 8.01. for Windows, GraphPad Software, San Diego, CA, United States, www.graphpad.com; GraphPad Prism, RRID:SCR_002798) and SPSS 23 (SPSS Inc, Chicago, IL, United States; SPSS, RRID:SCR_002865.

RESULTS

General Characterization of Livers From Pregnant Rats

A representative photo of two rat livers is shown in **Figure 2A**. The liver from a P18 rat was visibly larger compared to that from an NP rat. A significant difference in liver weight was observed between the pregnant and non-pregnant groups (P18: 18.8 ± 1.2 *g vs* NP: 11.2 ± 1.1 *g*, $p < 0.001$, $n = 8$ per group, **Figure 2B**). The livers from P18 rats were on average 40% heavier than those from non-pregnant rats.

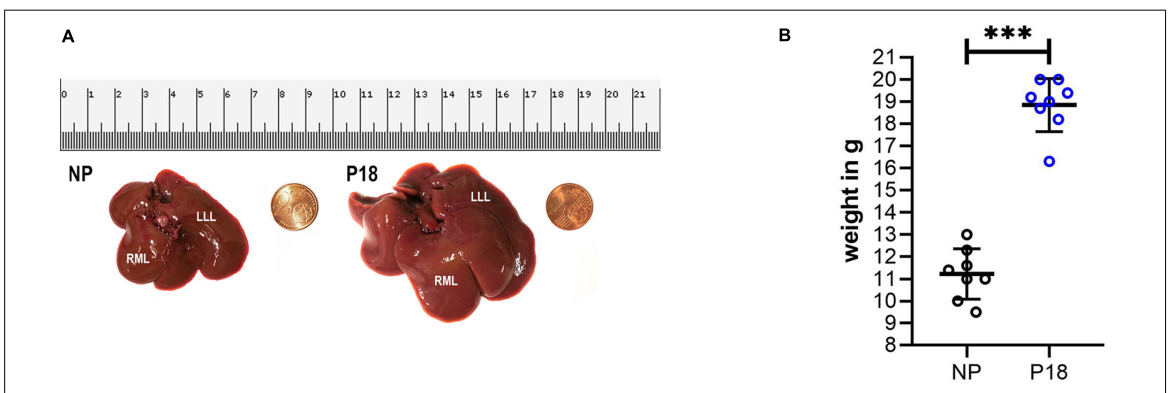

FIGURE 2 | (A) Photos of fresh liver from non-pregnant (NP) and pregnant (P18) rats for visual comparison of liver sizes. **(B)** Scatter plots of liver weight in pregnant (P18) and non-pregnant (NP) groups with mean and standard deviation. ***$p < 0.001$. LLL, left lateral lobe and RML, right middle lobe.

Histological Evaluation

The number of hepatocytes per FoV at 40x magnification was significantly lower in the P18 rats than in the NP rats (P18: 104 *vs* NP: 140, $p < 0.001$, $n = 8$ per group), see **Figure 3**.This 26 % reduction in hepatocyte counts per FoV was characteristic of hepatocyte hypertrophy.

As Ki67 protein is present during all active phases of the cell cycle, it is indicative of cell proliferation. In our samples, we observed a 4-fold increase in Ki67-positive hepatocytes in livers from pregnant rats (P18: 12 *vs* NP: 3, $p < 0.001$, $n = 8$ per group, **Figure 4**).

Livers from P18 rats did not differ from those of NP rats in terms of hepatic collagen or elastin content, as shown in the H&E- (**Figure 3A**) and Elastica van Gieson (EvG)-stained slices (**Figure 5**). Moreover, no visible signs of liver pathologies such as ballooning, steatosis, and inflammation were present in H&E-stained slices in either group.

Additionally, the presence of erythrocytes was visually assessed in both H&E and EvG-stained slices and there was no visible difference between the NP and the P18 groups, as shown in **Supplementary Figure 1**.

Biochemical Analysis

A total of 14 serum markers were analyzed. While 4 markers [alanine transaminase (ALT), total protein, creatinine, red blood cells] showed no significant changes during pregnancy, total bilirubin (P18, 2.6 ± 0.3 μmol/l; NP, 2.1 ± 0.7 μmol/l, and $p = 0.049$) and triglyceride (P18, 3.9 ± 1.4 mmol/l; NP, 1.9 ± 0.6 mmol/l, and $p < 0.001$) were significantly increased while the remaining markers showed a significant reduction during pregnancy. The results of biochemical analysis are compiled in **Table 1**.

Magnetic Resonance Elastography

Based on the mixed ANOVA analysis of MRE parameters acquired at multiple time points of the P18 and NP groups, acquisition time, the within-subject factor, had no significant influence on MRE parameters (c, $p = 0.50$; a, $p = 0.18$) while pregnancy status, the between-subject factor, had a significant effect on both c ($p = 0.01$) and a ($p < 0.001$). Additionally, there were no significant interactions between these two factors for c ($p = 0.98$) or a ($p = 0.44$).

Since acquisition time had no effect on MRE parameters, we averaged both c and a values of five acquisitions over 40 min

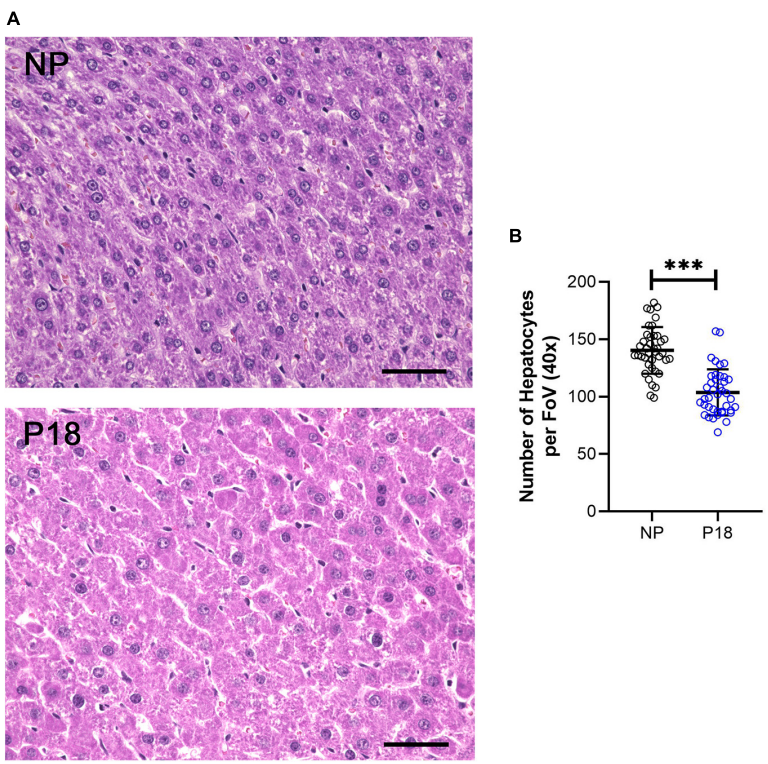

FIGURE 3 | (A) Representative H&E-stained liver sections from non-pregnant (NP) and pregnant (P18) rats. Scale bars correspond to 50 μm. Hepatocytes were counted at 40x optical field, five high-power images per animal were analyzed. **(B)** Scatter plots of numbers of hepatocytes per field of view (FoV) in pregnant (P18) and non-pregnant (NP) groups with mean and standard deviation. ***$p < 0.001$.

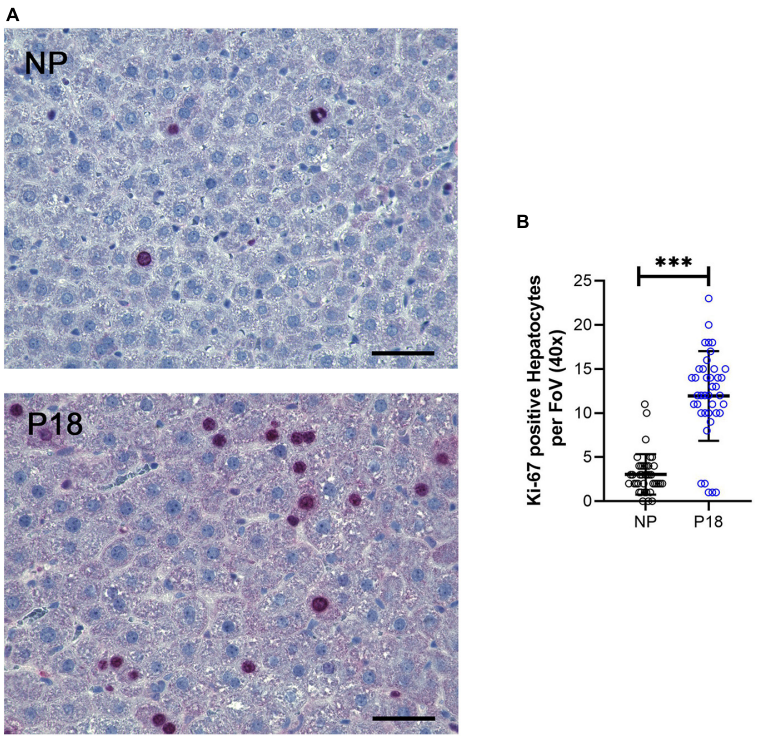

FIGURE 4 | (A) Representative Ki-67-immunostained liver sections from non-pregnant (NP) and pregnant (P18) rats. Scale bars correspond to 50 μm. Ki-67-positive hepatocytes were counted at 40x optical field, five high-power images per animal were analyzed. **(B)** Scatter plots of numbers of Ki-67-positive hepatocytes per field of view (FoV) in pregnant (P18) and non-pregnant (NP) groups with mean and standard deviation. ***$p < 0.001$.

for each animal, and compared the difference between the P18 and NP groups using the *t*-test. As shown in **Figure 6A**, *c* of the P18 group was significantly higher than that of the NP group (P18: 3.8 ± 0.4 m/s *vs* NP: 3.3 ± 0.5 m/s, $p = 0.012$). Similarly, a significant increase in penetration rate *a* was observed in the P18 group compared to the NP group (P18: 2.1 ± 0.3 m/s *vs* NP: 1.6 ± 0.2 m/s, $p < 0.001$, **Figure 6B**).

Correlation analysis was performed by pooling the data from the P18 and NP groups. We observed a positive correlation between *c* and *a* (Pearson's $r = 0.49$; $p = 0.011$) and a negative correlation between *a* and the number of hepatocytes per FoV (Pearson's $r = -0.76$; $p = 0.002$), as shown in **Figures 7A,C**.

We also correlated MRE parameters with biochemical results. There were a total of five significant correlations: between *c* and ALP (Pearson's $r = -0.7$; $p = 0.003$), *a* and ALP (Pearson's $r = -0.65$; $p = 0.006$), *a* and albumin (Pearson's $r = -0.68$; $p = 0.004$), *a* and urea (Pearson's $r = -0.54$; $p = 0.033$), and *a* and glucose (Pearson's $r = -0.76$; $p < 0.001$).

Diffusion-Weighted Imaging

Mixed ANOVA analysis of the DWI data acquired at multiple time points in the P18 and NP groups revealed that the effect of acquisition time (within-subjects factor) was not significant ($p = 0.19$) while the pregnancy status (between-subject factor) significantly influenced the ADC ($p < 0.001$). Also, there was no significant interaction between these two factors ($p = 0.51$). Based on the results of mixed ANOVA analysis, we averaged the ADC values of the five acquisitions over 40 min for each animal and compared the P18 and NP groups with the *t*-test. As shown in **Figure 6C**, ADC values in the P18 group were significantly higher than in the NP group (P18: $0.47e^{-3} \pm 0.03e^{-3}$ mm^2/s; NP: $0.42e^{-3} \pm 0.04e^{-3}$ mm^2/s, $p < 0.001$).

For correlation analysis, ADC values from the P18 and NP group were pooled. We observed a positive correlation between *a* and ADC (Pearson's $r = 0.48$; $p = 0.013$) and a negative correlation between ADC and the number of hepatocytes per FoV (Pearson's $r = -0.67$; $p = 0.009$). Results of correlation analysis are shown in **Figures 7B,D**.

We also tested correlation between ADC values and biochemical parameters. Four biochemical parameters – bile acid (Pearson's $r = -0.66$, $p = 0.005$), triglyceride (Pearson's $r = 0.5$; $p = 0.047$), albumin (Pearson's $r = -0.65$; $p = 0.007$), and glucose (Pearson's $r = -0.65$; $p = 0.006$) – were found to be significantly correlated with ADC values.

Group mean values and standard deviations of the aforementioned imaging parameters are presented in **Table 2**.

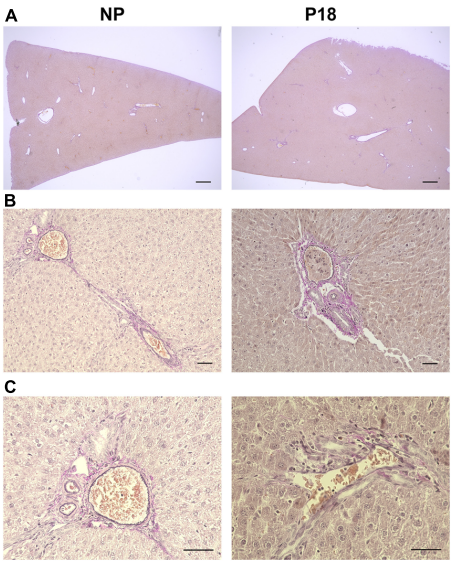

FIGURE 5 | Representative Elastica van Gieson (EvG)-stained liver sections from non-pregnant (NP) and pregnant (P18) rats. **(A)** 2x optical field, scale bars correspond to 500 μm. **(B)** 20x optical field, scale bars correspond to 50 μm. **(C)** 40x optical field, scale bars correspond to 50 μm. Elastic fibers are stained black and collagen red.

TABLE 1 | Mean serum markers with standard deviation of the pregnant and non-pregnant groups.

Parameter	Pregnant (n = 8)	Non-pregnant (n = 8)	p-value
ALP (U/l)	78.0 ± 25.0	116.0 ± 24.2	0.022
AST (U/l)	101.0 ± 14.2	145.6 ± 48.6	0.026
ALT (U/l)	69.9 ± 9.4	79.4 ± 13.6	0.133
GLDH (U/l)	4.7 ± 2.4	9.8 ± 5.5	0.033
Total bilirubin (μmol/l)	2.6 ± 0.3	2.1 ± 0.7	0.049
Bile acids (μmol/l)	14.3 ± 11.8	40.5 ± 28.8	0.026
Triglyceride (mmol/l)	3.9 ± 1.4	1.9 ± 0.6	0.001
Albumin (g/l)	31.0 ± 1.7	34.3 ± 2.0	0.003
Total protein (g/l)	58.8 ± 5.0	61.0 ± 3.6	0.319
Creatinine (μmol/l)	19.4 ± 1.4	21.7 ± 4.1	0.153
Urea (mmol/l)	6.2 ± 0.6	7.4 ± 0.9	0.011
Glucose (mmol/l)	5.1 ± 0.6	7.5 ± 0.9	< 0.001
Hemoglobin (g/l)*	110.0 ± 3.8	142.5 ± 4.4	< 0.001
Red blood cells (T/l)**	6.0 ± 0.2	6.7 ± 2.5	0.106

*ALP, Alkaline phosphatase; AST, Aspartate Transaminase; ALT, Alanine transaminase; and GLDH, Glutamate dehydrogenase.*Pregnant n = 7 and non-pregnant n = 4; **pregnant n = 7 and non-pregnant n = 5- the amount of blood was insufficient to execute the test.*

DISCUSSION

In this study, compact MRE and DWI were used to study biophysical changes occurring in the liver during pregnancy. Our results obtained in rat livers reveal that pregnancy increases stiffness and water diffusivity while reducing viscosity. The biophysical changes identified with these two imaging techniques were correlated with and validated by extensive histological and biochemical analysis.

The most obvious change was a pregnancy-related increase in liver size caused by hepatocyte hypertrophy and hyperproliferation. A pregnancy-related increase in liver weight is well documented for animals (Rosenfeld, 1977; Nuwayhid, 1979; Buelke-Sam et al., 1982; Ahokas et al., 1984). Hollister et al. (1987) were the first to report hepatic growth in pregnancy as a result of hepatocyte hypertrophy. This was later confirmed by other studies (Bustamante et al., 2010; Gielchinsky et al., 2010; Milona et al., 2010; Dai et al., 2011) showing hyperproliferation of hepatocytes (Bustamante et al., 2010; Milona et al., 2010; Dai et al., 2011), increased hepatic DNA content, and an altered hepatic gene expression profile (Bustamante et al., 2010; Dai et al., 2011) during pregnancy. An enhanced liver metabolism during pregnancy could lead to the observed liver growth (Pedrycz et al., 2014). Additionally, elevated estrogen levels in pregnancy (Abbassi-Ghanavati et al., 2009) were reported to induce transient hepatocyte proliferation and liver growth (Fisher et al., 1984; Yager et al., 1994). In the current study, considering the absence of ballooning, steatosis and inflammation based on histopathology, the observed hepatocyte hypertrophy was a result of increased DNA content which was physiological during pregnancy as reported in Bustamante and Dai et al. (Bustamante et al., 2010; Dai et al., 2011). Furthermore, as our histological analysis revealed no evidence of altered structural elements such as collagen and elastic fibers, we conclude that pregnancy-related hypertrophy and hyperproliferation of hepatocytes contributed to the overall increase in liver size and weight in our experiments.

As mentioned in the Introduction, biochemical changes occurring in maternal livers during pregnancy are well studied in humans (Abbassi-Ghanavati et al., 2009; Jamjute et al., 2009; Cunningham, 2010). With the notion that the liver anatomy defers between rats and humans with rats' liver consisting of four main lobes (Kogure et al., 1999), we compared the biochemical changes in rat maternal liver to that of humans. Most of the changes in serum markers we observed in rat livers were in accordance with results obtained in pregnant women (Abbassi-Ghanavati et al., 2009; Jamjute et al., 2009). Similar to humans, pregnant rats showed an increase in hepatic triglycerides with a concomitant reduction in glucose, which is attributable to the high energy demands during pregnancy. Additionally, hemodilution due to a larger volume of circulating plasma leads to lower albumin levels during pregnancy, a phenomenon observed in both rats (De Rijk et al., 2002; Liberati et al., 2004) and humans (Moll, 2001; Carlin and Alfirevic, 2008; Pedrycz et al., 2014). Nevertheless, there were three main differences between our results and findings known from human studies: firstly, the ALP level decreased significantly in pregnant rats, whereas pregnant women may have up to 3 times higher amounts of ALP compared to non-pregnant women. This difference is due to the fact that ALP produced by rat placenta does not enter maternal serum whereas placental ALP in humans contributes to overall maternal ALP (Boles et al.,

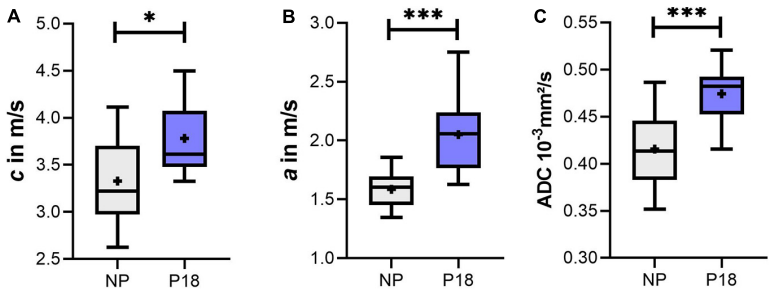

FIGURE 6 | Box plots of **(A)** shear wave speed (*c*), **(B)** penetration rate (*a*), and **(C)** apparent diffusion coefficient (ADC) of the liver in the pregnant (P18) and non-pregnant (NP) rat groups. Data are presented as minimum to maximum with interquartile range and median; + indicates means. $*p \leq 0.05$ and $***p \leq 0.001$.

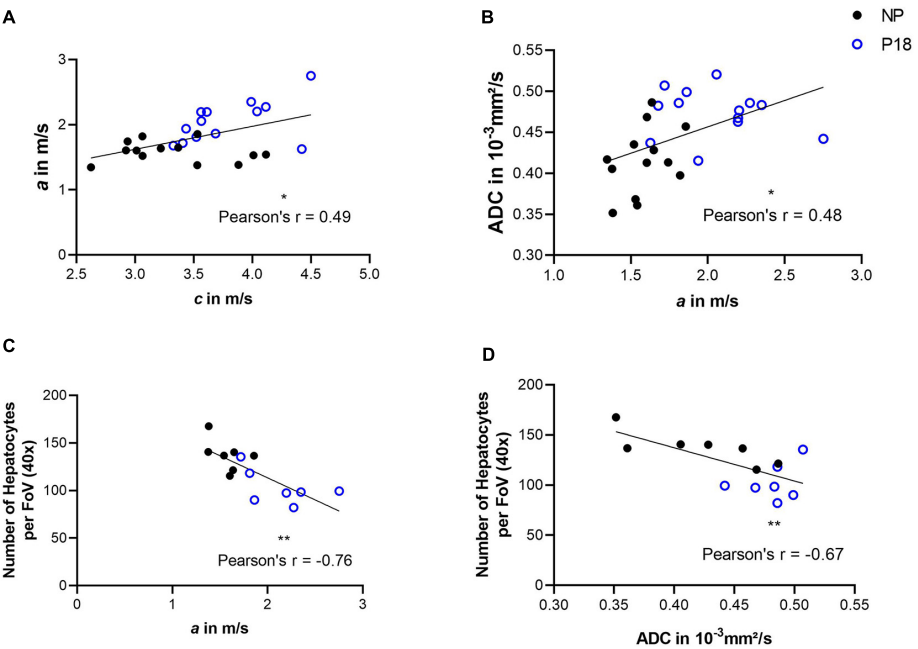

FIGURE 7 | Correlations between: **(A)** shear wave speed (*c*) and penetration rate (*a*); **(B)** *a* and apparent diffusion coefficient (ADC); **(C)** *a* and number of hepatocytes per field of view (FoV); and **(D)** ADC and number of hepatocytes per FoV. Solid black circles represent data from the non-pregnant group (NP) while open blue circles represent data from the pregnant group (P18). $*p \leq 0.05$ and $**p \leq 0.01$.

1972; Pedrycz et al., 2014). Secondly, in contrast to pregnant women, whose bile acid level is normally elevated (Abbassi-Ghanavati et al., 2009; Jamjute et al., 2009; Pedrycz et al., 2014; McIlvride et al., 2017), rats showed reduced bile acids during pregnancy, which was due to hemodilution as reported in Zhu et al. (2013). Thirdly, unlike humans whose bilirubin level is slightly reduced during pregnancy (Abbassi-Ghanavati et al., 2009; Jamjute et al., 2009), we observed an increase in total bilirubin concentration in the pregnant rats which is accordance with previously published data obtained from Wistar rats (Liberati et al., 2004).

Firstly, liver stiffness of rats measured *ex vivo* in our study is higher than that obtained *in vivo*, as reported in Piecha et al. (2016), Elshaarawy et al. (2020). Aside from the difference between *ex vivo* and *in vivo* conditions and the technical dissimilarity between the two imaging modalities, the frequency used in the current study (800 Hz) was higher than that of Fibroscan used in Piecha et al. (2016), Elshaarawy et al. (2020), 573 Hz, leading to the higher stiffness values. Secondly, pregnancy-related increase in liver stiffness was observed *in vivo* by Ammon et al. (2018) and Stenberg Ribeiro et al. (2019). These authors discussed that elevated liver stiffness might be

TABLE 2 | Mean imaging parameters obtained by MRE and DWI and mean liver weight of the pregnant and non-pregnant groups.

Parameter	Pregnant (n = 13)	Non-pregnant (n = 13)	p-value
c in m/s	3.8 ± 0.4	3.3 ± 0.5	0.012
a in m/s	2.1 ± 0.3	1.6 ± 0.2	< 0.001
ADC in mm^2/s	$0.47e^{-3} \pm 0.03e^{-3}$	$0.42e^{-3} \pm 0.04e^{-3}$	< 0.001
Liver weight in g^*	18.9 ± 1.2	11.2 ± 1.1	< 0.001

n = 8 in both groups.

associated with increased blood flow to the liver and elevated portal pressure. In Ammon et al. (Ammon et al., 2018), the author also proposed a possible association between liver congestion and liver stiffness, however, judging by both the macroscopic liver appearance and the microscopic histologic features, we didn't observe signs of liver congestion in our samples. More importantly, as the *in vivo* factors such as blood flow and pressure were not present in our *ex vivo* study, we can exclude blood-flow related influences on our data and attribute the stiffness changes that we observed mainly to structural alterations. The expansion of hepatocytes exert force on the cell membrane which lead to elevated intra-cellular pressure and increased mechanical resistance. The observed increase in stiffness reflects the collective behavior of these enlarged cells and is the macroscopic manifestation of elevated intracellular pressure. The expansion and the proliferation of the hepatocytes in the pregnant liver could also reduce intercellular space which lead to decreased friction as reflected by the wave penetration rate (a). Thus, in our study, the liver of the pregnant rats appeared more solid-like with lower viscosity. Based on our histology results, there were no other pregnancy-related extracellular matrix alterations such as changes in collagen or elastin fiber content which potentially also influence the mechanical properties of the liver (Feng et al., 2016; Hudert et al., 2018; Heucke et al., 2019). In additional to the aforementioned structural elements that contribute to the mechanical properties of the liver, production of macromolecule such as glycogen which was reported to increase especially at the begin of the pregnancy might also influence the observed hepatic viscoelasticity. We suspect that the accumulation of the multibranched polysaccharide with linear chains could alter the microarchitecture of the hepatocytes, thereby changing the macroscopic viscoelasticity of the liver. However, our study couldn't provide further detailed insights regarding macromolecule production. Overall, based on our results, we concluded that hypertrophy and hyperproliferation of hepatocytes are the main contributors to the observed changes in hepatic mechanical properties during pregnancy.

Pregnancy-related changes seen in MRE were accompanied by marked increases in ADC values probably due to hypertrophy of the hepatocytes. As cell density per unit area decreases, there are fewer cell membranes, which act as barriers that restrict water mobility within the hepatocytes, and water diffusion increases. This is consistent with data (Kele and van der Jagt, 2010) showing that reduced cellularity (number of cells per area) due to cell hypertrophy increases water diffusivity. Although the hyperproliferation of hepatocytes potentially reduces water diffusivity (Le Bihan, 2013), we assume that – in light of the considerably expanded liver volumes in our group of pregnant rats, effects of hypertrophy dominated over hyperproliferation in our ADC values.

The inverse correlations between the number of hepatocytes per FoV and imaging parameters a and ADC confirms liver hypertrophy to be the main contributor to both the pregnancy-related reduction of viscosity and increase of water diffusion.

Despite encouraging results, our study has limitations. Firstly, biochemical and histological examinations were performed only in a subgroup of rats. Secondly, we only imaged a small portion of the left lateral hepatic lobe, while clinical *in vivo* MRI normally covers the whole liver. However, as normal pregnancy usually affects the whole maternal liver, we do not expect significant regional difference. Finally, as we investigated only *ex vivo* liver samples, possible confounders for changes of the liver stiffness during pregnancy observed *in vivo* such as intra-abdominal pressure and blood perfusion (Millonig et al., 2010; Mueller, 2016; Piecha et al., 2016; Ammon et al., 2018) were not considered. To assess the influence of these factors, *in vivo* studies using animal models are warranted.

In conclusion, using a compact tabletop MRI scanner, we observed increased stiffness and water diffusion accompanied by decreased viscosity in *ex vivo* rat liver specimens obtained from rats with normal pregnancy. Our results suggest that these changes in biophysical properties were mainly caused by pregnancy-related hypertrophy and hyperproliferation of hepatocytes as supported by biochemical and histological examinations. Finally, the maternal liver during pregnancy mechanically transforms from a soft-viscous to a more solid-rigid state. MRE and DWI have the potential to inform on structural changes of the maternal liver in a clinical context.

DATA AVAILABILITY STATEMENT

The raw data supporting the conclusions of this article will be made available by the authors, without undue reservation.

ETHICS STATEMENT

The animal study was reviewed and approved by Landesamt für Gesundheit und Soziales Berlin.

AUTHOR CONTRIBUTIONS

KG: data acquisition, investigation, formal analysis, data curation, and writing – original draft. HT and LL: software and validation. AK: histological investigation and writing – review and editing. A-SM: investigation and writing – review and editing. AH, ES, NB, and H-GH: writing – review and editing. JB: funding acquisition, resources, methodology, project administration, supervision, and writing – review and editing. IS: conceptualization, funding acquisition, resources, methodology,

project administration, supervision, and critical revision of manuscript. JG: conceptualization, data curation, formal analysis, funding acquisition, investigation, methodology, visualization, supervision, writing – original draft, and critical revision of manuscript. All authors fully qualify for authorship and have approved the final version of the manuscript.

FUNDING

This work was supported by the Deutsche Forschungsgemeinschaft: SFB1340 Matrix in Vision (subprojects: A01, B07, B08, and C03) and BIOQIC. This work was also funded by the German Systems Biology Program "LiSyM", grant no. 31L0057, sponsored by the German Federal Ministry of Education and Research (BMBF).

ACKNOWLEDGMENTS

We thank the research group of Prof. S. Shoichet especially Dr. Stella-Amrei Kunde and Ms. Bettina Bert (Charité – Universitätsmedizin Berlin) for donating the livers used in the P18 group of this study. Thanks to this cooperation, the total number of experimental animals used in Berlin could be reduced (in accordance with the 3R principle). We also acknowledge the valuable support of Simone Spieckermann, who helped with the preparation of the histological samples. We acknowledge support from the German Research Foundation (DFG) and the Open Access Publication Fund of Charité – Universitätsmedizin Berlin.

SUPPLEMENTARY MATERIAL

The Supplementary Material for this article can be found online at: https://www.frontiersin.org/articles/10.3389/fphys.2020.605205/full#supplementary-material

Supplementary Figure 1 | Selected **(A)** H&E-stained and **(B)** EvG-stained liver sections from non-pregnant (NP) and pregnant (P18) rats. Scale bars correspond to 500 μm. Visually, similar amount (both high and low) of erythrocytes were found in NP and P18, indicating that the number of erythrocytes is not uniquely different in the pregnant rats compared with the pregnant ones.

REFERENCES

Abbassi-Ghanavati, M., Greer, L. G., and Cunningham, F. G. (2009). Pregnancy and laboratory studies: a reference table for clinicians. *Obstet Gynecol.* 114, 1326–1331. doi: 10.1097/aog.0b013e3181c2bde8

Ahokas, R. A., Reynolds, S. L., Anderson, G. D., and Lipshitz, J. (1984). Maternal organ distribution of cardiac output in the diet-restricted pregnant rat. *J Nutr.* 114, 2262–2268. doi: 10.1093/jn/114.12.2262

Ammon, F. J., Kohlhaas, A., Elshaarawy, O., Mueller, J., Bruckner, T., Sohn, C., et al. (2018). Liver stiffness reversibly increases during pregnancy and independently predicts preeclampsia. *World J. Gastroenterol.* 24, 4393–4402. doi: 10.3748/wjg.v24.i38.4393

Baeyens, Y. (2000–2013). "The liver in normal pregnancy," in *Madame Curie Bioscience Database [Internet]* (Austin, TX: Landes Bioscience). Available online at: https://www.ncbi.nlm.nih.gov/books/NBK6005/

Baeyens L., Hindi S., Sorenson R. L, German M. S., et al. (2016) β–Cell adaptation in pregnancy *Diab. Obes Metab.* 18,(suupl.1), 63–70. doi: 10.3748/wjg.v24.i38.4393

Boles, J., Leroux, M. L., and Perry, W. F. (1972). Investigation of alkaline phosphatase activity in the serum of pregnant rats. *Biochim. et Biophys. Acta (BBA) - General Sub.* 261, 198–204. doi: 10.1016/0304-4165(72)90331-5

Braun, J., Tzschatzsch, H., Korting, C., Ariza, de Schellenberger, A., Jenderka, M., et al. (2018). A compact 0.5 T MR elastography device and its application for studying viscoelasticity changes in biological tissues during progressive formalin fixation. *Magn. Reson. Med.* 79, 470–478. doi: 10.1002/mrm.26659

Buelke-Sam, J., Nelson, C. J., Byrd, R. A., and Holson, J. F. (1982). Blood flow during pregnancy in the rat: i. Flow patterns to maternal organs. *Teratology* 26, 269–277. doi: 10.1002/tera.1420260309

Bustamante, J. J., Copple, B. L., Soares, M. J., and Dai, G. (2010). Gene profiling of maternal hepatic adaptations to pregnancy. *Liver Int.* 30, 406–415. doi: 10.1111/j.1478-3231.2009.02183.x

Carlin, A., and Alfirevic, Z. (2008). Physiological changes of pregnancy and monitoring. *Best Pract. Res. Clin. Obstet Gynaecol.* 22, 801–823.

Cetin, O., Karaman, E., Arslan, H., Akbudak, I., Yildizhan, R., and Kolusari, A. (2017). Maternal liver elasticity determined by acoustic radiation force impulse elastosonography in intrahepatic cholestasis of pregnancy. *J. Med. Ultrason (2001).* 44, 255–261. doi: 10.1007/s10396-016-0768-z

Cunningham, F. G. (2010). *Laboratory Values in Normal Pregnancy. Protocol for High Risk Pregnancies: An Evidence Based Approach*. Hoboken, NJ: Wiley-Blackwell, 587–595.

Dai, G., Bustamante, J. J., Zou, Y., Myronovych, A., Bao, Q., Kumar, S., et al. (2011). Maternal hepatic growth response to pregnancy in the mouse. *Exp. Biol. Med. (Maywood).* 236, 1322–1332. doi: 10.1258/ebm.2011.011076

De Rijk, E. P. C. T., Van Esch, E., and Flik, G. (2002). Pregnancy dating in the rat: placental morphology and maternal blood parameters. *Toxicol. Pathol.* 30, 271–282. doi: 10.1080/019262302753559614

de Schellenberger, A. A., Tzschatzsch, H., Polchlopek, B., Bertalan, G., Schrank, F., Garczynska, K., et al. (2019). Sensitivity of multifrequency magnetic resonance elastography and diffusion-weighted imaging to cellular and stromal integrity of liver tissue. *J. Biomech.* 88, 201–208. doi: 10.1016/j.jbiomech.2019.03.037

Elshaarawy, O., Alquzi, S., Piecha, F., Sandrin, L., Bastard, C., and Mueller, S. (2020). "Liver stiffness measurements in small animals," in *Liver Elastography: Clinical Use and Interpretation*, ed. S. Mueller (Berlin: Springer International Publishing), 95–102. doi: 10.1007/978-3-030-40542-7_7

Everwien, H., Ariza, de Schellenberger, A., Haep, N., Tzschätzsch, H., Pratschke, J., et al. (2020). Magnetic resonance elastography quantification of the solid-to-fluid transition of liver tissue due to decellularization. *J. Mech. Behav. Biomed. Mater.* 104:103640. doi: 10.1016/j.jmbbm.2020.103640

Feng, Y. H., Hu, X. D., Zhai, L., Liu, J. B., Qiu, L. Y., Zu, Y., et al. (2016). Shear wave elastography results correlate with liver fibrosis histology and liver function reserve. *World J. Gastroenterol.* 22, 4338–4344. doi: 10.3748/wjg.v22.i17.4338

Fisher, B., Gunduz, N., Saffer, E. A., and Zheng, S. (1984). Relation of estrogen and its receptor to rat liver growth and regeneration. *Cancer Res.* 44, 2410–2415.

Frank Wolf, M., Peleg, D., Kariv Silberstein, N., Assy, N., Djibre, A., and Ben-Shachar, I. (2016). Correlation between changes in liver stiffness and preeclampsia as shown by transient elastography. *Hypertens Pregnancy* 35, 536–541. doi: 10.1080/10641955.2016.1197934

Gielchinsky, Y., Laufer, N., Weitman, E., Abramovitch, R., Granot, Z., Bergman, Y., et al. (2010). Pregnancy restores the regenerative capacity of the aged liver via activation of an mTORC1-controlled hyperplasia/hypertrophy switch. *Genes Dev.* 24, 543–548. doi: 10.1101/gad.563110

Heucke, N., Wuensch, T., Mohr, J., Kaffarnik, M., Arsenic, R., Sinn, B., et al. (2019). Non-invasive structure-function assessment of the liver by 2D time-harmonic elastography and the dynamic Liver MAximum capacity (LiMAx) test. *J. Gastroenterol. Hepatol.* 34, 1611–1619. doi: 10.1111/jgh.14629

Hollister, A., Okubara, P., Watson, J. G., and Chaykin, S. (1987). Reproduction in mice: liver enlargement in mice during pregnancy and lactation. *Life Sci.* 40, 11–18. doi: 10.1016/0024-3205(87)90246-3

Hudert, C. A., Tzschatzsch, H., Guo, J., Rudolph, B., Blaker, H., Loddenkemper, C., et al. (2018). US time-harmonic elastography: detection of liver fibrosis in

adolescents with extreme obesity with nonalcoholic fatty liver disease. *Radiology* 288, 99–106. doi: 10.1148/radiol.2018172928

Ipek-Ugay, S., Driessle, T., Ledwig, M., Guo, J., Hirsch, S., Sack, I., et al. (2015). Tabletop magnetic resonance elastography for the measurement of viscoelastic parameters of small tissue samples. *J. Magn. Reson.* 251, 13–18. doi: 10.1016/j.jmr.2014.11.009

Jamjute, P., Ahmad, A., Ghosh, T., and Banfield, P. (2009). Liver function test and pregnancy. *J. Matern Fetal Neonatal, Med.* 22, 274–283.

Kele, P. G., and van der Jagt, E. J. (2010). Diffusion weighted imaging in the liver. *World J. Gastroenterol.* 16, 1567–1576.

Kogure, K., Ishizaki, M., Nemoto, M., Kuwano, H., and Makuuchi, M. (1999). A comparative study of the anatomy of rat and human livers. *J. Hepato-Biliary-Pancreatic Surgery* 6, 171–175. doi: 10.1007/s005340050101

Lain, K. Y., and Catalano, P. M. (2007). Metabolic changes in pregnancy. *Clin. Obstet Gynecol.* 50, 938–948.

Le Bihan, D. (2013). Apparent diffusion coefficient and beyond: what diffusion MR imaging can tell us about tissue structure. *Radiology* 268, 318–322. doi: 10.1148/radiol.13130420

Liberati, T. A., Sansone, S. R., and Feuston, M. H. (2004). Hematology and clinical chemistry values in pregnant Wistar Hannover rats compared with nonmated controls. *Vet. Clin. Pathol.* 33, 68–73. doi: 10.1111/j.1939-165x.2004.tb00352.x

McIlvride, S., Dixon, P. H., and Williamson, C. (2017). Bile acids and gestation. *Mol. Aspects Med.* 56, 90–100. doi: 10.1016/j.mam.2017.05.003

Millonig, G., Friedrich, S., Adolf, S., Fonouni, H., Golriz, M., Mehrabi, A., et al. (2010). Liver stiffness is directly influenced by central venous pressure. *J. Hepatol.* 52, 206–210. doi: 10.1016/j.jhep.2009.11.018

Milona, A., Owen, B. M., van Mil, S., Dormann, D., Mataki, C., Boudjelal, M., et al. (2010). The normal mechanisms of pregnancy-induced liver growth are not maintained in mice lacking the bile acid sensor Fxr. *Am. J. Physiol. Gastrointest Liver Physiol.* 298, G151–G158.

Moll, W. (2001). Die physiologische kreislaufumstellung in der schwangerschaft – Ihre bedeutung für kardiale Erkrankungen. *Zeitschrift für Kardiologie* 90, IV2–IV9.

Mueller, S. (2016). Does pressure cause liver cirrhosis? the sinusoidal pressure hypothesis. *World J. Gastroenterol.* 22, 10482–10501. doi: 10.3748/wjg.v22.i48.10482

Napso, T., Yong, H. E. J., Lopez-Tello, J., and Sferruzzi-Perri, A. N. (2018). The role of placental hormones in mediating maternal adaptations to support pregnancy and lactation. *Front. Physiol.* 9:1091. doi: 10.3389/fphys.2018.01091

Nuwayhid, B. (1979). Hemodynamic changes during pregnancy in the rabbit. *Am. J. Obstet Gynecol.* 135, 590–596. doi: 10.1016/s0002-9378(16)32982-9

Pedrycz, A. Z., Zając, A., Ciechan, A., Lonc, G., Zając, G., Siermontowski, P., et al. (2014). Changes in the liver during pregnancy. *Polish Hyperbaric Res.* 48, 81–92.

Piecha, F., Peccerella, T., Bruckner, T., Seitz, H. K., Rausch, V., and Mueller, S. (2016). Arterial pressure suffices to increase liver stiffness. *Am. J. Physiol. Gastrointest Liver Physiol.* 311, G945–G953.

Rosenfeld, C. R. (1977). Distribution of cardiac output in ovine pregnancy. *Am. J. Physiol.* 232, H231–H235.

Sauer, F., Oswald, L., Ariza, de Schellenberger, A., Tzschatzsch, H., Schrank, F., et al. (2019). Collagen networks determine viscoelastic properties of connective tissues yet do not hinder diffusion of the aqueous solvent. *Soft. Matter.* 15, 3055–3064. doi: 10.1039/c8sm02264j

Schneider, C. A., Rasband, W. S., and Eliceiri, K. W. (2012). NIH Image to ImageJ: 25 years of image analysis. *Nat. Methods.* 9, 671–675. doi: 10.1038/nmeth.2089

Soma-Pillay, P., Nelson-Piercy, C., Tolppanen, H., and Mebazaa, A. (2016). Physiological changes in pregnancy. *Cardiovasc. J. Afr.* 27, 89–94.

Stenberg Ribeiro, M., Hagstrom, H., Stal, P., and Ajne, G. (2019). Transient liver elastography in normal pregnancy - a longitudinal cohort study. *Scand. J. Gastroenterol.* 54, 761–765. doi: 10.1080/00365521.2019.1629007

Yager, J. D., Zurlo, J., Sewall, C. H., Lucier, G. W., and He, H. (1994). Growth stimulation followed by growth inhibition in livers of female rats treated with ethinyl estradiol. *Carcinogenesis* 15, 2117–2123. doi: 10.1093/carcin/15.10.2117

Zhang, Y., Kallenberg, C., Hyatt, H. W., Kavazis, A. N., and Hood, W. R. (2017). Change in the lipid transport capacity of the liver and blood during reproduction in Rats. *Front. Physiol.* 8:517. doi: 10.3389/fphys.2017.00517

Zhu, Q. N., Xie, H. M., Zhang, D., Liu, J., and Lu, Y. F. (2013). Hepatic bile acids and bile acid-related gene expression in pregnant and lactating rats. *PeerJ.* 1:e143. doi: 10.7717/peerj.143

Conflict of Interest: The authors declare that the research was conducted in the absence of any commercial or financial relationships that could be construed as a potential conflict of interest.

4.2.2 Supplementary Material

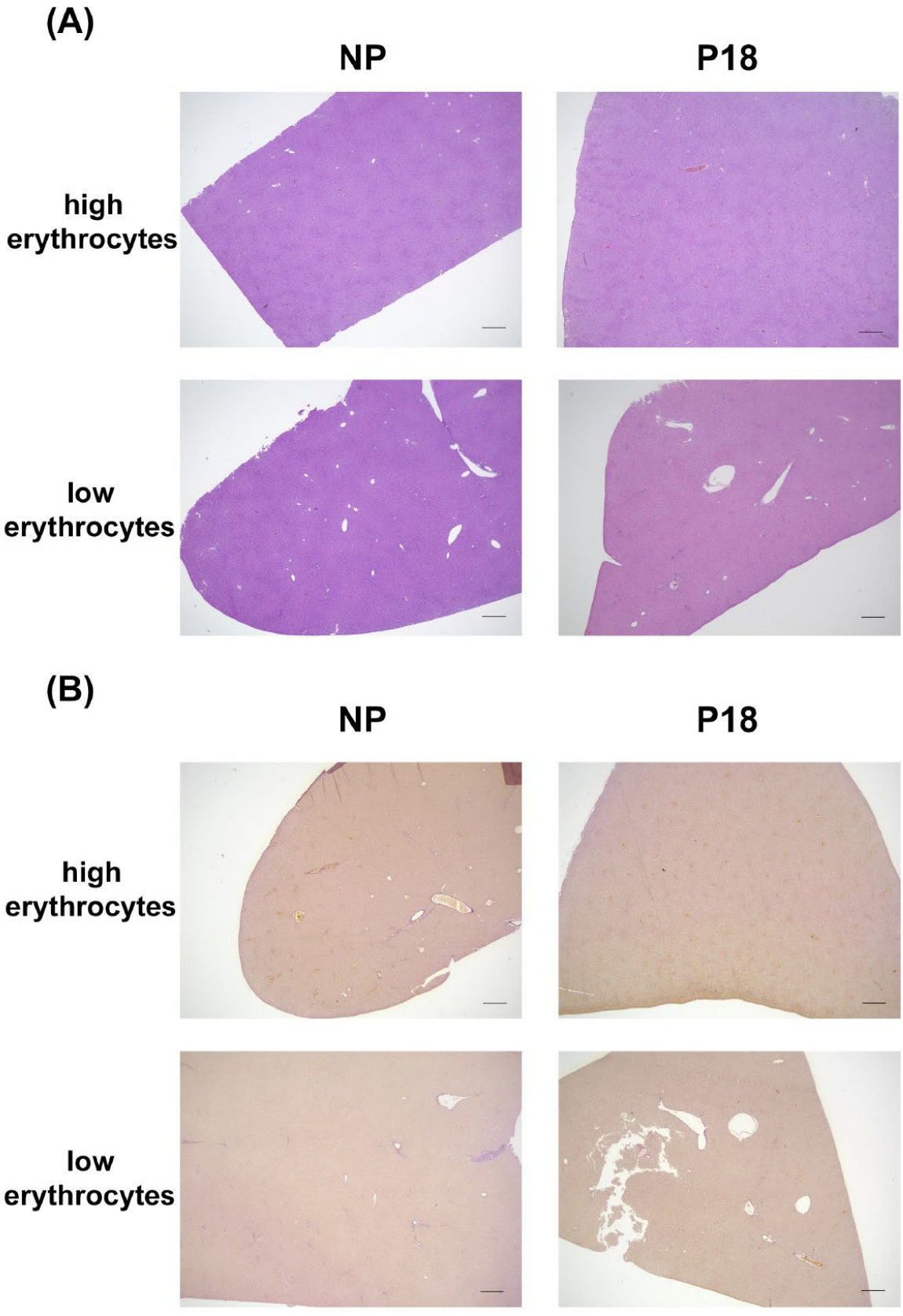

6 Discussion

The microstructure of biological soft tissues is composed of the architectural arrangement of cells, extracellular matrix and vascular structures. The interactions between these compartments determine the tissue's mechanical properties and how mechanical forces are transmitted to the cells. All elements are constantly interacting, and even when considered individually, they are never isolated.

Elastography allows us to investigate which solid component contributes to which mechanical property and to what extent it affects the biomechanical properties we measure. The advent of the compact MRI tabletop scanner with MRE capability has provided new insights into tissue properties [96, 112-114]. Everwien et al. [113] showed decellularized samples to be more viscous and softer than the native liver, suggesting that liver stiffness is mainly determined by hepatocytes. de Schellenberger et al. [114] went one step further and investigated temperature as another factor affecting tissue changes. Stiffness decreased at lower temperatures due to cell membrane degradation and cell detachment. Viscosity, on the other hand, was more sensitive to sinusoidal collagen distortion and sinusoidal dilation, such that samples at -20 °C were less viscous than native tissue and also tissue at -80 °C.

The aim of this work was to further investigate the microstructural changes of liver tissue by magnetic resonance elastography and diffusion-weighted imaging to further elucidate the link between biophysical properties and tissue architecture.

In a first step, we investigated the influence of time since the death on *ex vivo* tissue, assuming that postmortem processes alter the structure of liver tissue and its biophysical properties with the changes being time-dependent and the rate being determined by the tissue's blood content.

We investigated the courses of viscoelasticity over 15 and water diffusion over 20 hours after the death of perfused (low blood content) and nonperfused (high blood content) liver samples. This experiment showed that the nonperfused liver was stiffer and had a higher wave penetration rate and a lower water diffusivity at all time points. We identified three phases for viscoelastic parameters and four phases for water diffusion as a function of postmortem time and related these to changes in tissue microstructure.

Fresh livers were characterized by normally shaped (polygonal) hepatocytes that were nicely packed and well organized. Two hours after death, we observed enlarged hepatocytes that formed a densely packed and compact structure. Due to ischemia, cytotoxic edema [115] occurred, which resulted in higher mechanical resistance and intracellular pressure [116, 117], increased stiffness, and decreased viscosity, while water diffusivity decreased due to the displacement of extracellular water into the intracellular space [118, 119] within the first two hours after death. The changes in viscoelastic parameters were more pronounced in

nonperfused livers due to higher blood content [120-122]. The initial changes were followed by a stable phase lasting up to 10 hours post mortem with minimal changes in SWS, wave penetration rate, and water diffusivity in both groups. Histological examination of the samples 10 hours post mortem showed elongation of hepatocytes with changes in cell packing and rearrangement into a more parallel pattern. These changes caused a reduction in intercellular friction, resulting in easier penetration and propagation of the shear wave through the tissue without losing much energy, and therefore the tissue was less viscous in both groups. The main difference between nonperfused and perfused livers was seen in the behavior of water diffusivity, which increased earlier in nonperfused samples, indicating faster tissue degradation in this group, probably due to the acidic environment resulting from lactate accumulation as a result of postmortem anaerobic glycogenolysis [123-128]. Overall, higher water diffusivity was attributable to increased cell membrane permeability rather than cell collapse and autolysis, which is consistent with the stiffness values not decreasing and also with the visibility of cell membranes in histological specimens.

These results confirm our hypothesis, showing that the cascade of biological events that occur after death lead to structural changes in rat liver, which are reflected in changes in biophysical imaging parameters, and that the extent and speed of these changes depend on the blood content of the tissue.

Decellularization [113], temperature variations [114] and time since death [129] are nonphysiological events. Therefore, we next examined the effects of biophysical changes triggered by a physiological process, such as pregnancy. Ammon et al. [130] and Stenberg et al. [131] showed that the pregnancy-induced adaptation of the maternal body includes biomechanical properties of the liver besides biochemical changes [2, 132-134]. However, they did not investigate the microstructural alterations of the tissue. Accordingly, our second hypothesis was that pregnancy leads to physiological changes in the microstructure of the liver, which affect the biophysical parameters measured by MRE and DWI.

To investigate this hypothesis, we harvested liver samples from pregnant and nonpregnant rats and examined them using the same two imaging techniques and comprehensive histological analysis as in the first study. To avoid effects associated with variations in the time since death, the tissues were examined during the stable phase identified by our initial measurement, which begins two hours post mortem. As expected from numerous reports in the literature, we observed an increase in liver size and weight in pregnant animals [135-138]. Histologically, liver samples from pregnant rats showed hypertrophy and hyperproliferation, again consistent with previous studies [139-143]. Besides the growth and proliferation of hepatocytes, there was no evidence of other changes such as altered structural elements - collagen or elastin. Hypertrophy and hyperproliferation of hepatocytes contribute to an increase in cellularity and tissue compactness, resulting in higher intracellular pressure and a

decrease in intercellular space, which in turn causes an increase in stiffness and a reduction in viscosity. The livers of pregnant rats had solid-like properties with lower viscosity. Due to hypertrophy, cell density per unit area decreased, resulting in a decrease in cell membranes per area and thus a decrease in barriers which limited water mobility. As a result, there was an increase in water diffusivity. Kele and van der Jagt [73] have previously shown that lower cellularity due to cell hypertrophy increases water diffusivity. The increase in total liver volume masks the decrease in water diffusion capacity that may be caused by hyperproliferation [118], so that hepatocyte hypertrophy plays a predominant role and overall water diffusion increases in the pregnant liver. The findings of this study confirm our hypothesis that physiological processes such as pregnancy also lead to structural adaptation of the liver, causing a change in the tissue's viscoelastic properties and water diffusivity and that these changes are detectable by MRE and DWI.

Despite encouraging results, our work has limitations.

Many factors are involved in the postmortem degeneration of biological tissues, including tissue type and its biochemical composition, temperature and humidity of the environment, and cause of death, to mention just a few [144-150]. For this reason, our results only represent changes to be expected under the described circumstances, while their onset after death will vary with the temperature and humidity of the environment. Nevertheless, we think that the cascade of changes will remain more or less similar in other settings. Due to ethical restrictions in our study protocol, we could not use any anticoagulant, so the perfused samples probably contained some residual blood, which could have affected our results.

In our study of pregnancy-related physiological effects, we could not address changes in intra-abdominal pressure and blood perfusion in the *ex vivo* study, according to other studies [130, 151-153] could also influence the observed biophysical changes.

Further studies should be performed on *ex vivo* tissues from different origins under controlled variations of factors such as temperature, cell hydration, and different osmolarities to better understand autolysis and tissue decomposition and their manifestations. In the design phase of *ex vivo* experiments, investigators must consider the postmortem time factor to avoid erroneous results by measuring samples at different time points after death.

Pregnancy-related changes in the liver need to be studied *in vivo* to clarify the influence of other contributors, such as changes in blood flow or increased intra-abdominal pressure due to the growing fetus.

The understanding of tissue characteristics at macro- and microscales, including their changes during proliferation and time-dependent changes in mechanics during tissue maturation, is essential for the future development of new materials which should mimic the features of

biological tissues and may be used in the development of individualized treatments or even as transplants [154].

In conclusion, using a compact tabletop MRI scanner, we demonstrated that MRE and DWI can provide biophysical parameters sensitive to microstructural changes in rat liver tissue. The results of both studies support our hypotheses and improve our understanding of the dependencies between biomechanics and diffusivity of biological materials and the underlying structure. We have elucidated the contributions of cellular components such as cell density, shape and size, packing pattern and organization, and cell membrane integrity to the biophysical properties of liver tissue. In both studies, we also paid attention to the non-cellular components of the tissue, such as the extracellular matrix components, which are known to influence the biophysical parameters of tissues [105, 112, 114, 155]. In our experiments, we found no changes in ECM fibers, such as collagen or elastin, their density, strength or cross-linking. The amount of macromolecules such as glycogen, multibranched polysaccharides or proteoglycans, can also change macroscopic viscoelasticity, due to biochemical processes occurring in the cells, as described in the first study, or due to their ability to bind water, as described by Shahryari et al. [105].

In summary, MRE and DWI have the potential to provide information on structural changes in cellular and noncellular tissue components that, taken together, are reflected in the mechanical behavior and water movement of biological structures. In this dissertation, we have revealed how certain parameters respond to corresponding changes that will help to correctly interpret clinical findings in liver imaging in the future. The results of this work provide the basis for further investigation of pathologies and will contribute to the understanding of underlying processes, allowing faster and more accurate diagnosis.

7 Summary

Studies of microstructural changes of liver tissue by magnetic resonance elastography and diffusion-sensitive magnetic resonance imaging.

The liver is a vital organ that is involved in most processes in the body and rapidly adapts to changes in the organism. Pathological and physiological processes are associated with adaptations of the cellular and noncellular (extracellular matrix) tissue components, which can be visualized by medical imaging such as elastography and diffusion-sensitive magnetic resonance imaging. The relationship between microarchitectural changes and the corresponding biophysical manifestations is not yet clear. Elastography is already a standard clinical procedure in liver diagnosis, which requires a deeper understanding of the influence of structural elements on macroscopic imaging properties.

In order to properly diagnose pathological processes, with special attention to the early detection of chronic liver diseases such as fibrosis or nonalcoholic fatty liver disease, we must first focus on physiological changes to understand the results of modern imaging techniques. In this work, we studied *ex vivo* rat livers to determine how structural changes of the liver depend on postmortem time and blood content on the one hand, and to investigate liver adaptation to physiological gestation on the other.

We identified three phases in the cascade of postmortem biological events that provide a biophysical imaging fingerprint of liver tissue breakdown. Within the first two hours after death, the viscoelastic properties and also the water diffusion capacity of the liver change rapidly due to cytotoxic edema manifested by enlargement of hepatocytes. This is followed by a stable phase up to ten hours post mortem. In the final phase, the degradation phase, there are changes in cell shape, cell packing pattern, and loss of cell membrane integrity, resulting in higher water diffusivity and an increase in the wave penetration rate. In this study, we demonstrated the individual contributions of vascular components and cellular integrity to the changes observed with imaging techniques.

In the second part of this work, we investigated pregnancy-induced changes in microstructure and biophysical properties in the liver. We used the findings from the first study to minimize the effects of additional factors as much as possible. To this end, liver samples were examined under identical conditions during the stable phase - beginning two hours post mortem. Our findings demonstrate that the adaptations of the female organism during pregnancy lead to liver hypertrophy and hyperproliferation of hepatocytes, which cause increased intracellular pressure, increased mechanical resistance, and a decrease in intracellular spaces, resulting in an increase in liver stiffness and wave penetration rate. Due to hypertrophy, cell density per

unit area decreases, and fewer cell membranes (which act as barriers to water movement) are present, resulting in an increase in water diffusivity in the livers of pregnant rats.

Elastography and diffusion-weighted imaging can detect microstructural changes in liver tissue, and the results of this work provide insight into the processes that affect the biomechanical properties and diffusivity of biological tissue and form the basis for further investigation.

8 Zusammenfassung

Untersuchungen der mikrostrukturellen Veränderungen des Lebergewebes mittels Magnetresonanz-Elastographie und diffusionssensitiver Magnetresonanztomographie.

Die Leber als lebenswichtiges Organ ist an den meisten Prozessen im Körper beteiligt und passt sich schnell an Veränderungen im Organismus an. Die pathologischen und physiologischen Prozesse sind mit Anpassungen der zellulären und nichtzellulären (extrazellulären Matrix) Komponenten des Gewebes verbunden, die durch medizinische Bildgebung wie Elastographie und diffusionsempfindliche Magnetresonanztomographie sichtbar gemacht werden können. Der Zusammenhang zwischen mikroarchitektonischen Veränderungen und den entsprechenden biophysikalischen Manifestationen ist noch nicht klar. Die Elastographie ist bereits ein klinisches Standardverfahren in der Leberdiagnostik, das ein tieferes Verständnis des Einflusses von Strukturelementen auf die makroskopischen Bildeigenschaften erfordert.

Um pathologische Prozesse richtig zu diagnostizieren, müssen wir uns zunächst auf physiologische Veränderungen konzentrieren, die Ergebnisse moderner bildgebender Verfahren interpretieren lernen und erst dann in der Lage sein, diese Befunde zur Früherkennung chronischer Lebererkrankungen wie Fibrose oder nichtalkoholischer Fettleber einzusetzen. In dieser Arbeit haben wir *ex vivo* Rattenlebern untersucht, um einerseits die postmortalen Zeit- und Blutgehaltsabhängigkeiten der strukturellen Veränderungen der Leber zu bestimmen und andererseits die Anpassungen der Leber an die physiologische Trächtigkeit zu untersuchen.

Wir identifizierten drei Phasen in der Kaskade postmortaler biologischer Ereignisse, die einen biophysikalischen bildgebenden Fingerabdruck des Lebergewebeabbaus liefern. Innerhalb der ersten zwei Stunden postmortal ändern sich die viskoelastischen Eigenschaften und auch die Wasserdiffusionskapazität der Leber aufgrund eines zytotoxischen Ödems, das sich in einer Vergrößerung der Hepatozyten manifestiert, rasch. Es folgt eine stabile Phase bis zu zehn Stunden post mortem. In der letzten Phase, der Abbauphase, kommt es zu Veränderungen der Zellform, des Zellpackungsmusters und zum Verlust der Integrität der Zellmembran, was zu einer höheren Wasserdiffusionsfähigkeit und einem Anstieg der Wellendurchdringungsrate führt. In dieser Studie haben wir den individuellen Beitrag der vaskulären Komponenten und der zellulären Integrität zu den mit bildgebenden Verfahren beobachteten Veränderungen nachgewiesen.

Im zweiten Teil dieser Arbeit untersuchten wir die schwangerschaftsbedingten Veränderungen der Mikrostruktur und der biophysikalischen Eigenschaften in der Leber. Wir nutzten die Erkenntnisse aus der ersten Studie, um den Einfluss zusätzlicher Faktoren so weit wie möglich

zu minimieren. Zu diesem Zweck wurden die Leberproben unter identischen Bedingungen während der stabilen Phase - beginnend zwei Stunden post mortem - untersucht. Unsere Ergebnisse zeigen, dass die Anpassungen des weiblichen Organismus während der Schwangerschaft zu einer Leberhypertrophie und Hyperproliferation der Hepatozyten führen, die die Ursache für einen erhöhten intrazellulären Druck, einen erhöhten mechanischen Widerstand und eine Verringerung der intrazellulären Räume sind, was zu einer Erhöhung der Lebersteifigkeit und der Wellendurchdringungsrate führt. Aufgrund der Hypertrophie nimmt die Zelldichte pro Flächeneinheit ab, und es sind weniger Zellmembranen (die als Barrieren für die Wasserbewegung fungieren) vorhanden, was zu einem Anstieg der Wasserdiffusionsfähigkeit in den Lebern trächtiger Ratten führt.

Mit Hilfe der Elastographie und der diffusionsgewichteten Bildgebung lassen sich mikrostrukturelle Veränderungen im Lebergewebe nachweisen. Die Ergebnisse dieser Arbeit geben Aufschluss über die Prozesse, die die biomechanischen Eigenschaften und die Diffusionsfähigkeit des Gewebes beeinflussen, und bilden die Grundlage für weitere Untersuchungen.

9 References

1. König, H.E., J. Sautet, and H.-G. Liebich, 7 Verdauungsapparat (Apparatus digestorius), Anhangsdrüsen des Darms, Leber (Hepar), in Anatomie der Haussäugetiere : Lehrbuch und Farbatlas für Studium und Praxis / hrsg. von Horst Erich König ; Hans-Georg Liebich. . 2005, Schattauer: Stuttgart [u.a. p. 355-363.

2. Pedrycz, A.Z., A. Ciechan, A. Lonc, G. Zając, G. Siermontowski, P. Orłowski, M. , Changes in the liver during pregnancy. Polish Hyperbaric Research, 2014. nr 3(48)(PolHypRes 2014 Vol. 48 Issue 3 pp. 81 – 92): p. 81--92.

3. Sourianarayanane, A., Normal Hepatic Function and Physiology, in Hepatic Critical Care, R. Nanchal and R. Subramanian, Editors. 2018, Springer International Publishing: Cham. p. 3-19.

4. Mescher, A.L., Organs Associated with the Digestive Tract, in Junqueira's Basic Histology: Text and Atlas, 15e. 2018, McGraw-Hill Education: New York, NY.

5. Senoo, H., Chapter 18 - Digestion, Metabolism, in The Laboratory Rat, G.J. Krinke, Editor. 2000, Academic Press: London. p. 359-383.

6. Rogers, A.B. and R.Z. Dintzis, 13 - Hepatobiliary System, in Comparative Anatomy and Histology (Second Edition), P.M. Treuting, S.M. Dintzis, and K.S. Montine, Editors. 2018, Academic Press: San Diego. p. 229-239.

7. Suriawinata, A.A. and S.N. Thung, Liver, in Histology for Pathologists. 2012, Lippincott Williams & Wilkins. p. 733-758.

8. Crawford, J.M., P. Bioulac-Sage, and P. Hytiroglou, 1 - Structure, Function, and Responses to Injury, in Macsween's Pathology of the Liver (Seventh Edition), A.D. Burt, L.D. Ferrell, and S.G. Hübscher, Editors. 2018, Elsevier. p. 1-87.

9. Stan, F., Comparative Study of the Liver Anatomy in the Rat, Rabbit, Guinea Pig and Chinchilla. Bulletin of University of Agricultural Sciences and Veterinary Medicine Cluj-Napoca. Veterinary Medicine, 2018. 75: p. 33.

10. Komárek, V., Chapter 13 - Gross Anatomy, in The Laboratory Rat, G.J. Krinke, Editor. 2000, Academic Press: London. p. 253-283.

11. Couinaud, C., [Liver lobes and segments: notes on the anatomical architecture and surgery of the liver]. Presse Med, 1954. 62(33): p. 709-12.

12. Kruepunga, N., et al., Anatomy of rodent and human livers: What are the differences? Biochimica et Biophysica Acta (BBA) - Molecular Basis of Disease, 2019. 1865(5): p. 869-878.

13. Eipel, C., K. Abshagen, and B. Vollmar, Regulation of hepatic blood flow: the hepatic arterial buffer response revisited. World journal of gastroenterology, 2010. 16(48): p. 6046-6057.

14. Colnot, S. and C. Perret, Liver Zonation, in Molecular Pathology of Liver Diseases, S.P.S. Monga, Editor. 2011, Springer US: Boston, MA. p. 7-16.
15. Tsung, A. and D.A. Geller, Gross and Cellular Anatomy of the Liver, in Molecular Pathology of Liver Diseases, S.P.S. Monga, Editor. 2011, Springer US: Boston, MA. p. 3-6.
16. Kiernan, F. and J.H. Green, XXIX. The anatomy and physiology of the liver. Philosophical Transactions of the Royal Society of London, 1833. 123: p. 711-770.
17. Krishna, M., Microscopic anatomy of the liver. Clinical liver disease, 2013. 2(Suppl 1): p. S4-S7.
18. Rappaport, A.M., et al., Subdivision of hexagonal liver lobules into a structural and functional unit. Role in hepatic physiology and pathology. The Anatomical Record, 1954. 119(1): p. 11-33.
19. Kleiner, D.E., The pathology of drug-induced liver injury. Semin Liver Dis, 2009. 29(4): p. 364-72.
20. Saxena, R., N.D. Theise, and J.M. Crawford, Microanatomy of the human liver-exploring the hidden interfaces. Hepatology, 1999. 30(6): p. 1339-46.
21. Takahashi, T., Lobular Structure of the Human Liver from the Viewpoint of Hepatic Vascular Architecture. The Tohoku Journal of Experimental Medicine, 1970. 101(2): p. 119-140.
22. Wagenaar, G.T.M., et al., Distribution and activity of glutamine synthase and carbamoylphosphate synthase upon enlargement of the liver lobule by repeated partial hepatectomies. Journal of Hepatology, 1993. 17(3): p. 397-407.
23. Teutsch, H.F., D. Schuerfeld, and E. Groezinger, Three-dimensional reconstruction of parenchymal units in the liver of the rat. Hepatology, 1999. 29(2): p. 494-505.
24. Wagenaar, G.T.M., et al., Lobular patterns of expression and enzyme activities of glutamine synthase, carbamoylphosphate synthase and glutamate dehydrogenase during postnatal development of the porcine liver. Biochimica et Biophysica Acta (BBA) - General Subjects, 1994. 1200(3): p. 265-270.
25. Gershbein, L.L. and H. Elias, Observations on the anatomy of the rat liver. Anat Rec, 1954. 120(1): p. 85-98.
26. Yarpuzlu, B., et al., Correlation between the mechanical and histological properties of liver tissue. Journal of the Mechanical Behavior of Biomedical Materials, 2014. 29: p. 403-416.
27. Gokgol, C., C. Basdogan, and D. Canadinc, Estimation of fracture toughness of liver tissue: Experiments and validation. Medical Engineering & Physics, 2012. 34(7): p. 882-891.
28. Madhan, K. and S. Raju, Comparative histology of human and cow, goat and sheep liver. Journal of Surgical Academia, 2014. 4(1): p. 10-13.
29. Ekataksin, W., The isolated artery: An intrahepatic arterial pathway that can bypass the lobular parenchyma in mammalian livers. Hepatology, 2000. 31(2): p. 269-279.

30. Kogure, K., et al., A comparative study of the anatomy of rat and human livers. Journal of Hepato-Biliary-Pancreatic Surgery, 1999. 6(2): p. 171-175.
31. Organization, W.H. Global Health Estimates 2020: Disease burden by Cause, Age, Sex, by Country and by Region, 2000-2019. 2020 [cited 2021 14.12.2021 16:36]; Available from: https://www.who.int/data/gho/data/themes/mortality-and-global-health-estimates/global-health-estimates-leading-causes-of-dalys.
32. Schaefer, E.A. and L.S. Friedman, History Taking and Physical Examination for the Patient with Liver Disease, in Schiff's Diseases of the Liver. 2017. p. 1-16.
33. Apte, U., Chapter 1 - Liver Regeneration: An Introduction, in Liver Regeneration, U. Apte, Editor. 2015, Academic Press: Boston. p. 2-11.
34. Nevzorova, Y.A. and C. Trautwein, Chapter 2 - Liver Regeneration, in Zakim and Boyer's Hepatology (Sixth Edition), T.D. Boyer, M.P. Manns, and A.J. Sanyal, Editors. 2012, W.B. Saunders: Saint Louis. p. 20-35.
35. Ryder, S.D., Clinical assessment of liver disease. Medicine, 2011. 39(9): p. 507-510.
36. Vuppalanchi, R. and N. Chalasani, 5 - Laboratory Tests in Liver Disease, in Practical Hepatic Pathology: A Diagnostic Approach, R. Saxena, Editor. 2011, W.B. Saunders: Saint Louis. p. 55-62.
37. Martin, P. and L.S. Friedman, Chapter 1 - Assessment of Liver Function and Diagnostic Studies, in Handbook of Liver Disease (Fourth Edition), L.S. Friedman and P. Martin, Editors. 2018, Elsevier. p. 1-17.
38. Poynard, T. and F. Imbert-Bismut, Chapter 14 - Laboratory Testing for Liver Disease, in Zakim and Boyer's Hepatology (Sixth Edition), T.D. Boyer, M.P. Manns, and A.J. Sanyal, Editors. 2012, W.B. Saunders: Saint Louis. p. 201-215.
39. Curry, M.P. and L.J. Jeffers, Laboratory Tests, Noninvasive Markers of Fibrosis, Liver Biopsy, and Laparoscopy, in Schiff's Diseases of the Liver. 2017. p. 17-37.
40. Badrick, T. and P. Turner, Review and Recommendations for the Component Tests in the Liver Function Test Profile. Indian J Clin Biochem, 2016. 31(1): p. 21-9.
41. Dufour, D.R., et al., Diagnosis and monitoring of hepatic injury. I. Performance characteristics of laboratory tests. Clin Chem, 2000. 46(12): p. 2027-49.
42. Green, R.M. and S. Flamm, AGA technical review on the evaluation of liver chemistry tests. Gastroenterology, 2002. 123(4): p. 1367-84.
43. Abbassi-Ghanavati, M., L.G. Greer, and F.G. Cunningham, Pregnancy and laboratory studies: a reference table for clinicians. Obstet Gynecol, 2009. 114(6): p. 1326-31.
44. Jamjute, P., et al., Liver function test and pregnancy. J Matern Fetal Neonatal Med, 2009. 22(3): p. 274-83.
45. Thapa, B.R. and A. Walia, Liver function tests and their interpretation. The Indian Journal of Pediatrics, 2007. 74(7): p. 663-671.

46. Zoli, M., et al., Physical examination of the liver: is it still worth it? Am J Gastroenterol, 1995. 90(9): p. 1428-32.

47. Patton, H.M., et al., Chapter 15 - Imaging and Noninvasive Diagnosis of Liver Disease: Computerized Tomography, Ultrasound, Magnetic Resonance Imaging, and Emerging Techniques, in Zakim and Boyer's Hepatology (Sixth Edition), T.D. Boyer, M.P. Manns, and A.J. Sanyal, Editors. 2012, W.B. Saunders: Saint Louis. p. 216-254.

48. Sandrasegaran, K. and S. Venkatesh, 7 - Investigative Imaging of the Liver, in Practical Hepatic Pathology: A Diagnostic Approach, R. Saxena, Editor. 2011, W.B. Saunders: Saint Louis. p. 73-84.

49. Das, K.K., M.A. Morgan, and G.G. Ginsberg, Noninvasive and Invasive Imaging of the Liver and Biliary Tract, in Schiff's Diseases of the Liver. 2017. p. 38-69.

50. O'Neill, E.K., J.R. Cogley, and F.H. Miller, The ins and outs of liver imaging. Clin Liver Dis, 2015. 19(1): p. 99-121.

51. Taouli, B., R.L. Ehman, and S.B. Reeder, Advanced MRI methods for assessment of chronic liver disease. AJR. American journal of roentgenology, 2009. 193(1): p. 14-27.

52. Vu, L.N., J.N. Morelli, and J. Szklaruk, Basic MRI for the liver oncologists and surgeons. Journal of hepatocellular carcinoma, 2018. 5: p. 37-50.

53. Strassburg, C.P. and M.P. Manns, Chapter 12 - Liver Biopsy (Quality and Use of Gun), in Zakim and Boyer's Hepatology (Sixth Edition), T.D. Boyer, M.P. Manns, and A.J. Sanyal, Editors. 2012, W.B. Saunders: Saint Louis. p. 173-183.

54. Shiha, G., et al., Asian-Pacific Association for the Study of the Liver (APASL) consensus guidelines on invasive and non-invasive assessment of hepatic fibrosis: a 2016 update. Hepatol Int, 2017. 11(1): p. 1-30.

55. Menghini, G., One-second needle biopsy of the liver. Gastroenterology, 1958. 35(2): p. 190-9.

56. Bedossa, P. and V. Paradis, 2 - Cellular and molecular techniques, in MacSween's Pathology of the Liver (Sixth Edition), A.D. Burt, B.C. Portmann, and L.D. Ferrell, Editors. 2012, Churchill Livingstone: Edinburgh. p. 79-99.

57. Tannapfel, A., H.-P. Dienes, and A.W. Lohse, The Indications for Liver Biopsy. Dtsch Arztebl International, 2012. 109(27-28): p. 477-483.

58. Vernuccio, F., et al., Advances in liver US, CT, and MRI: moving toward the future. European Radiology Experimental, 2021. 5(1): p. 52.

59. Younossi, Z., et al., Global burden of NAFLD and NASH: trends, predictions, risk factors and prevention. Nature Reviews Gastroenterology & Hepatology, 2018. 15(1): p. 11-20.

60. Lombardi, A., M.U. Mondelli, and E.S.G.f.V. Hepatitis, Hepatitis C: Is eradication possible? Liver International, 2019. 39(3): p. 416-426.

61. Masuzaki, R., et al., Noninvasive Assessment of Liver Fibrosis: Current and Future Clinical and Molecular Perspectives. International Journal of Molecular Sciences, 2020. 21(14): p. 4906.
62. Grover, V.P., et al., Magnetic Resonance Imaging: Principles and Techniques: Lessons for Clinicians. J Clin Exp Hepatol, 2015. 5(3): p. 246-55.
63. Kagawa, T., et al., Basic principles of magnetic resonance imaging for beginner oral and maxillofacial radiologists. Oral Radiology, 2017. 33(2): p. 92-100.
64. Ipek-Ugay, S., et al., Tabletop magnetic resonance elastography for the measurement of viscoelastic parameters of small tissue samples. J Magn Reson, 2015. 251: p. 13-8.
65. McGowan, J.C., Basic principles of magnetic resonance imaging. Neuroimaging Clin N Am, 2008. 18(4): p. 623-36, x.
66. van Geuns, R.J., et al., Basic principles of magnetic resonance imaging. Prog Cardiovasc Dis, 1999. 42(2): p. 149-56.
67. Schild, H.H., MRI made easy. 1997: Schering Aktiengesellschaft, Berlin. 105.
68. Stejskal, E.O. and J.E. Tanner, Spin Diffusion Measurements: Spin Echoes in the Presence of a Time-Dependent Field Gradient. The Journal of Chemical Physics, 1965. 42(1): p. 288-292.
69. Le Bihan, D. and E. Breton, Imagerie de diffusion in vivo par résonance magnétique nucléaire. Comptes rendus de l'Académie des sciences. Série 2, Mécanique, Physique, Chimie, Sciences de l'univers, Sciences de la Terre, 1985. 301(15): p. 1109-1112.
70. Le Bihan, D., Diffusion MRI: what water tells us about the brain. EMBO molecular medicine, 2014. 6(5): p. 569-573.
71. Baliyan, V., et al., Diffusion weighted imaging: Technique and applications. World journal of radiology, 2016. 8(9): p. 785-798.
72. Koh, D.M. and D.J. Collins, Diffusion-weighted MRI in the body: applications and challenges in oncology. AJR Am J Roentgenol, 2007. 188(6): p. 1622-35.
73. Kele, P.G. and E.J. van der Jagt, Diffusion weighted imaging in the liver. World journal of gastroenterology, 2010. 16(13): p. 1567-1576.
74. Malayeri, A.A., et al., Principles and Applications of Diffusion-weighted Imaging in Cancer Detection, Staging, and Treatment Follow-up. RadioGraphics, 2011. 31(6): p. 1773-1791.
75. Lewis, S., et al., Diffusion-weighted imaging of the liver: techniques and applications. Magnetic resonance imaging clinics of North America, 2014. 22(3): p. 373-395.
76. Shenoy-Bhangle, A., et al., Diffusion weighted magnetic resonance imaging of liver: Principles, clinical applications and recent updates. World journal of hepatology, 2017. 9(26): p. 1081-1091.

77. Mannelli, L., et al., Diffusion-weighted imaging of the liver: a comprehensive review. Curr Probl Diagn Radiol, 2013. 42(3): p. 77-83.
78. Jiang, H., et al., Liver fibrosis staging with diffusion-weighted imaging: a systematic review and meta-analysis. Abdom Radiol (NY), 2017. 42(2): p. 490-501.
79. Gourtsoyianni, S., et al., Diffusion-weighted imaging and texture analysis: current role for diffuse liver disease. Abdom Radiol (NY), 2020. 45(11): p. 3523-3531.
80. Saito, K., Y. Tajima, and T.L. Harada, Diffusion-weighted imaging of the liver: Current applications. World journal of radiology, 2016. 8(11): p. 857-867.
81. Sack, I., Magnetresonanz-Elastographie. Dtsch Med Wochenschr, 2008. 133(06): p. 247-251.
82. Garra, B.S., Elastography: history, principles, and technique comparison. Abdominal Imaging, 2015. 40(4): p. 680-697.
83. Muthupillai, R. and R.L. Ehman, Magnetic resonance elastography. Nat Med, 1996. 2(5): p. 601-3.
84. Seyedpour, S.M., et al., Application of Magnetic Resonance Imaging in Liver Biomechanics: A Systematic Review. Frontiers in Physiology, 2021. 12(1563).
85. Sarvazyan, A., et al., AN OVERVIEW OF ELASTOGRAPHY - AN EMERGING BRANCH OF MEDICAL IMAGING. Current medical imaging reviews, 2011. 7(4): p. 255-282.
86. Guglielmo, F.F., S.K. Venkatesh, and D.G. Mitchell, Liver MR Elastography Technique and Image Interpretation: Pearls and Pitfalls. RadioGraphics, 2019. 39(7): p. 1983-2002.
87. Tzschätzsch, H., et al., Tomoelastography by multifrequency wave number recovery from time-harmonic propagating shear waves. Medical Image Analysis, 2016. 30: p. 1-10.
88. Tang, A., et al., Ultrasound Elastography and MR Elastography for Assessing Liver Fibrosis: Part 1, Principles and Techniques. AJR Am J Roentgenol, 2015. 205(1): p. 22-32.
89. Mueller, S., Liver Stiffness and Its Measurement, in Liver Elastography: Clinical Use and Interpretation, S. Mueller, Editor. 2020, Springer International Publishing: Cham. p. 13-28.
90. Manduca, A., et al., MR elastography: Principles, guidelines, and terminology. Magnetic Resonance in Medicine, 2021. 85(5): p. 2377-2390.
91. Sack, I., Magnetresonanzelastographie 2.0: Hochaufgelöste Bildgebung zur Bestimmung von Elastizität, Viskosität und Druck weicher Gewebe. Dtsch Med Wochenschr, 2013. 138(47): p. 2426-2430.
92. Venkatesh, S.K. and R.L. Ehman, Magnetic resonance elastography of abdomen. Abdominal Imaging, 2015. 40(4): p. 745-759.
93. Hirsch, S., J. Braun, and I. Sack, Magnetic resonance elastography: physical background and medical applications. 2017: John Wiley & Sons.
94. Morr, A.S., et al., Liquid-Liver Phantom: Mimicking the Viscoelastic Dispersion of Human Liver for Ultrasound- and MRI-Based Elastography. Investigative Radiology, 2022.

95. Li, H., et al., Viscoelasticity Imaging of Biological Tissues and Single Cells Using Shear Wave Propagation. Frontiers in Physics, 2021. 9.
96. Braun, J., et al., A compact 0.5 T MR elastography device and its application for studying viscoelasticity changes in biological tissues during progressive formalin fixation. Magn Reson Med, 2018. 79(1): p. 470-478.
97. Guo, J., I. Sack, and Stephan R. Marticorena Garcia, Liver Magnetic Resonance Elastography: Clinical Use and Interpretation, in Liver Elastography: Clinical Use and Interpretation, S. Mueller, Editor. 2020, Springer International Publishing: Cham. p. 69-93.
98. Reiter, R., et al., Comparison of non-invasive assessment of liver fibrosis in patients with alpha1-antitrypsin deficiency using magnetic resonance elastography (MRE), acoustic radiation force impulse (ARFI) Quantification, and 2D-shear wave elastography (2D-SWE). PLoS One, 2018. 13(4): p. e0196486.
99. Reiter, R., et al., Diagnostic performance of tomoelastography of the liver and spleen for staging hepatic fibrosis. Eur Radiol, 2020. 30(3): p. 1719-1729.
100. Hoodeshenas, S., M. Yin, and S.K. Venkatesh, Magnetic Resonance Elastography of Liver: Current Update. Topics in magnetic resonance imaging : TMRI, 2018. 27(5): p. 319-333.
101. Chen, J., et al., Early detection of nonalcoholic steatohepatitis in patients with nonalcoholic fatty liver disease by using MR elastography. Radiology, 2011. 259(3): p. 749-56.
102. Kim, D., et al., Advanced fibrosis in nonalcoholic fatty liver disease: noninvasive assessment with MR elastography. Radiology, 2013. 268(2): p. 411-9.
103. Hudert, C.A., et al., Tomoelastography for the Evaluation of Pediatric Nonalcoholic Fatty Liver Disease. Investigative Radiology, 2019. 54(4): p. 198-203.
104. Venkatesh, S.K., et al., MR elastography of liver tumors: preliminary results. AJR Am J Roentgenol, 2008. 190(6): p. 1534-40.
105. Shahryari, M., et al., Tomoelastography Distinguishes Noninvasively between Benign and Malignant Liver Lesions. Cancer Res, 2019. 79(22): p. 5704-5710.
106. Singh, S., et al., American Gastroenterological Association Institute Technical Review on the Role of Elastography in Chronic Liver Diseases. Gastroenterology, 2017. 152(6): p. 1544-1577.
107. EASL-ALEH Clinical Practice Guidelines: Non-invasive tests for evaluation of liver disease severity and prognosis. J Hepatol, 2015. 63(1): p. 237-64.
108. Lim, J.K., et al., American Gastroenterological Association Institute Guideline on the Role of Elastography in the Evaluation of Liver Fibrosis. Gastroenterology, 2017. 152(6): p. 1536-1543.
109. Chalasani, N., et al., The diagnosis and management of nonalcoholic fatty liver disease: Practice guidance from the American Association for the Study of Liver Diseases. Hepatology, 2018. 67(1): p. 328-357.

110. Horowitz, J.M., et al., ACR Appropriateness Criteria(®) Chronic Liver Disease. J Am Coll Radiol, 2017. 14(5s): p. S103-s117.
111. Tang, A., et al., Ultrasound Elastography and MR Elastography for Assessing Liver Fibrosis: Part 2, Diagnostic Performance, Confounders, and Future Directions. AJR Am J Roentgenol, 2015. 205(1): p. 33-40.
112. Sauer, F., et al., Collagen networks determine viscoelastic properties of connective tissues yet do not hinder diffusion of the aqueous solvent. Soft Matter, 2019. 15(14): p. 3055-3064.
113. Everwien, H., et al., Magnetic resonance elastography quantification of the solid-to-fluid transition of liver tissue due to decellularization. J Mech Behav Biomed Mater, 2020. 104: p. 103640.
114. de Schellenberger, A.A., et al., Sensitivity of multifrequency magnetic resonance elastography and diffusion-weighted imaging to cellular and stromal integrity of liver tissue. J Biomech, 2019. 88: p. 201-208.
115. Riede, U.N., et al., Einfluß einer einstündigen Autolyse auf die quantitative Zytoarchitektur der Rattenleberzelle (Eine ultrastrukturell-morphometrische Studie). Beiträge zur Pathologie, 1976. 157(4): p. 391-411.
116. Bertalan, G., et al., Biomechanical properties of the hypoxic and dying brain quantified by magnetic resonance elastography. Acta Biomater, 2020. 101: p. 395-402.
117. Arthurs, O.J., et al., Diffusion-weighted perinatal postmortem magnetic resonance imaging as a marker of postmortem interval. European radiology, 2015. 25(5): p. 1399-1406.
118. Le Bihan, D., Apparent diffusion coefficient and beyond: what diffusion MR imaging can tell us about tissue structure. Radiology, 2013. 268(2): p. 318-22.
119. Le Bihan, D. and M. Iima, Diffusion Magnetic Resonance Imaging: What Water Tells Us about Biological Tissues. PLoS Biol, 2015. 13(7): p. e1002203.
120. Berg, S.P., Das postmortale Verhalten des Blutes. Deutsche Zeitschrift für die gesamte gerichtliche Medizin, 1950. 40(1): p. 1-75.
121. Clark MA, W.M., Pless JE, Post mortem changes in soft tissues, in Forensic taphonomy: the postmortem fate of human remains, 1st edn. , S.M. Haglung WD, Editor. 1996, CRC Press, Boca Raton. p. 151-164.
122. García-Manzano, A., et al., Standardization of rat blood clotting tests with reagents used for humans. Proc West Pharmacol Soc, 2001. 44: p. 153-5.
123. Calder, P.C. and R. Geddes, Post mortem glycogenolysis is a combination of phosphorolysis and hydrolysis. Int J Biochem, 1990. 22(8): p. 847-56.
124. SHIMA, S., STUDIES OF AUTOLYSIS. The Journal of Biochemistry, 1922. 2(1): p. 1-26.

125. Popper, H. and O. Wozasek, Zur Kenntnis des Glykogengehaltes der Leichenleber. III. Zeitschrift für die gesamte experimentelle Medizin, 1932. 83(1): p. 682-710.
126. Hertz, W., Der postmortale Glykogenschwund in der Leber von menschlichen Neugeborenen und Feten. Zeitschrift für Kinderheilkunde, 1933. 55(4): p. 410-420.
127. Nunley, W.C., M.W. Dickie, and K.E. Schuit, Delayed, in vivo hepatic postmortem autolysis. Virchows Archiv B, 1973. 14(1): p. 285-291.
128. Donaldson, A.E. and I.L. Lamont, Biochemistry changes that occur after death: potential markers for determining post-mortem interval. PloS one, 2013. 8(11): p. e82011-e82011.
129. Garczyńska, K., et al., Effect of Post-mortem Interval and Perfusion on the Biophysical Properties of ex vivo Liver Tissue Investigated Longitudinally by MRE and DWI. Frontiers in Physiology, 2021. 12(1219).
130. Ammon, F.J., et al., Liver stiffness reversibly increases during pregnancy and independently predicts preeclampsia. World J Gastroenterol, 2018. 24(38): p. 4393-4402.
131. Stenberg Ribeiro, M., et al., Transient liver elastography in normal pregnancy - a longitudinal cohort study. Scand J Gastroenterol, 2019. 54(6): p. 761-765.
132. Moll, W., Die physiologische Kreislaufumstellung in der Schwangerschaft – Ihre Bedeutung für kardiale Erkrankungen. Zeitschrift für Kardiologie, 2001. 90(4): p. IV2-IV9.
133. Bacq, Y. The Liver in Normal Pregnancy. . [cited 2020 09.04.2020]; Available from: https://www.ncbi.nlm.nih.gov/books/NBK6005/.
134. Soma-Pillay, P., et al., Physiological changes in pregnancy. Cardiovascular journal of Africa, 2016. 27(2): p. 89-94.
135. Rosenfeld, C.R., Distribution of cardiac output in ovine pregnancy. Am J Physiol, 1977. 232(3): p. H231-5.
136. Buelke-Sam, J., et al., Blood flow during pregnancy in the rat: I. Flow patterns to maternal organs. Teratology, 1982. 26(3): p. 269-77.
137. Ahokas, R.A., et al., Maternal organ distribution of cardiac output in the diet-restricted pregnant rat. J Nutr, 1984. 114(12): p. 2262-8.
138. Nuwayhid, B., Hemodynamic changes during pregnancy in the rabbit. Am J Obstet Gynecol, 1979. 135(5): p. 590-6.
139. Hollister, A., et al., Reproduction in mice: Liver enlargement in mice during pregnancy and lactation. Life Sciences, 1987. 40(1): p. 11-18.
140. Bustamante, J.J., et al., Gene profiling of maternal hepatic adaptations to pregnancy. Liver Int, 2010. 30(3): p. 406-15.
141. Dai, G., et al., Maternal hepatic growth response to pregnancy in the mouse. Exp Biol Med (Maywood), 2011. 236(11): p. 1322-32.

142. Gielchinsky, Y., et al., Pregnancy restores the regenerative capacity of the aged liver via activation of an mTORC1-controlled hyperplasia/hypertrophy switch. Genes Dev, 2010. 24(6): p. 543-8.
143. Milona, A., et al., The normal mechanisms of pregnancy-induced liver growth are not maintained in mice lacking the bile acid sensor Fxr. Am J Physiol Gastrointest Liver Physiol, 2010. 298(2): p. G151-8.
144. Oka, Zur Frage der postmortalen Autolyse der Zellgranula. Virchows Archiv für pathologische Anatomie und Physiologie und für klinische Medizin, 1920. 228(1): p. 200-215.
145. Otto, G., et al., Elektronenmikroskopische Befunde während hypothermer Lagerungskonservierung der Leber. Langenbecks Archiv für Chirurgie, 1981. 354(2): p. 117-123.
146. Milroy, C.M., Forensic Taphonomy: The Postmortem Fate of Human Remains. BMJ, 1999. 319(7207): p. 458.
147. Tomita, Y., et al., Ultrastructural changes during in situ early postmortem autolysis in kidney, pancreas, liver, heart and skeletal muscle of rats. Legal Medicine, 2004. 6(1): p. 25-31.
148. Takeichi, S., C. Wakasugi, and I. Shikata, Fluidity of cadaveric blood after sudden death: Part I. Postmortem fibrinolysis and plasma catecholamine level. Am J Forensic Med Pathol, 1984. 5(3): p. 223-7.
149. Takeichi, S., C. Wakasugi, and I. Shikata, Fluidity of cadaveric blood after sudden death: Part II. Mechanism of release of plasminogen activator from blood vessels. Am J Forensic Med Pathol, 1985. 6(1): p. 25-9.
150. Takeichi, S., et al., Fluidity of cadaveric blood after sudden death: Part III. Acid-base balance and fibrinolysis. Am J Forensic Med Pathol, 1986. 7(1): p. 35-8.
151. Millonig, G., et al., Liver stiffness is directly influenced by central venous pressure. J Hepatol, 2010. 52(2): p. 206-10.
152. Mueller, S., Does pressure cause liver cirrhosis? The sinusoidal pressure hypothesis. World J Gastroenterol, 2016. 22(48): p. 10482-10501.
153. Piecha, F., et al., Arterial pressure suffices to increase liver stiffness. Am J Physiol Gastrointest Liver Physiol, 2016. 311(5): p. G945-G953.
154. Guimarães, C.F., et al., The stiffness of living tissues and its implications for tissue engineering. Nature Reviews Materials, 2020. 5(5): p. 351-370.
155. Hudert, C.A., et al., How histopathologic changes in pediatric nonalcoholic fatty liver disease influence in vivo liver stiffness. Acta biomaterialia, 2021. 123: p. 178-186.

10 Publications

10.1 First autorship

1. **Garczyńska, K.,** H. Tzschätzsch, A. A. Kühl, A. S. Morr, L. Lilaj, A. Häckel, E. Schellenberger, N. Berndt, H.-G. Holzhütter, J. Braun, I. Sack and J. Guo (2020). "Changes in Liver Mechanical Properties and Water Diffusivity During Normal Pregnancy Are Driven by Cellular Hypertrophy." Frontiers in Physiology 11(1518).
2. **Garczyńska, K.,** H. Tzschätzsch, S. Assili, A. A. Kühl, A. Häckel, E. Schellenberger, N. Berndt, H.-G. Holzhütter, J. Braun, I. Sack and J. Guo (2021). "Effect of Post-mortem Interval and Perfusion on the Biophysical Properties of ex vivo Liver Tissue Investigated Longitudinally by MRE and DWI." Frontiers in Physiology 12(1219).

Under review, pre-printed:

3. **Garczyńska, Karolina** and Hahndorf, Julia and Stolzenburg, Nicola and Taupitz, Matthias and Braun, Jürgen and Sack, Ingolf and Schnorr, Jörg and Guo, Jing, Monitoring Renal Fibrosis in Rats with Chronic Kidney Disease by In Vivo Tomoelastography. Available at SSRN: https://ssrn.com/abstract=3996171 or http://dx.doi.org/10.2139/ssrn.3996171

10.2 Co-autorship

4. de Schellenberger, A. A., H. Tzschatzsch, B. Polchlopek, G. Bertalan, F. Schrank, **K. Garczynska**, P. A. Janmey, J. Braun and I. Sack (2019). "Sensitivity of multifrequency magnetic resonance elastography and diffusion-weighted imaging to cellular and stromal integrity of liver tissue." J Biomech 88: 201-208.
5. Haeckel, A., L. Ascher, N. Beindorff, S. Prasad, **K. Garczyńska**, J. Guo and E. Schellenberger (2021): Long-circulating XTEN864-annexin A5 fusion protein for phosphatidylserine-related therapeutic applications. Apoptosis. DOI: 10.1007/s10495-021-01686-w.

10.3 Oral presentations

1. “Changes in Liver Mechanical Properties and Water Diffusivity During Normal Pregnancy Are Driven by Cellular Hypertrophy”
   K. Garczyńska, H. Tzschätzsch, A. A. Kühl, A. S. Morr, L. Lilaj, A. Häckel, E. Schellenberger, N. Berndt, H.-G. Holzhütter, J. Braun, I. Sack and J. Guo
   14th Colloquium of the CRC 1340 „Matrix in Vision“, Berlin, Germany, digital colloquium (16.02.2021)

2. “Renal fibrosis investigated by *in vivo* multifrequency MR elastography in a rat model of chronic kidney disease.”
   Karolina Garczyńska, Julia Hahndorf, Nicola Stolzenburg, Matthias Taupitz, Jürgen Braun, Ingolf Sack, Jörg Schnorr, and Jing Guo
   Joint Annual Meeting ISMRM-ESMRMB 2022 and the ISMRT 31st Annual Meeting on 07 May 2022 - 12 May 2022 in London, United Kingdom. (09.05.2022, presentation, Preclinical Brain & Body Session)
3. “*In vivo* longitudinal characterization of hepatocellular carcinoma based on viscoelasticity and water diffusivity in an orthotopic mouse model”
   Karolina Garczyńska, Akvile Häckel, Eyk Schellenberger, Anja A. Kühl, Jürgen Braun, Lynn Jeanette Savic, Ingolf Sack, and Jing Guo
   Joint Annual Meeting ISMRM-ESMRMB 2022 and the ISMRT 31st Annual Meeting on 07 May 2022 - 12 May 2022 in London, United Kingdom. (12.05.2022, digital poster, Pre-Clinical Cancer: Session 1)

11 Acknowledgements- Danksagung

Ich möchte mich an dieser Stelle bei Allen bedanken, die mich während der letzten Jahre begleitet und unterstützt haben.

Besonderer Dank gilt Frau Dr. Jing Guo und Herrn Prof. Dr. Ingolf Sack für die Überlassung des Promotionsthemas, deren Vertrauen, die persönliche Betreuung und deren stets tatkräftige und geduldige Unterstützung über die Jahre.

Herrn Univ.-Prof. Dr. Robert Klopfleisch danke ich, für die freundliche Unterstützung, große Hilfsbereitschaft und organisatorische Hilfestellung bei dieser Doktorarbeit.

Ein ganz besonderes Dankeschön geht an meine lieben Kollegen an der Charité Universitätsmedizin Berlin, insbesondere meine Kollegen der AG Sack für die gegenseitige Motivation, stets gute Atmosphäre im Büro und fachlichen Austausch.

Zusätzlich möchte ich mich bei den Mitgliedern vom Sonderforschungsbereich 1340 "Matrix in Vision" und Graduiertenkolleg „Bioqic“ für die hervorragende Kooperation und der Deutschen Forschungsgemeinschaft für die finanzielle Unterstützung bedanken.

Meinem Mann und besten Freund danke ich für seine Geduld und großes Verständnis, für seine stets positive Sichtweise, und dass er immer an mich glaubt und mich dadurch zu Größerem befähigt hat, als ich es mir selbst zugetraut habe.

Zum Schluss möchte ich mich ganz besonders bei meinen Eltern bedanken, dafür, dass sie in allen Lebenslagen für mich da waren und für ihre uneingeschränkte Unterstützung auf meinem bisherigen Lebensweg.
Na koniec chciałbym szczególnie podziękować moim rodzicom za to, że byli przy mnie w każdej sytuacji i za ich niezachwiane wsparcie przez całe moje dotychczasowe życie.

12 Funding Sources- Finanzierungsquellen

This work was funded by the Deutsche Forschungsgemeinschaft (DFG, German Research Foundation): Project number: SFB1340 Matrix in Vision (subproject: B08) and BIOQIC graduate school.

13 Conflicts of interest

The author has no conflicts of interest to declare.

14 Selbstständigkeitserklärung

Hiermit bestätige ich, dass ich die vorliegende Arbeit selbstständig angefertigt habe. Ich versichere, dass ich ausschließlich die angegebenen Quellen und Hilfen in Anspruch genommen habe.

Hereby, I declare that I have composed the presented dissertation independently on my own and without any other resources than the ones indicated.

Berlin, den 01.12.2022 Karolina Maria Krehl